# Synthesis, Properties, and Applications of Single-Domain Magnetic Nanoparticles

Guest Editors: Subhankar Bedanta, Anjan Barman, Wolfgang Kleemann, Oleg Petracic, and Takeshi Seki

# Synthesis, Properties, and Applications of Single-Domain Magnetic Nanoparticles

# Synthesis, Properties, and Applications of Single-Domain Magnetic Nanoparticles

Guest Editors: Subhankar Bedanta, Anjan Barman, Wolfgang Kleemann, Oleg Petracic, and Takeshi Seki

# Editorial Board

# Contents

## Editorial

# Synthesis, Properties, and Applications of Single-Domain Magnetic Nanoparticles

**Subhankar Bedanta,[1] Anjan Barman,[2] Wolfgang Kleemann,[3] Oleg Petracic,[4] and Takeshi Seki[5]**

[1] *School of Physical Sciences, National Institute of Science Education and Research (NISER), IOP Campus, Bhubaneswar 751005, India*

[2] *Department of Condensed Matter Physics and Material Sciences, S. N. Bose National Centre for Basic Sciences, Block JD, Sector III, Salt Lake City, Kolkata 700098, India*

[3] *Department of Physics, University Duisburg-Essen, 47057 Duisburg, Germany*

[4] *Juelich Centre for Neutron Science JCNS and Peter Gruenberg Institute (PGI), JARA-FIT, Forschungszentrum Juelich GmbH, 52425 Juelich, Germany*

[5] *Institute for Materials Research, Tohoku University, 2-1-1 Katahira, Aoba-ku, Sendai 980-8577, Japan*

Correspondence should be addressed to S. Bedanta; sbedanta@niser.ac.in

Since the pioneering work of Stoner and Wohlfarth over six decades ago, the behavior of magnetic single (or *mono*) domain particles has held enormous fascination. Magnetization reversal in such single domain particles occurs often via coherent rotation of spins. As a consequence of this rotation mechanism, magnetic nanoparticles show high coercivities, which lie between those of soft and hard permanent magnetic materials. The ability to control the magnetism in these types of particles makes them very attractive for applications, for example, in information storage. Moreover, the research on magnetic nanoparticles has raised hopes for applications in the fields of biology and medicine, for example, drug-targeting, cancer therapy, lymph node imaging, hyperthermia, and so forth.

Detailed information on the properties of single domain nanoparticles is needed before making use of these nanoparticles for any applications. Also the synthesis of such particles by reproducible means is of great importance. The *superspins* of single-domain particles fluctuate on the timescale modelled within the Néel-Brown theory. The superspins undergo so-called blocking in an ensemble of magnetic nanoparticles with dilute concentration, namely, where inter-particle interactions are negligible. However, in dense ensembles, interaction effects lead to collective states such as *superspin glass* and *superferromagnetism*. Several reports on these subjects as well as on *superparamagnetism* in the very dilute limit have been made in the last decade. This special issue focuses on the preparation, characterization, structural and magnetic properties, and various possible applications of magnetic nanoparticles. It was our hope that it will become an important international platform for researchers to summarize the most recent progress and to exchange ideas in the field of magnetic nanoparticles.

This special issue comprises three review articles. The article by H. Mamiya gives a comprehensive review on progress in understanding the heat dissipation mechanisms of magnetic nanoparticles under large magnetic fields. It also discusses the potential of magnetic nanoparticles in targeted hyperthermia treatment. The review article by S. Mørup et al. outlines realistic models and also experimental studies on spin canting in magnetic nanoparticles. The third review paper written by the editors of this special issue gives a detailed review of various important aspects related to research on magnetic nanoparticles.

The remaining articles in this special issue are research articles, which present selected aspects in reference to synthesis, characterization and also applications of magnetic nanoparticles. The article by Uhm and Rhee explains the synthesis and magnetic properties of Ni and carbon coated Ni by a levitational gas condensation method. The article

by Singh et al. shows the study of the magnetic properties of indirect exchange spring-type FePt/M(Cu,C)/Fe trilayered thin films. Křišťan et al. have studied the preparation of bentonite/iron oxide composites and characterized them by nuclear magnetic resonance (NMR) and Mössbauer spectroscopy. The article by Quy et al. shows the results on the synthesis of silica-coated $Fe_3O_4$ nanoparticles and their application in the detection of pathogenic viruses. Prodan et al. have studied biological properties of iron oxide nanoparticles, which are obtained in an aqueous suspension. The article by Sato et al. reports on atomic structure imaging of epitaxial $L1_0$-type CoPt nanoparticles using chemically sensitive high-angle annular dark-field scanning transmission electron microscopy. $Fe_3O_4$ nanoparticles and nanowires and their magnetorheological (MR) properties are studied in an article by Rwei et al. The same authors present another study devoted to MR properties of polydimethylsiloxane containing powders of $Fe_3O_4$ and $CoFe_2O_4$ nanoparticles with various shapes and at different compositions and concentrations.

## Acknowledgments

*Subhankar Bedanta*
*Anjan Barman*
*Wolfgang Kleemann*
*Oleg Petracic*
*Takeshi Seki*

*Research Article*

# Development for High-Accuracy *In Vitro* Assay of Vascular Endothelial Growth Factor Using Nanomagnetically Labeled Immunoassay

**C. C. Yang,[1] K. W. Huang,[2,3] S. Y. Yang,[1,4] H. H. Chen,[4] T. C. Chen,[1] C. S. Ho,[1] S. F. Chang,[1] J. J. Chieh,[4] H. E. Horng,[4] C. Y. Hong,[5] and H. C. Yang[6]**

[1] *MagQu Co., Ltd., Xindian District, New Taipei City 231, Taiwan*

[2] *Department of Surgery & Hepatitis Research Center, National Taiwan University Hospital, Taipei 100, Taiwan*

[3] *Graduate Institute of Clinical Medicine, College of Medicine, National Taiwan University, Taipei 100, Taiwan*

[4] *Institute of Electro-Optical Science and Technology, National Taiwan Normal University, Taipei 116, Taiwan*

[5] *Graduate Institute of Biomedical Engineering, National Chung Hsing University, Taichung 402, Taiwan*

[6] *Department of Electro-Optical Engineering, Kun Shan University, Yongkang District, Tainan City 710, Taiwan*

Correspondence should be addressed to S. Y. Yang; syyang@magqu.com and H. E. Horng; phyfv001@ntnu.edu.tw

Nanomagnetically labeled immunoassays have been demonstrated to be promisingly applied in clinical diagnosis. In this work, by using antibody-functionalized magnetic nanoparticles and a high-temperature superconducting quantum interference device ac magnetosusceptometer, the assay properties for vascular endothelial growth factor (VEGF) in serum are investigated. By utilizing the assay method so-called immunomagnetic reduction, the properties of assaying VEGF are explored. In addition, the VEGF concentrations in serum samples of normal people and patients with either colorectal or hepatocellular cancer are detected. The experimental results show that the low-detection limit for assaying VEGF is 10 pg/mL, which is much lower than the clinical cut-off VEGF concentration of 50 pg/mL for diagnosing malignancy. Besides, there are no significant interference effects on assaying VEGF from hemoglobin, conjugated bilirubin, and triglyceride. The VEGF concentrations in serum samples donated by normal people and patients with hepatocellular carcinoma or colorectal cancer are detected. A clear difference in VEGF concentrations between these two groups is found. These results reveal the feasibility of applying nanomagnetically labeled immunoassay to clinics.

## 1. Introduction

Early-stage diagnosis is the trend for *in vitro* diagnosis. For immunoassay, the important requirements with early-stage diagnosis are the abilities to assay the ultra-low-concentration biomarkers. One of the categories in the early-stage immunoassay is the screening of malignancy. The biomarker for malignancy is vascular endothelial growth factor (VEGF) [1–4]. In clinics, the cut-off concentration for VEGF is 50 pg/mL. This means the VEGF concentration in the noncancer population is lower than 50 pg/mL [5, 6]. Thus, the low-detection limit of assay kits for VEGF would be better to be lower than 5 pg/mL, or even down to sub-pg/mL.

One popular method to assay VEGF is the so-called enzyme-linked immunosorbent assay (ELISA) [7–9]. However, it is difficult to detect VEGF at low concentrations, such as tens of pg/mL, using ELISA. Further, it requires much time and skill. The results from ELISA tend to be confounded by hemolysis or jaundice, and these phenomena are very common in the blood of cancer patients [10]. Hence, ELISA is usually used to diagnose mild to serve malignancy, not for early-stage diagnosis.

Some of the coauthors developed assay technologies for quantitatively detecting ultra-low-concentration biomolecules [11, 12]. This technology is referred to as SQUID-based immunomagnetic reduction (IMR), where SQUID is

the abbreviation for superconducting quantum interference device. It was demonstrated that the low-detection limit of SQUID-based IMR to assay $\beta$-amyloids is around pg/mL [13, 14]. Thus, it can hopefully be applied to SQUID-based IMR for the quantitative detection of ultra-low-concentration VEGF. This motivates us to characterize the assay of VEGF using SQUID-based IMR.

The detailed physical mechanism of IMR is reported in [15]. Instead of tedious theoretical discussion, phenomenological explanations for IMR are given here. IMR is such a method as assaying target molecules via measuring the reduction in the mixed-frequency magnetic susceptibility of the magnetic reagent owing to the association between magnetic nanoparticles and target molecules, as illustrated in Figures 1(a) and 1(b). Under external multiple ac magnetic fields, magnetic nanoparticles oscillate with the multiple ac magnetic fields via magnetic interaction. Thus, the reagent under external multiple ac magnetic fields shows a magnetic property, called mixed-frequency ac magnetic susceptibility $\chi_{ac}$, as illustrated in Figure 1(a). Via the antibodies on the outmost shell, magnetic nanoparticles associate with and magnetically label biotargets. With the association, magnetic nanoparticles become larger or clustered, as schematically shown in Figure 1(b). The response of these larger magnetic nanoparticles to external multiple ac magnetic fields becomes much less than that of originally individual magnetic nanoparticles. Thus, the $\chi_{ac}$ of the magnetic reagent is reduced due to the association between magnetic nanoparticles and biotargets. In principle, as the amounts of biotargets are reduced, fewer magnetic nanoparticles become larger or clustered. The reduction in $\chi_{ac}$ of the reagent is depressed. Once the reduction in $\chi_{ac}$ is depressed to be lower than the noises of $\chi_{ac}$ of the reagent, the assay result becomes negative. To achieve highly sensitive detections, it is preferred to utilize a detection module with low noise and high sensitivity to $\chi_{ac}$ signals. This is why SQUID is used for IMR because it is a more sensitive sensor of magnetic signals.

In this work, SQUID-based IMR is applied to explore the low-detection limit for assaying VEGF. In addition, the interferences by several materials such as hemoglobin, bilirubin, and triglyceride to the assays of VEGF are investigated for SQUID-based IMR. These results are compared with those done via ELISA. Finally, the VEGF concentrations in human serum from patients with hepatocellular carcinoma or colorectal cancer, as well as normal people, are detected using SQUID-based IMR.

## 2. Materials and Methods

The magnetic reagent used here is magnetic nanoparticles, which are biofunctionalized with antibodies against VEGF (anti-VEGF), and dispersed in pH 7.4 phosphate buffered saline solution (MF-VEG-0060, MagQu). The magnetic core of the particles is $Fe_3O_4$. The $Fe_3O_4$ cores are individually enveloped with dextran. The size distribution of dextran-coated $Fe_3O_4$ particles was detected by dynamic laser scattering (Nanotrac-150, Microtrac). The results are shown in Figure 2(a). The mean diameter was found to be 49.7 nm.

Through chemical reactions, anti-VEGF is covalently bound with dextran [16, 17]. By using dynamic laser scattering (Nanotrac-150, Microtrac), the diameter distribution of the biofunctional magnetic nanoparticles was measured, as shown in Figure 2(b). The mean diameter of the biofunctionalized $Fe_3O_4$ nanoparticles is 57.2 nm. The stability of magnetic reagent stored at 2–8°C is examined by analyzing the time-evolution mean value of the hydrodynamic diameter of particles. The results are shown in Figure 3 and reveal that the hydrodynamic diameter of particles remains unchanged for 36 weeks. This implies that there is no agglomeration of particles in the reagent stored at 2–8°C for 36 weeks. The magnetic hysteresis curve of the magnetic reagent was measured with a vibrating sample magnetometer (HyterMag, MagQu), as shown in Figure 4. The saturated magnetization of the magnetic reagent is 0.3 emu/g, corresponding to the particle concentration of $10^{12}$ particles/mL. Besides, the magnetic reagent shows superparamagnetism.

60 $\mu$L magnetic reagent was thoroughly mixed with the 60 $\mu$L sample solution in a glass tube. The $\chi_{ac}$ signal, $\chi_{ac,o}$, of the mixture before the formation of immunocomplex of VEGF-magnetic-nanoparticles was recorded using a magnetic immunoassay analyzer (XacPro-S, MagQu). Then, the mixture was kept at room temperature for the formation of VEGF-magnetic-nanoparticles, followed by recording the $\chi_{ac}$ signal, $\chi_{ac,\phi}$, of the mixture. It usually takes 3 hours for finishing the formation of VEGF-magnetic-nanoparticles. With the measured $\chi_{ac,o}$ and $\chi_{ac,\phi}$, the IMR signal can be obtained via

$$\text{IMR}(\%) = \frac{\left(\chi_{ac,o} - \chi_{ac,\phi}\right)}{\chi_{ac,o}} \times 100\%. \tag{1}$$

For a given sample solution, the sample was divided into three parts for the triple tests of IMR signals. With the three individual IMR signals, the mean value and the standard deviation of the IMR signals were calculated. To build the characteristic curve, that is, the relationship between the IMR signal and VEGF concentration, various amounts of VEGF (PEP400-31-10, PeproTech) were added to the PBS solution, followed by measuring the IMR signals for these VEGF solutions.

As to the human serum, the $\chi_{ac,o}$ and $\chi_{ac,\phi}$ of the mixture of 60 $\mu$L serum and 60 $\mu$L magnetic reagent were detected using a magnetic immunoassay analyzer (XacPro-S, MagQu). Thus, the IMR signals can be obtained via (1) for human serum.

VEGF levels were detected using the Quantikine Human VEGF-ELISA kit (R&D Systems, Minneapolis, MN) [18]. 100 $\mu$L of rat serum and serially diluted standard solutions (VEGF) were added to 96-well microtiter plates precoated with murine anti-VEGF monoclonal antibodies and incubated at room temperature for 2 hours. After incubation, 200 $\mu$L of the secondary antibody, an enzyme-linked EGF-specific polyclonal goat antibody, was added, and then, incubation continued for 2 hours at room temperature. Substrate solution was added, and the reaction continued for 30 minutes. The optical density at a 450 nm wavelength is detected with an ELSIA reader.

(a)

(b)
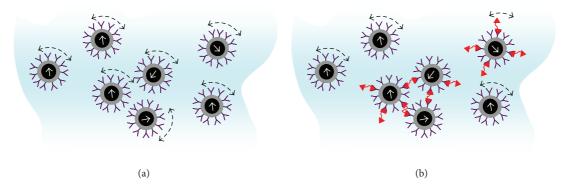
FIGURE 1: Illustration of the mechanism of immunomagnetic reduction (IMR).



(a)

(b)
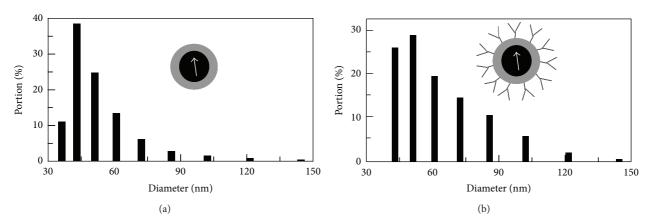
FIGURE 2: Distribution analysis for the hydrodynamic diameters of (a) dextran-coated $Fe_3O_4$ nanoparticles and (b) anti-VEGF functionalized $Fe_3O_4$ nanoparticles dispersed in PBS solution.
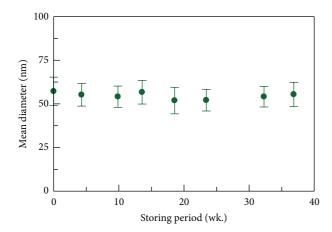


FIGURE 3: Time-evolution mean diameter of magnetic particles biofunctionalized with anti-VEGF and dispersed in PBS solution.
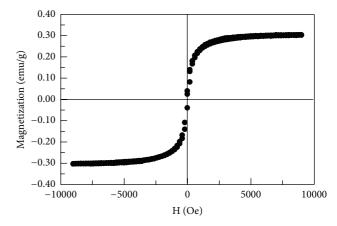


FIGURE 4: Magnetic hysteresis curve of magnetic nanoparticles functionalized with anti-VEGF and dispersed in PBS solution.

## 3. Results and Discussion

The optical density (OD) as a function of the VEGF concentration detected via ELISA was characterized, as shown with the crosses and the dashed line in Figure 5. The error bars are the standard deviations of the triple-test signals. It was found that OD almost remains constant as VEGF concentration $\phi_{VEGF}$ increases from 1 pg/mL to 23.4 pg/mL. As VEGF concentration $\phi_{VEGF}$ is higher than 46.9 pg/mL, a significant increase in OD is observed. The low-detection
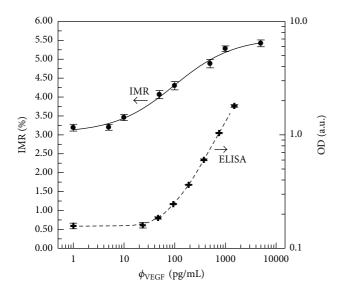
FIGURE 5: VEGF concentration dependent IMR signals (dots with the solid line) using immunomagnetic reduction (IMR) and OD (crosses with the dashed line) using ELISA.

limit in OD can be obtained by the addition of triple standard deviations (e.g., 3-sigma criterion) to the OD at low VEGF concentrations. The OD at 23.4 pg/mL VEGF is 0.160, and its standard deviation is 0.009. The low-detection limit in OD is $(0.160 + 3 \times 0.009)\% = 0.187\%$, which is very close to the OD at 46.9 pg/mL VEGF, that is, 0.185. This implies that the low-detection limit for assaying VEGF via ELISA is around 50 pg/mL. However, the cut-off concentration for VEGF in clinics is 50 pg/mL. The results shown by the dashed line in Figure 3 reveal that the ELISA is not sensitive enough to assay VEGF for patients in early-stage malignancy.

SQUID-based IMR is applied to characterize the VEGF concentration dependent IMR signals. The results are shown by the dots in Figure 5. The error bar at each VEGF concentration is the standard deviation of the triple-test IMR signals. Clearly, there is no difference in IMR signals (~3.2%) for $\phi_{VEGF}$ being 1 and 5 pg/mL. For $\phi_{VEGF}$ being 10 pg/mL, the IMR signal (~3.5%) definitely deviates from that of $\phi_{VEGF}$ being 1 or 5 pg/mL. The low-detection limit in IMR signals can be obtained by adding triple standard deviations (e.g. 3-sigma criterion) to the IMR signals at low VEGF concentrations. According to Figure 5, the IMR signal at 5 pg/mL VEGF is 3.20%, and its standard deviation is 0.08%. The low-detection limit in IMR signal turns to $(3.20 + 3 \times 0.08)\% = 3.44\%$., which is slightly lower than the IMR signal at 10 pg/mL VEGF, that is, 3.46%. Therefore, the low-detection limit for assaying VEGF using SQUID-based IMR is 10 pg/mL, which is lower than the clinical cut-off VEGF concentration 50 pg/mL. Hence, SQUID-based IMR would be good for early-stage diagnosis of malignancy.

As the VEGF concentration keeps increasing from 10 pg/mL, the IMR signal also increases and becomes saturated as the VEGF concentration is over 1000 pg/mL.

The VEGF concentration dependent IMR signals in Figure 3 exhibit such behavior of logistic function. Consider

$$IMR (\%) = \frac{A - B}{1 + (\phi_{VEGF}/\phi_o)^\gamma} + B, \qquad (2)$$

where $A$, $B$, $\phi_o$, and $\gamma$ are fitting parameters. By fitting dots in Figure 3 to (2), $A$ was found to be 3.05, $B$ was 5.56, $\phi_o$ equaled 98.84, and $\gamma$ was 0.74. The fitting curve of (2) is plotted by the solid curve in Figure 5. The coefficient of determination $R^2$ between the dots and the solid line is 0.993, denoting a high consistency between the experimental data (dots) and the fitting curve (solid line).

Note, the value of $A$ in (2) corresponds to the IMR signal at zero VEGF concentration. Theoretically, the value of $A$ should be zero. However, due to noises in the mixed-frequency ac magnetic susceptibility $\chi_{ac}$, a nonzero IMR signal is resulted, even if there is no VEGF molecules in the tested sample. Hence, the value of $A$ in (2) is not zero. The noises are attributed from two main factors. One factor is the electric noise generated by the immunoanalyzer. The other factor is referred to as bioreaction noise, which results from the dynamic balance of the association/dissociation between VEGF molecules and anti-VEGF functionalized magnetic nanoparticles.

For serum, there might be interfering materials due to hemolysis, jaundice, or hypertriglyceridemia, such as hemoglobin (Hb), conjugated bilirubin (C-BL), or triglyceride (TG). It is necessary to clarify the interference effects of these materials on assaying VEGF. Besides, biomarkers for other cancers like hepatocellular carcinoma (HCC) or colorectal cancer (CRC) are included for the interference tests. In clinics, the biomarker for HCC is alpha-fetoprotein (AFP), while carcinoembryonic antigen (CEA) is the biomarker for CRC. The cut-off concentrations for these interfering materials are listed in Table 1. When someone's serum contains a certain biomarker concentration exceeding its cut-off value, he or she is suffering from the corresponding disease. For example, if someone's serum contains Hb higher than 500 $\mu$g/mL, say 600 $\mu$g/mL, he or she is suffering from hemolysis. Table 1 shows that the concentrations of these interfering materials used for the interference tests are much higher than the cut-off concentrations. For comparison, the interference tests for VEGF were done using ELISA and IMR, respectively.

The 100 pg/mL VEGF solutions without or with interfering materials are used as test samples. The optical densities (OD) for these solutions are detected using ELISA and are plotted in Figure 6(a). The data of these ODs are listed in Table 2. In the experiment, the sample without interfering material (labeled with "None" in Figure 6(a)) is used as a reference. The OD of the reference sample was observed to be $0.31 \pm 0.01$. The samples with 1000 $\mu$g/mL Hb, 10 $\mu$g/mL C-BL, and 2000 $\mu$g/mL TG show distinctly higher OD's as compared to that of the reference sample, while the sample with 100 ng/mL AFP shows differentially lower OD. These results reveal the significant interference by biomolecules of Hb, C-BL, TG, and AFP for assaying VEGF using ELISA.

(a)



(b)
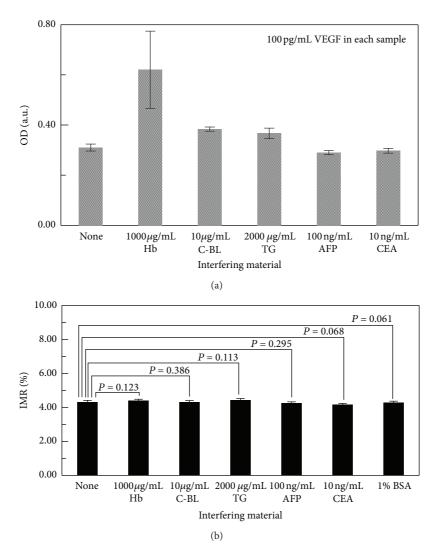
Figure 6: Interference tests for (a) ELISA and (b) IMR by interfering materials such as Hb, C-BL, TG, AFP, and CEA.

Table 1: Clinical cut-off concentrations and used concentrations in this work for interference tests due to hemoglobin (Hb), conjugated bilirubin (C-BL), triglyceride (TG), alpha-fetoprotein (AFP), and carcinoembryonic antigen (CEA).

| Disease | Hemolysis | Jaundice | Hypertriglyceridemia | Hepatocellular carcinoma | Colorectal cancer |
|---|---|---|---|---|---|
| Biomarker (as interfering material) | Hb | C-BL | TG | AFP | CEA |
| Cut-off concentration | 500 $\mu$g/mL | 2 $\mu$g/mL | 1500 $\mu$g/mL | 20 ng/mL | 5 ng/mL |
| Concentration used for interference test | 1000 $\mu$g/mL | 10 $\mu$g/mL | 2000 $\mu$g/mL | 100 ng/mL | 10 ng/mL |

As to the interference tests for IMR, the IMR signals for these VEGF solutions without or with interfering materials are detected and shown in Figure 6(b). One more interfering material, 1% bovine serum albumin (BSA), is used for the interference tests for IMR. The IMR signal for the reference sample, which consists of pure 100 pg/mL VEGF, was found to be (4.30 ± 0.11)%. The IMR signals of the other samples with interfering materials are listed in Table 2. There is hardly any difference in IMR signals between the samples with interfering material and the reference sample. A quantitative analysis of the consistency in IMR signals between samples with interfering materials and the reference sample was done

through $t$-test statistic analysis. A quantity, $P$ value, was calculated for the consistency in IMR signals between samples with interfering materials and the reference sample, as labeled in Figure 6(b). It was found that all $P$ values are higher than 0.05, meaning that there was no significant difference in IMR signals for VEGF solutions without interfering materials as compared to that of the pure VEGF solution.

In addition to the high specificity of antibodies against VEGF molecules, there are two important factors relevant to the high specificity in assaying VEGF using IMR. The first factor is that the signals detected using IMR are magnetic instead of optical for ELISA. The colors due to Hb, C-BL, or

TABLE 2: Experimental data of ODs and IMR signals for the interference tests using ELISA and IMR, respectively. The results are plotted in Figures 6(a) and 6(b).

| Interfering material | None | Hb | C-BL | TG | AFP | CEA | BSA |
|---|---|---|---|---|---|---|---|
| OD | $0.31 \pm 0.01$ | $0.62 \pm 0.15$ | $0.38 \pm 0.008$ | $0.37 \pm 0.02$ | $0.29 \pm 0.008$ | $0.29 \pm 0.01$ | — |
| IMR signal (%) | $4.30 \pm 0.11$ | $4.40 \pm 0.07$ | $4.32 \pm 0.07$ | $4.42 \pm 0.10$ | $4.26 \pm 0.07$ | $4.15 \pm 0.09$ | $4.28 \pm 0.08$ |

TG seriously affect the optical signals for ELISA but do nothing to with magnetic signals for IMR. The second factor is the suppression of nonspecific binding between antibodies and interfering molecules. Briefly speaking, the bound molecules with antibodies on magnetic particles experience centrifugal force because of the rotation of particles under external ac magnetic fields. The centrifugal force is enhanced under higher rotating frequencies. However, the binding force between anti-VEGF and non-specific molecules is weaker than that between anti-VEGF and specific molecules, that is, VEGF molecules. Thus, by suitably adjusting the frequencies of the external magnetic fields, the centrifugal force is strong enough to break out the binding between anti-VEGF and non-specific molecules but still weaker than the binding force between anti-VEGF and VEGF molecules. Therefore, the non-specific binding can be significantly depressed in IMR. Other examples for demonstrating the depression in the non-specific binding by adjusting the frequencies of the external magnetic fields are reported in [19].

With the relationship between the IMR signals and VEGF concentration, that is, IMR(%)-$\phi_{VEGF}$ curve, in Figure 5, the VEGF concentrations $\phi_{VEGF}$ in human serum are detected using IMR. The serum can be categorized into three groups. The first group is sixteen serum samples from people without tumors, denoted as the normal group. The second group is sixteen serum samples from patients with HCC, referred to as the HCC group. The third group is sixteen serum samples of patients with CRC, referred to as the CRC group. The detected VEGF concentrations $\phi_{VEGF}$ using IMR for these forty-eight serum samples are shown in Figure 7. It was found that the $\phi_{VEGF}$ for normal group ranges from 9 to 40 pg/mL, which is well below the cut-off concentration in clinics of 50 pg/mL. However, for either the HCC group or CRC group, $\phi_{VEGF}$ is much higher than 50 pg/mL. A clear difference in the VEGF concentration in serum is obtained between the normal group and cancer (HCC and CRC) group using IMR.

## 4. Conclusions

By utilizing magnetic nanoparticles biofunctionalized with anti-VEGF and the SQUID-based mixed-frequency ac magnetosusceptometer, the assay properties for VEGF using immunomagnetic reduction (IMR) technologies are investigated. The SQUID-based IMR shows an ultra-low detection limit and nonsignificant interference for assaying VEGF. Further, there is a clear difference in the detected VEGF concentration in the serum between the normal group and the cancer group with hepatocellular carcinoma or colorectal cancer. These results demonstrate the feasibility of achieving clinically high sensitivity and high specificity for diagnosing
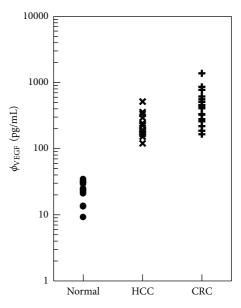


FIGURE 7: Detected VEGF concentrations in serum using SQUID-based IMR for normal people and patients with hepatocellular carcinoma (HCH) or colorectal cancer (CRC).

malignancy by assaying VEGF in serum using SQUID-based IMR.

## Acknowledgments

## References

[1] G. Viglietto, D. Maglione, M. Rambaldi et al., "Upregulation of vascular endothelial growth factor (VEGF) and downregulation of placenta growth factor (PIGF) associated with malignancy in human thyroid tumors and cell lines," *Oncogene*, vol. 11, no. 8, pp. 1569–1579, 1995.

[2] K. Podar and K. C. Anderson, "The pathophysiologic role of VEGF in hematologic malignancies: therapeutic implications," *Blood*, vol. 105, no. 4, pp. 1383–1395, 2005.

[3] R. S. Finn and A. X. Zhu, "Targeting angiogenesis in hepatocellular carcinoma: focus on VEGF and bevacizumab," *Expert Review of Anticancer Therapy*, vol. 9, no. 4, pp. 503–509, 2009.

[4] R. Bendardaf, A. Buhmeida, M. Hilska et al., "VEGF-1 expression in colorectal cancer is associated with disease localization, stage, and long-term disease-specific survival," *Anticancer Research*, vol. 28, no. 6 B, pp. 3865–3870, 2008.

[5] I. Hyodo, T. Doi, H. Endo et al., "Clinical significance of plasma vascular endothelial growth factor in gastrointestinal cancer," *European Journal of Cancer*, vol. 34, no. 13, pp. 2041–2045, 1998.

[6] K. Werther, I. J. Christensen, H. J. Nielsen et al., "Prognostic impact of matched preoperative plasma and serum VEGF in patients with primary colorectal carcinoma," *British Journal of Cancer*, vol. 86, no. 3, pp. 417–423, 2002.

[7] F. M. Belgore, A. D. Blann, and G. Y. Lip, "Measurement of free and complexed soluble vascular endothelial growth factor receptor, Flt-1, in fluid samples: development and application of two new immunoassays," *Clinical Science*, vol. 100, no. 5, pp. 567–575, 2001.

[8] S. Ponticelli, A. Braca, N. De Tommasi, and S. De Falco, "Competitive ELISA-based screening of plant derivatives for the inhibition of VEGF family members interaction with vascular endothelial growth factor receptor 1," *Planta Medica*, vol. 74, no. 4, pp. 401–406, 2008.

[9] S. Greenberger, E. Boscolo, I. Adini, J. B. Mulliken, and J. Bischoff, "Corticosteroid suppression of VEGF-A in infantile hemangioma-derived stem cells," *The New England Journal of Medicine*, vol. 362, no. 11, pp. 1005–1013, 2010.

[10] K. W. Huang, S. Y. Yang, Y. W. Hong et al., "Feasibility studies for assaying alpha-fetoprotein using antibody-activated magnetic nanoparticles," *International Journal of Nanomedicine*, vol. 7, pp. 1991–1996, 2012.

[11] J. J. Chieh, S. Y. Yang, Z. F. Jian et al., "Hyper-high-sensitivity wash-free magnetoreduction assay on biomolecules using high-$T_c$ superconducting quantum interference devices," *Journal of Applied Physics*, vol. 103, no. 1, Article ID 014703, pp. 1–6, 2008.

[12] J. J. Chieh, S.-Y. Yang, H.-E. Horng et al., "Immunomagnetic reduction assay using high-$T_c$ superconducting-quantum-interference-device-based magnetosusceptometry," *Journal of Applied Physics*, vol. 107, no. 7, Article ID 074903, pp. 1–5, 2010.

[13] C. C. Yang, S. Y. Yang, J. J. Chieh et al., "Biofunctionalized magnetic nanoparticles for specifically detecting biomarkers of Alzheimer's Disease in vitro," *ACS Chemical Neuroscience*, vol. 2, pp. 500–505, 2011.

[14] M. J. Chiu, H. E. Horng, J. J. Chieh et al., "Multi-channel squid-based ultra-high-sensitivity *in-vitro* detections for bio-markers of alzheimer's disease via immunomagnetic reduction," *IEEE Transactions on Applied Superconductivity*, vol. 21, no. 3, pp. 477–480, 2011.

[15] C. C. Yang, S. Y. Yang, H. H. Chen et al., "Effect of molecule-particle binding on the reduction in the mixed-frequency ac magnetic susceptibility of magnetic bio-reagents," *Journal of Applied Physics*, vol. 112, pp. 24704-1–24704-4, 2012.

[16] W. Jiang, H. C. Yang, S. Y. Yang et al., "Preparation and properties of superparamagnetic nanoparticles with narrow size distribution and biocompatible," *Journal of Magnetism and Magnetic Materials*, vol. 283, no. 2-3, pp. 210–214, 2004.

[17] S. Y. Yang, Z. F. Jian, H. E. Horng et al., "Dual immobilization and magnetic manipulation of magnetic nanoparticles," *Journal of Magnetism and Magnetic Materials*, vol. 320, no. 21, pp. 2688–2691, 2008.

[18] M. C. Wergin and B. Kazer-Hotz, "Plasma vascular endothelial growth factor (VEGF) measured in seventy dogs with spontaneously occuring tumours," *In Vivo*, vol. 18, no. 1, pp. 15–20, 2004.

[19] S. Y. Yang, W. C. Wang, C. B. Lan et al., "Magnetically enhanced high-specificity virus detection using bio-activated magnetic nanoparticles with antibodies as labeling markers," *Journal of Virological Methods*, vol. 164, no. 1-2, pp. 14–18, 2010.

*Research Article*

# High Temperature Magnetic Properties of Indirect Exchange Spring FePt/M(Cu,C)/Fe Trilayer Thin Films

**Anabil Gayen,[1] Barnali Biswas,[1] Akhilesh Kumar Singh,[1]**
**Padmanapan Saravanan,[2] and Alagarsamy Perumal[1]**

[1] *Department of Physics, Indian Institute of Technology Guwahati, Guwahati 781039, India*
[2] *Defence Metallurgical Research Laboratory, Hyderabad 500058, India*

Correspondence should be addressed to Alagarsamy Perumal; alagarsamy.perumal@gmail.com

We report the investigation of temperature dependent magnetic properties of FePt and FePt(30)/M(Cu,C)/Fe(5) trilayer thin films prepared by using magnetron sputtering technique at ambient temperature and postannealed at different temperatures. $L1_0$ ordering, hard magnetic properties, and thermal stability of FePt films are improved with increasing postannealing temperature. In FePt/M/Fe trilayer, the formation of interlayer exchange coupling between magnetic layers depends on interlayer materials and interface morphology. In FePt/C/Fe trilayer, when the C interlayer thickness was about 0.5 nm, a strong interlayer exchange coupling between hard and soft layers was achieved, and saturation magnetization was enhanced considerably after using interlayer exchange coupling with Fe. In addition, incoherent magnetization reversal process observed in FePt/Fe films changes into coherent switching process in FePt/C/Fe films giving rise to a single hysteresis loop. High temperature magnetic studies up to 573 K reveal that the effective reduction in the coercivity decreases largely from 34 Oe/K for FePt/Fe film to 13 Oe/K for FePt/C(0.5)/Fe film demonstrating that the interlayer exchange coupling seems to be a promising approach to improve the stability of hard magnetic properties at high temperatures, which is suitable for high-performance magnets and thermally assisted magnetic recording media.

## 1. Introduction

The development of futuristic magnetic devices such as biasing nanomagnets and exchange coupled nanocomposite magnet in microelectromagnetic devices, and ultra-high-density magnetic storage media, strongly depends on progress of performance of hard magnetic thin films [1–3]. In order to improve the hard magnetic properties and to attain large thermal stability, single domain magnetic particles with high magnetic anisotropy energy are indispensable [4]. Hence, the single domain particles are of great interest, and extensive research work has been carried out recently to search for suitable thin films with magnetic alloys having large magnetic anisotropy energy from the standpoint of high density magnetic recording technology and permanent magnet applications [5–10]. It is well known that the permanent magnet, an essential component in modern technology, is an important magnetic material whose main application is

to provide magnetic fluxes and to be used as a magnetic media. The key character is maximum high energy product, which is markedly dependent on remanent magnetization and coercivity ($H_C$). For instance, SmCo and NdFeB alloys with complex crystal structures are widely being used as permanent magnets with an idea of exchange coupling between the transition metal and rare earth atoms with strong uniaxial anisotropy [11, 12]. This provided a maximum energy of 55 MGOe for an NdFeB alloy, while its theoretical value is calculated to be 64 MGOe. Recently, $L1_0$ ordered equiatomic Fe(Co)Pt alloy is also considered as one of the most promising candidates for hard magnet applications because of its extremely high magnetic anisotropy energy ($K_u \sim 10^8$ erg/cc). Since high $K_u$ materials can produce large $H_C$, attempts were shown to fabricate FePt based alloys in the form of chemically synthesized nanoparticles, isolated island particles, epitaxially grown single crystal films, and granular films [13–15]. Nevertheless, the maximum energy product in

thin films is limited by $M_S$, and hence the permanent magnet with high-energy product is not available mainly because of a trade-off in obtaining large $H_C$ and high $M_S$.

On the other hand, Coehoorn et al. [16] and Kneller and Hawig [17] proposed the exchange spring magnet, based on an interfacial exchange coupling of two nanostructured phases combining a hard magnetic material in order to provide large $H_C$ and a soft magnetic material to provide high $M_S$, as a way to create a next generation high performance permanent magnet and magnetic recording media. Since then many investigations have been carried out using various hard (Sm-Co, FePt, and Co-Pt) and soft (Fe, Co, and Fe-Co, $Fe_3Pt$) ferromagnetic (FM) phases to achieve high energy product [15, 18–27]. It has been predicted theoretically that FePt based nanocomposite shows an energy product of 90 MGOe [28, 29]. However, a maximum energy product of 52.8 MGOe was achieved experimentally by Liu et al. [18] in FePt/$Fe_3Pt$ nanocomposite thin film with rapid annealing process. A careful review on FePt films reveals that these films display large $H_C$ (>30 kOe) in very thin island-like films and particulate films [5, 30, 31], but $H_C$ drops down drastically when they become continuous [15, 32]. These results confirm that FePt films with high $L1_0$ ordering show very high $H_C$ and the introduction of proper exchange coupling using soft magnets should improve the high energy product.

Up to now most of the attempts in exchange spring have been executed by coupling the soft FM phase directly to the hard FM phase and studied the effects of bilayer and multilayer structures and various heat treatment process on the improvement of properties of nanocomposite magnets. Recently, interlayer exchange coupling using two FM films, hard and soft magnets, separated by a thin nonmagnetic layer, resulting in an indirect exchange coupling between the FM layers, was reported to construct an exchange spring [33]. The advantages of such coupling are (i) coherent interface is not necessary, and (ii) interface diffusion may not have serious effects on the exchange coupling. Besides, to use as a desirable magnet and for the application of high density magnetic recording media, both intrinsic (high $M_S$, high Curie temperature, and high $K_u$) and extrinsic (high energy product, high $H_C$, thermal stability, and corrosion stability) properties should be characterized. However, no systematic investigations on the indirect exchange spring have been reported. Since the fundamental magnetic properties of FePt films are very sensitive to chemical ordering and microstructure, thermal stability of FePt particles against temperature is also expected to show strong dependence on chemical ordering. Nevertheless, only a few reports have been published on the role of chemical ordering on the thermal stability and high temperature magnetic properties of FePt based single domain particles [34, 35] and their applications in indirect exchange spring nanocomposite magnets. Therefore, in this work, we have studied (i) the effect of chemical ordering on the high temperature magnetic properties of FePt polycrystalline films fabricated on low cost substrates, (ii) the formation of interlayer exchange coupling in indirect exchange spring, and (iii) their effects on the stability of magnetic properties at high temperature, by fabricating FePt(30 nm)/M($x$ nm)/Fe(5 nm)

nanocomposite thin films with Cu and C as a nonmagnetic layer for the first time.

## 2. Materials and Methods

FePt films with various thicknesses ranging from 10 to 50 nm were prepared by sputtering a high purity Fe target with Pt pellets on it on low cost substrates. This gives a homogenous single layer FePt film, and composition of FePt was optimized by adjusting number of Pt pellets on Fe target. Thermally oxidized Si and Si(111) wafers were used as substrates. All the films were deposited at ambient temperature and postannealed at high temperatures (450 and 550°C) for 45 minutes under a high vacuum to induce face centered tetragonal (*fct*) structure. The base pressure of the chamber was better than $3 \times 10^{-5}$ Pa and the high purity argon of 10 mTorr for FePt and Fe, 20 mTorr for C and 8 mTorr for Cu was flown during the sputtering. A series of FePt(30 nm)/M($x$ nm)/Fe(5 nm) (M = Cu and C, and $x$ = 0, 0.25, 0.5, 1, 2, and 4 nm) trilayer films were deposited by sputtering FePt, M, and Fe targets at ambient temperature and postannealed at 550°C. The nominal thicknesses of the FePt, M, and Fe films were controlled based on precalibrated sputtering rates of the FePt, M, and Fe, respectively. Crystal structure and film structure were examined by X-ray diffraction (XRD) using a Rigaku TTRAX diffractometer with Cu-$K_\alpha$ radiation ($\lambda$ = 1.5405 Å) and transmission electron microscopy (TEM). Compositions, estimated using energy dispersive X-ray spectroscopy attached to a scanning electron microscope (SEM, Leo 1430VP), were about $Fe_{49}Pt_{51}$ for all the films. Room temperature and temperature dependent magnetic properties were analyzed by using vibrating sample magnetometer (VSM, Model: Lakeshore 7410, USA) in the temperature range 300 K to 800 K by measuring magnetic hysteresis (*M-H*) loops at different temperatures.

## 3. Results and Discussion

*3.1. Magnetic Properties of FePt Films.* To optimize the magnetic properties and to study the thermal stability of single layer FePt films, *M-H* loops were measured at room temperature and at high temperatures. Figure 1 depicts the variations of $H_C(T)$ for FePt films with 30 and 50 nm thicknesses grown on oxidized Si substrate at ambient temperature and annealed at two different temperatures (450 and 550°C). $(M\text{-}H)_T$ loops measured at different temperatures for FePt(50 nm) film annealed at 450°C are displayed in inset of Figure 1. It is clear from the figure that room temperature magnetization of FePt film obtained at 20 kOe field is around 530 emu/cc, which is quite low as compared to its bulk value ($M_S$-1140 emu/cc). While the exact mechanism responsible for the pronounced loss in saturation magnetization in FePt film is unclear, the observed results can be attributed to one of the following reasons: (i) the observation of nonsaturated hysteresis curve for the applied field of 20 kOe, (ii) size dependent chemical ordering in FePt films with different thicknesses [36–38], (iii) incomplete structural phase transition from face-centered cubic (*fcc*) structure in as-deposited film to *fct* structure in annealed films [39], (iv) reduced magnetization on the
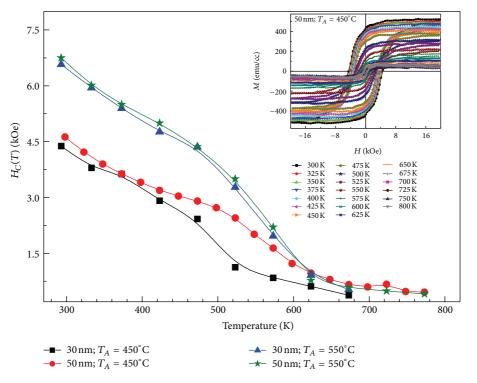
FIGURE 1: (Color online) Variations of coercivity with temperature in the temperature range 300 K and 800 K for the FePt films prepared on thermally oxidized Si substrates at ambient temperature and postannealed at different temperatures. Inset: Typical $M$-$H$ loops obtained at different temperatures between 300 K and 800 K for FePt(50 nm) film annealed at 450°C.

surfaces [38], and (v) the formation of magnetically deadlayer at the substrate film interface or possible oxidation of the FePt surface during post annealing process, resulting an overall reduction in FePt film thickness [40]. Nevertheless, the observed room temperature magnetization in the presently investigated films is in agreement with the earlier reports ($M_S \sim 610$ emu/cc) on similar system (FePt(50 nm)) [39]. In addition, $H_C$ of FePt films at room temperature shows a strong dependence of annealing temperature, which can be attributed to an increase in chemical ordering of $L1_0$ phase. The improvement in the chemical ordering was also confirmed from structural analysis (not shown here) that (i) the ratio of integrated intensities between the superlattice (001) peak and the fundamental (002) peak increases and (ii) the peak position of the (001) superlattice peak ((002) fundamental peak) shifts slightly to higher angles with increasing post annealing temperature. Another feature observed from Figure 1 is that $H_C(T)$ shows a substantial thickness dependent for the samples annealed at low temperature, while the samples annealed at high temperature follow a similar trend for different film thicknesses. This can be attributed to size dependent chemical ordering in FePt films with different thicknesses [36–38]. It is generally understood that $H_C$ variation in FePt films is not only affected by the ordered volume fraction [41, 42], but also by a microstructural factor, that is related to the ordered volume fraction and that scales similarly. Defects, such as grain boundaries and phase boundaries, in the magnetic materials can form pinning sites, which impede the domain walls and leading to an enhancement in

$H_C$. In addition, the boundaries between the ordered and disordered regions might also represent domain wall pinning sites and responsible for high $H_C$. In order to understand the effect of post annealing on the thermal stability of FePt films, $H_C(T)$ data are analyzed using Sharrock's equation [43–46], given as

$$H_r(t, T) = H_o \left\{ 1 - \left[ \left( \frac{k_B T}{E_b} \right) \ln \left( \frac{f_o t}{\ln 2} \right) \right]^n \right\}, \quad (1)$$

where $H_r$ is remanent coercivity dependent upon field exposure time $t$ and temperature $T$. $H_o$ is intrinsic coercivity without thermal agitation, $k_B$ is the Boltzmann's constant, $f_o$ is attempt frequency, $t$ is time of hysteresis measurement, and $E_b$ is energy barrier at zero field. The value of $n$ is taken as 2/3 by assuming slightly unaligned particles [47, 48]. The attempt frequency $f_o$ and the hysteresis measurement time are taken as $10^{10}$ Hz and 1 second, respectively. Figure 2 depicts the applicability of Sharrock's equation on $H_C(T)$ data for FePt films. The fitting resulted the energy barrier values of 1.40 eV and 1.61 eV for FePt films of 30 and 50 nm annealed at 450°C, and 1.96 eV and 2.02 eV for FePt films of 30 and 50 nm annealed at 550°C, respectively. This reveals the corresponding thermal stability (the ratio between the energy barrier ($E_b$) to thermal energy ($k_B T$) at room temperature) of about 54 and 63 for FePt films of 30 and 50 nm annealed at 450°C and 76 and 78 for FePt films of 30 and 50 nm annealed at 550°C, respectively. These results confirm that the values of energy barrier increase considerably with the annealing
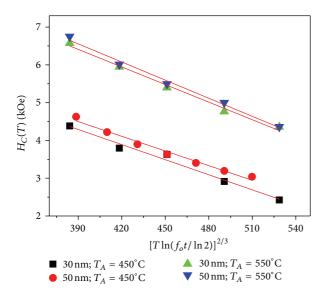
FIGURE 2: (Color online) Coercivity as a function of $[T\ln(f_o t/\ln 2)]^{2/3}$ for the FePt films annealed at different temperatures.

temperature. Since the FePt films annealed at 550°C show enhanced properties, we have taken FePt(30 nm) film for the study of indirect exchange spring by fabricating the FePt and Fe with different nonmagnetic interlayers.

*3.2. FePt/M/Fe Trilayer System.* To investigate the indirect exchange spring in FePt film and to study their temperature dependent magnetic properties and the thermal stability, FePt(30 nm)/M($x$ nm)/Fe(5 nm) trilayer films with $x = 0$, 0.25, 0.5, 1, 2, and 4 nm, and different intermediate layers using C and Cu were fabricated on Si(111) substrates. Figure 3 shows the XRD patterns of trilayer films with different Cu and C thicknesses deposited at ambient temperature and postannealed at 550°C. It is evident from the figure that superlattice diffraction line of (001) is observed around $2\theta = 24°$, and all the films are $L1_0$ ordered with *fct* structure after post annealing. The other unlabeled diffractions peaks are due to the Si substrate. The relative integrated intensities of (001) and (111) peaks reveal that the films have a weak preferred orientation to [001], that is, in the perpendicular direction to the film plane [15, 49]. Note that none of the XRD patterns in fact showed any diffraction peak of Fe layer or any information about the Fe and the nonmagnetic interlayers. Figure 4 shows the room temperature *M-H* loops of FePt(30)/M($x$)/Fe(5) trilayer films. For the films with no nonmagnetic interlayer, *M-H* loop exhibits a clear kink in second quadrant due to an incoherent or separate magnetic reversal process suggesting that there is a weak FM coupling or no coupling between the hard and soft layers [22, 33]. With increasing Cu layer thickness, the kink observed in bilayer film reduces gradually up to 4 nm without a much change in $M_S$ values. In addition, the magnetic field required for saturating the films ($H_{sat}$) and $H_C$ decreases significantly with increasing the Cu layer thickness. On the other hand, the introduction of C interlayer interestingly exhibits different properties. (i) With increasing the C to 0.25 nm, the kink



(a)



(b)
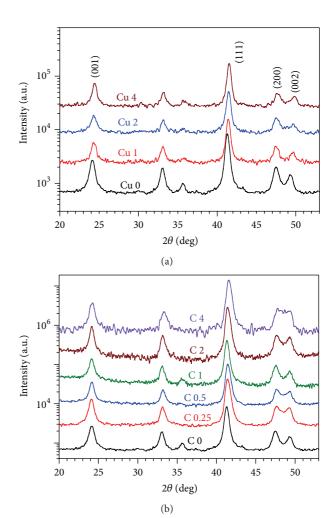
FIGURE 3: (Color online) XRD patterns for FePt(30 nm)/M($x$ nm)/ Fe(5 nm) trilayer films with M-Cu (a) and C (b) and $x = 0$–4 prepared on Si(111) substrates at ambient temperature and postannealed at 550°C.

in the second quadrant slightly reduces, but $H_{sat}$ decreases noticeably. (ii) When the C thickness is increased to 0.5 nm, the kink in the loop disappears, and *M-H* loop exhibits a single hysteresis with almost rectangular shape. This confirms a strong interlayer FM exchange coupling between the FePt and Fe layers through C interlayer. (iii) Remarkably, $M_S$ value is increased to 990 emu/cc, which is much higher than that of pure FePt single layer films obtained in the present investigation. (iv) On further increasing the C layer thickness up to 4 nm, the shape of the *M-H* loop and values of $M_S$ remain same, but the values of $H_C$ and $H_{sat}$ decrease gradually. To understand the effect of interlayer thickness on the magnetic parameters, the values of $H_C$, $M_S$, and $H_{sat}$ were extracted from the loops and depicted in Figure 5 for FePt(30)/M($x$)/Fe(5) trilayer films. It is observed that $H_C$ and $H_{sat}$ decrease largely for the initial increase in C thickness up to 1 nm and exhibits gradual decrease for the higher C thickness. On the other hand, $M_S$ values increases quickly to 990 emu/cc for C thickness up to 1 nm and remains almost constant for larger C thicknesses. In the case of Cu
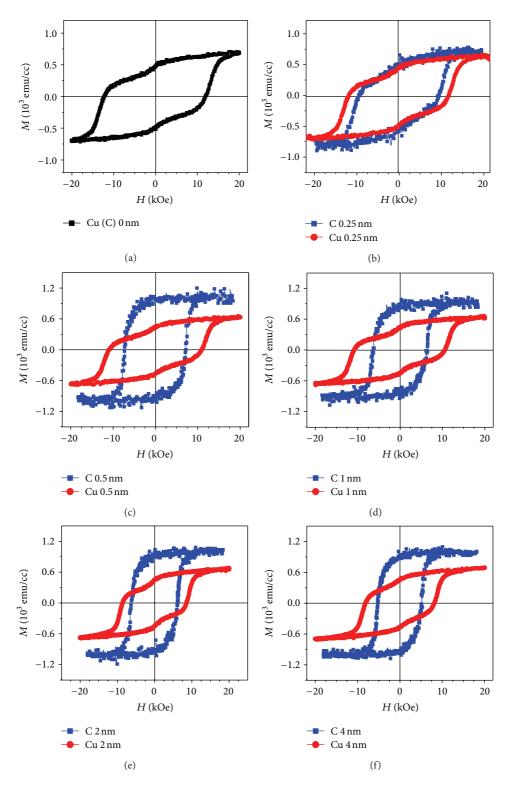
Figure 4: (Color online) Room temperature $M$-$H$ loops of FePt(30 nm)/M($x$ nm)/Fe(5 nm) trilayer films with M-Cu and C and $x = 0$–4 nm prepared on Si(111) substrates at ambient temperature and postannealed at 550°C.

interlayer, both $H_C$ and $H_{sat}$ exhibit a slow decrease up to 1 nm and a larger change for higher thicknesses. In addition, $M_S$ decreased initially up to 0.5 nm and started increasing with increasing the Cu thickness.

The observed results suggest that the interlayer FM exchange coupling between the FePt and Fe layers strongly depends on the type of materials used as interlayers and their thickness, and interface morphology [33, 50]. All the trilayer

(a)



(b)



(c)
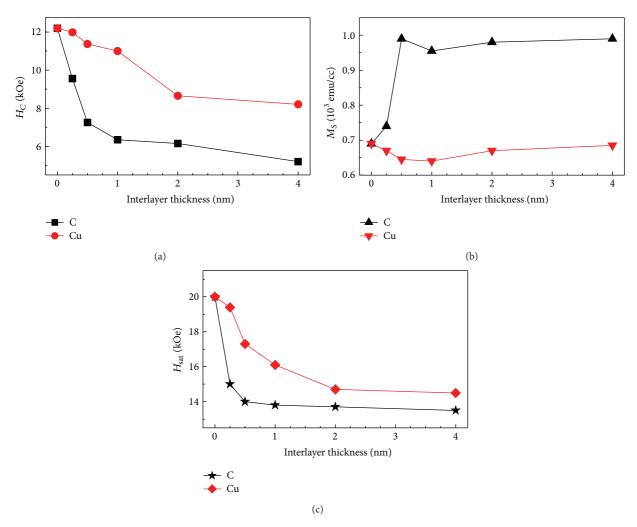
Figure 5: (Color online) Variations of (a) coercivity, (b) saturation magnetization, and (c) applied magnetic field required for saturating the films with different interlayer thicknesses of FePt(30 nm)/M($x$ nm)/Fe(5 nm) trilayer films with M-Cu and C and $x = 0$–4 nm prepared on Si(111) substrates at ambient temperature and postannealed at 550°C.

films were prepared at room temperature and postannealed at 550°C. It is known that the post annealing may cause a possible interdiffusion between the layers in multilayer films resulting a change in interface morphology [51]. Also, the growth morphology of FePt films with annealing may provide inhomogeneous interface morphology to the subsequent layers [50]. Since the trilayer films with Cu interlayer did not show a considerable change in the magnetic properties, this may be correlated to a possible inter-diffusion across the interlayers resulting an unclear interface between hard and soft layers [51], when the Cu thickness is less than 1 nm. Although the kink observed in the second quadrant weakens slowly due to a thick Cu interlayer at higher thickness, the formation of interlayer exchange coupling was not at all observed for Cu thickness up to 4 nm. On the other hand, the introduction of C between the hard and soft phases is expected to provide stable interfaces even after annealing [52]. Hence, the hard and soft phases are clearly separated by the C interlayer, which induces the interlayer exchange coupling resulting a coherent switching process and giving

rise to a single hysteresis loop. The appearance of incoherent or separate magnetization reversal process in the bilayer films may be correlated to the growth morphology of FePt [50] or to the higher thickness of the soft layer [15, 22]. The interface analysis reported by Casoli et al. [50] on the FePt/Fe bilayer films reveals that (i) for homogeneous and pseudocontinuous FePt layers, Fe layers grow epitaxially on FePt resulting a strong exchange coupling, (ii) but the FePt film grown at high substrate temperature exhibits island-like morphology where the Fe shows a more disordered structure due to considerable amount of Fe grows directly on the substrate, and thus the system behaves as an incoherent reversal process for high Fe layer thickness. On the other hand, Rheem et al. [52] reported that the robust interlayer exchange coupling obtained in the FePt(30)/FeCo(10)/FePt(30) tri-layers is improved initially by introducing a thinner C/Ta interlayer, but eventually degraded at larger thicknesses. They also correlated that the degradation of the exchange coupling is mainly due to the formation of continuous TaC films between the hard and soft layers. Jiang et al. [33]
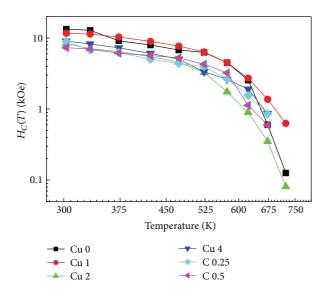
FIGURE 6: (Color online) Variations of coercivity with temperature for FePt(30 nm)/M($x$ nm)/Fe(5 nm) trilayer films with M-Cu (0, 1, 2, and 4) and C (0.25 and 0.5 nm) prepared on Si(111) substrates at ambient temperature and postannealed at $550°C$.

reported the indirect exchange between FePt and Fe using Ru interlayer, where the introduction of a thin Ru layer improves the existence of weak FM coupling into strong FM exchange coupling. The observed results in the presently investigated FePt/C/Fe trilayers are in agreement with the results observed in FePt/Ru/Fe trilayer films [33]. However, it is important to mention that the formation of exchange coupling between FePt and Fe was observed even for the 4 nm thick C interlayer. This value is significantly larger than the value reported in FePt/Ru/Fe trilayer films. Herndon et al. [53] reported the effect of nonmagnetic ($Al_2O_3$) spacer layer thickness on magnetic interactions of self-assembled single domain iron nanoparticles separated by $Al_2O_3$ spacer layer, and the variation of observed magnetic properties has been attributed to three types of magnetic interactions: exchange, strong dipolar, and weak dipolar depending on the spacer layer thickness. This revealed a dominance of exchange type interaction between two ferromagnetic layers when the nonmagnetic spacer layer thickness is less than 6 nm. In order to form an interlayer exchange coupling [54], a ferromagnetic coupling between hard and soft layers with preferred orientation of magnetization without much interdiffusion across the interface is necessary [33]. Since the introduction of C provides a stable interface between FePt and Fe layers, the ferromagnetic coupling between them generates a possible interlayer exchange coupling even at 4 nm thick C interlayer. Nevertheless, a systematic investigation of interlayer thickness dependent exchange coupling over a wide range of interlayer thicknesses is required to obtain more insight of interlayer exchange coupling.

To understand the effect of interlayer exchange coupling between hard and soft phases on the $H_C(T)$ in FePt/M/Fe trilayers, $(M\text{-}H)_T$ loops were observed at different constant

temperatures, and the extracted values of $H_C(T)$ are plotted as a function of temperature in Figure 6 for different Cu and C interlayers. $H_C(T)$ decreases gradually with increasing temperature up to 600 K as expected for a typical FM material. This is mainly due to the reduction in the magnetocrystalline anisotropy energy with increasing temperature. On further increasing the temperature above 600 K, $H_C(T)$ decreases largely due to instability of $L1_0$ ordered state, and finally they exhibit soft magnetic properties. In order to correlate the effect of interlayer exchange coupling on the magnetic properties, the effective reduction in $H_C(T)$ data for various interlayer thicknesses was analyzed carefully. It is revealed that in the temperature range between 300 K and 573 K, $H_C(T)$ decreases from 34 Oe/K for $x = 0$ to 25 Oe/K and 22 Oe/K for $x = 1$ and 2 nm, respectively, in FePt/Cu($x$)/Fe films. Similarly, in FePt/C($x$)/Fe films, $H_C$ reduces from 34 Oe/K for $x = 0$ to 15 Oe/K and 13 Oe/K for $x = 0.25$ and 0.5 nm, respectively. The above results provide a clear evidence that the interlayer FM exchange coupling between the hard and soft phases through a nonmagnetic film plays a major control on the stability of the hard magnetic properties of FePt films at higher temperatures leading to a sluggish decrease in $H_C(T)$. However, a careful analysis of $H_C(T)$ study at different Fe layer thicknesses in FePt/C/Fe trilayer films would reveal a detailed information on the effects of interlayer exchange coupling and the role of different amount of soft phases on the FePt hard magnetic properties and their possible applications in permanent magnet and thermally assisted magnetic recording media.

## 4. Conclusion

We have investigated the high temperature magnetic properties of pure FePt thin films and indirect exchange spring FePt/M/Fe trilayer through various interlayers at different interlayer thicknesses. It is perceived that the interlayer exchange coupling between the hard and soft magnetic phases through the nonmagnetic layer strongly depends on the interlayer materials and their thicknesses. When the C interlayer thickness was about 0.5 nm, a strong interlayer exchange coupling between FePt and Fe has been realized, and the saturation magnetization was largely improved. High temperature magnetic properties of the FePt/C/Fe trilayer films suggest that the stability of the hard magnetic properties of the FePt films are improved by the interlayer exchange coupling, as compared to the bilayer FePt/Fe films. The observed results provide a promising way in making exchange spring in future for the applications in permanent magnet and thermally assisted magnetic recording media.

## Acknowledgments

# References

[1] D. Sellmyer and R. Skomski, *Advanced Magnetic Nanostructures,*, Springer, New York, NY, USA, 2010.

[2] J. P. Liu, E. Fullerton, and O. Gutfleish, *Nanoscale Magnetic Materials and Applications*, Springer, New York, NY, USA, 2009.

[3] T. Shima and K. Takanashi, *Hard Magnetic Films in Handbook of Magnetism and Advanced Magnetic Materials: Novel Materials, Part 6*, Wiley-Interscience, 2007, Edited by, H. Kronmuller and S. S. P. Parkin.

[4] D. Weller, A. Moser, L. Folks et al., "High ku materials approach to 100 gbits/in2," *IEEE Transactions on Magnetics*, vol. 36, no. 1, pp. 10–15, 2000.

[5] T. Shima, K. Takanashi, Y. K. Takahashi, and K. Hono, "Coercivity exceeding 100 kOe in epltaxially grown FePt sputtered films," *Applied Physics Letters*, vol. 85, no. 13, pp. 2571–2573, 2004.

[6] H. Shima, K. Oikawa, A. Fujita, K. Fukamichi, and K. Ishida, "Large magnetocrystalline anisotropy energy of L10-type Co100-xPtx bulk single crystals prepared under compressive stress," *Applied Physics Letters*, vol. 86, no. 11, Article ID 112515, pp. 1–3, 2005.

[7] J. Sayama, T. Asahi, K. Mizutani, and T. Osaka, "Newly developed SmCo5 thin film with perpendicular magnetic anisotropy," *Journal of Physics D*, vol. 37, no. 1, p. L1, 2004.

[8] L. K. E. B. Serrona, A. Sugimura, N. Adachi et al., "Structure and magnetic properties of high coercive NdFeB films with a perpendicular anisotropy," *Applied Physics Letters*, vol. 82, no. 11, pp. 1751–1753, 2003.

[9] A. Singh, V. Neu, S. Fähler, K. Nenkov, L. Schultz, and B. Holzapfel, "Mechanism of coercivity in epitaxial Sm Co5 thin films," *Physical Review B*, vol. 77, no. 10, Article ID 104443, 2008.

[10] E. Stilp, J. Freudenberger, M. Seifert et al., "Probing the anisotropy constants of SmCo5 and PrCo5 by Hall resistance measurements in pulsed high magnetic fields up to 47 T," *Journal of Magnetism and Magnetic Materials*, vol. 324, no. 9, pp. 1711–1714, 2012.

[11] K. Hono and H. Sepehri-Amin, "Strategy for high-coercivity Nd–Fe–B magnets," *Scripta Materialia*, vol. 67, p. 503, 2012.

[12] P. Saravanan, M. Premkumar, A. K. Singh, R. Gopalan, and V. Chandrasekaran, "Study on morphology and magnetic behavior of SmCo5 and SmCo5/Fe nanoparticles synthesized by surfactant-assisted ball milling," *Journal of Alloys and Compounds*, vol. 480, no. 2, pp. 645–649, 2009.

[13] S. Sun, "Recent advances in chemical synthesis, self-assembly, and applications of FePt nanoparticles," *Advanced Materials*, vol. 18, no. 4, pp. 393–403, 2006.

[14] M. Kim, S. Shin, and K. Kang, "Ordering of island-like FePt L10 thin films," *Applied Physics Letters*, vol. 80, no. 20, pp. 3802–3804, 2002.

[15] Y. K. Takahashi, T. O. Seki, K. Hono, T. Shima, and K. Takanashi, "Microstructure and magnetic properties of FePt and Fe/FePt polycrystalline films with high coercivity," *Journal of Applied Physics*, vol. 96, no. 1, pp. 475–481, 2004.

[16] R. Coehoorn, D. B. de Mooij, and C. de Waard, "Meltspun permanent magnet materials containing Fe3B as the main phase," *Journal of Magnetism and Magnetic Materials*, vol. 80, no. 1, pp. 101–104, 1989.

[17] E. F. Kneller and R. Hawig, "The exchange-spring magnet: a new material principle for permanent magnets," *IEEE Transactions on Magnetics*, vol. 27, no. 4, pp. 3588–3600, 1991.

[18] J. P. Liu, C. P. Luo, Y. Liu, and D. J. Sellmyer, "High energy products in rapidly annealed nanoscale Fe/Pt multilayers," *Applied Physics Letters*, vol. 72, no. 4, pp. 483–485, 1998.

[19] T. Schrefl, H. Forster, R. Dittrich, D. Suess, W. Scholz, and J. Fidler, "Reversible magnetization processes and energy density product in Sm-CoFe and Sm-Co/Co bilayers," *Journal of Applied Physics*, vol. 93, no. 10, pp. 6489–6491, 2003.

[20] J. E. Davies, O. Hellwig, E. E. Fullerton et al., "Anisotropy dependence of irreversible switching in Fe/SmCo and FeNi/FePt exchange spring magnet films," *Applied Physics Letters*, vol. 86, no. 26, Article ID 262503, pp. 1–3, 2005.

[21] Y. Choi, J. S. Jiang, J. E. Pearson et al., "Controlled interface profile in Sm-CoFe exchange-spring magnets," *Applied Physics Letters*, vol. 91, no. 7, Article ID 072509, 2007.

[22] F. Casoli, F. Albertini, L. Nasi et al., "Strong coercivity reduction in perpendicular FePtFe bilayers due to hard/soft coupling," *Applied Physics Letters*, vol. 92, no. 14, Article ID 142506, 2008.

[23] A. Sun, F. Yuan, J. Hsu, Y. H. Lin, and P. C. Kuo, "Magnetic reversal behaviors of perpendicular exchange-coupled Fe/FePt bilayer films," *IEEE Transactions on Magnetics*, vol. 45, no. 6, pp. 2709–2715, 2009.

[24] J. Zhang, Y. X. Li, F. Wang, B. G. Shen, and J. R. Sun, "Coercivity mechanism of nanocomposite Sm-Co/Fe multilayer films," *Journal of Applied Physics*, vol. 107, no. 4, Article ID 043911, 4 pages, 2010.

[25] C. Rong, Y. Zhang, N. Poudyal, X. Xiong, M. J. Kramer, and J. P. Liu, "Fabrication of bulk nanocomposite magnets via severe plastic deformation and warm compaction," *Applied Physics Letters*, vol. 96, no. 10, Article ID 102513, 2010.

[26] D. Kim and J. Hong, "Rare earth free exchange spring magnet FeCo/FePt(001): giant magnetic anisotropy and energy product," *Surface Science*, vol. 606, p. 1960, 2012.

[27] P. Saravanan, J. H. Hsu, A. Gayen et al., "Effect of Fe layer thickness and Fe/Co intermixing on the magnetic properties of Sm–Co/Fe bilayer exchange-spring magnets," *Journal of Physics D*, vol. 46, no. 15, Article ID 155002, 2013.

[28] R. Skomski and J. M. D. Coey, "Giant energy product in nanostructured two-phase magnets," *Physical Review B*, vol. 48, no. 21, pp. 15812–15816, 1993.

[29] R. F. Sabiryanov and S. S. Jaswal, "Electronic structure and magnetic properties of hard/soft multilayers," *Journal of Magnetism and Magnetic Materials*, vol. 177–181, no. 2, pp. 989–990, 1998.

[30] A. Perumal, Y. K. Takahashi, T. O. Seki, and K. Hono, "Particulate structure of L 10 ordered ultrathin FePt films for perpendicular recording," *Applied Physics Letters*, vol. 92, no. 13, Article ID 132508, 2008.

[31] L. Zhang, Y. K. Takahashi, A. Perumal, and K. Hono, "L10-ordered high coercivity (FePt)AgC granular thin films for perpendicular recording," *Journal of Magnetism and Magnetic Materials*, vol. 322, no. 18, pp. 2658–2664, 2010.

[32] T. Shima, K. Takanashi, Y. K. Takahashi, and K. Hono, "Preparation and magnetic properties of highly coercive FePt films," *Applied Physics Letters*, vol. 81, no. 6, pp. 1050–1052, 2002.

[33] J. Jiang, N. Tezuka, and K. Inomata, "Indirect exchange spring between FePt and Fe with a Ru interlayer," *Journal of Magnetism and Magnetic Materials*, vol. 302, no. 1, pp. 40–46, 2006.

[34] S. Okamoto, N. Kikuchi, O. Kitakami, T. Miyazaki, Y. Shimada, and K. Fukamichi, "Chemical-order-dependent magnetic anisotropy and exchange stiffness constant of FePt (001) epitaxial films," *Physical Review B*, vol. 66, no. 2, Article ID 024413, pp. 244131–244139, 2002.

[35] A. Perumal, L. Zhang, Y. K. Takahashi, and K. Hono, "FePtAg-C nanogranular films fabricated on a heat resistant glass substrate for perpendicular magnetic recording," *Journal of Applied Physics*, vol. 108, no. 8, Article ID 083907, 2010.

[36] S. Okamoto, O. Kitakami, N. Kikuchi, T. Miyazaki, Y. Shimada, and Y. K. Takahashi, "Size dependences of magnetic properties and switching behavior in FePt L10 nanoparticles," *Physical Review B*, vol. 67, no. 9, Article ID 094422, pp. 944221–944227, 2003.

[37] Y. K. Takahashi, T. Ohkubo, M. Ohnuma, and K. Mono, "Size effect on the ordering of FePt granular films," *Journal of Applied Physics*, vol. 93, no. 10, pp. 7166–7168, 2003.

[38] C. Rong, D. Li, V. Nandwana et al., "Size-dependent chemical and magnetic ordering in L10-FePt nanoparticles," *Advanced Materials*, vol. 18, no. 22, pp. 2984–2988, 2006.

[39] C. P. Luo and D. J. Sellmyer, "Structural and magnetic properties of FePt:SiO$_2$ granular thin films," *Applied Physics Letters*, vol. 75, no. 20, pp. 3162–3164, 1999.

[40] C. Brombacher, *Rapid thermal annealing of FePt and FePt/Cu thin films [Ph.D. thesis]*, Chemnitz University of Technology, Chemnitz, Germany, 2011.

[41] J. D. Livingston, "A review of coercivity mechanisms (invited)," *Journal of Applied Physics*, vol. 52, no. 3, pp. 2544–2548, 1981.

[42] H. S. Ko, A. Perumal, and S. Shin, "Fine control of L 10 ordering and grain growth kinetics by C doping in FePt films," *Applied Physics Letters*, vol. 82, no. 14, pp. 2311–2313, 2003.

[43] N. Li and B. M. Lairson, "Magnetic recording on FePt and FePtB intermetallic compound media," *IEEE Transactions on Magnetics*, vol. 35, no. 2, pp. 1077–1082, 1999.

[44] M. P. Sharroack and J. T. McKinney, "Kinetic effects in coercivity measurementsIEEE Transactions on Magnetics," vol. 17, p. 3020, 1981.

[45] R. H. Victora, "Predicted time dependence of the switching field for magnetic materials," *Physical Review Letters*, vol. 63, no. 4, pp. 457–460, 1989.

[46] M. El-Hilo, "Time-dependent coercivity in participate recording media," *Journal of Magnetism and Magnetic Materials*, vol. 272-276, no. III, pp. 1700–1702, 2004.

[47] K. R. Coffey, J. Thiele, and T. Thomson, "Temperature dependence of the magnetization reversal of thin-film longitudinal magnetic recording media," *IEEE Transactions on Magnetics*, vol. 40, no. 4, pp. 2440–2442, 2004.

[48] C. W. Su, J. S. Tsay, and Y. D. Yao, "Finding stabilized coercivity in a study of thickness and temperature dependent Co/Ag/Ge(001) ultrathin films," *Thin Solid Films*, vol. 516, no. 6, pp. 1164–1170, 2008.

[49] J. Zhou, R. Skomski, X. Li, W. Tang, G. C. Hadjipanayis, and D. J. Sellmyer, "Permanent-magnet properties of thermally processed FePt and FePt-Fe multilayer films," *IEEE Transactions on Magnetics*, vol. 38, no. 5 I, pp. 2802–2804, 2002.

[50] F. Casoli, F. Albertini, L. Nasi et al., "Role of interface morphology in the exchange-spring behavior of FePt/Fe perpendicular bilayers," *Acta Materialia*, vol. 58, no. 10, pp. 3594–3601, 2010.

[51] A. J. A. De Oliveira, W. A. Ortiz, D. H. Mosca, N. Mattoso, I. Mazzaro, and W. H. Schreiner, "Magnetic irreversibility in Fe/Cu multilayers," *Journal of Physics Condensed Matter*, vol. 11, no. 1, pp. 47–57, 1999.

[52] Y. Rheem, H. Saito, and S. Ishio, "Fabrication of FePt/FeCo/FePt exchange-spring trilayer with very thin FeCo layer for high-resolution MFM tips," *IEEE Transactions on Magnetics*, vol. 41, no. 10, pp. 3793–3795, 2005.

[53] N. B. Herndon, S. H. Oh, J. T. Abiade et al., "Effect of spacer layer thickness on magnetic interactions in self-assembled single domain iron nanoparticles," *Journal of Applied Physics*, vol. 103, no. 7, Article ID 07D515, 2008.

[54] F. Almeida, *Exchange Springs and Exchange bias studied with nuclear methods [Ph.D. thesis]*, Katholieke Universiteit Leuven, Flanders, Belgium, 2011.

*Research Article*

# Synthesis and Magnetic Properties of Ni and Carbon Coated Ni by Levitational Gas Condensation (LGC)

## Young Rang Uhm[1] and Chang Kyu Rhee[2]

[1] *Radioisotope Research Division, Korea Atomic Energy Research Institute, 989 Daedukdaero, Daejeon 305-353, Republic of Korea*
[2] *Nuclear Materials Development Research Division, Korea Atomic Energy Research Institute, 989 Daedukdaero, Daejeon 305-353, Republic of Korea*

Correspondence should be addressed to Young Rang Uhm; uyrang@kaeri.re.kr

The nickel (Ni), and carbon coated nickel (Ni@C) nanoparticles were synthesized by levitaional gas condensation (LGC) methods using a micron powder feeding (MPF) system. Both metal and carbon coated metal nano powders include a magnetic ordered phase. The synthesis by LGC yields spherical particles with a large coercivity. The abnormal initial magnetization curve for Ni indicates a non-collinear magnetic structure between the core and surface layer of the particles. The carbon coated particles had a core structure diameter at and below 10 nm and were covered by 2-3 nm thin carbon layers. The hysteresis loop of the as-prepared Ni@Cs materials with unsaturated magnetization shows a superparamagnetic state at room temperature.

## 1. Introduction

Nanoparticles have achieved significant attention owing to the novel electro-optic, magnetic, and catalytic properties that arise from the quantum size effect and large specific surface areas that are characteristic of nanosized species [1, 2]. Magnetic nanoparticles have attracted much of the attention these days, because of their potential technological applications in nanofluids for biomedical application, thermal conductive fluids, various catalysts, and so forth [1–3]. However, the preparation of nanofluids using pure metal nanoparticles is very hard, because nanoparticles are inherently vulnerable to oxidation, dissolution and agglomeration. In particular, agglomeration of the particles in a solvent is a serious problem when preparing nanofluids. To overcome these problems, a protective shell has been recommended to improve the chemical stability of metal nanoparticles and the dispersion stability in the solvent [4–6]. It is also worth noting that these materials are not prone to agglomeration owing to the fact that the addition of a carbon coating layer reduces the magnetic interaction. In addition, the surface diffusion processes allow the preservation of the chemical and structural properties of the nanopowder for a long time in many chemically aggressive surroundings [7]. In particular, a graphitic carbon shell is regarded as an ideal coating as it is light and shows high stability in both chemical and physical environments [8, 9]. The stable dispersion of nanoparticles in both aqueous and nonaqueous media has important applications in cosmetics, chemicals, pharmaceuticals, microelectronics, paints, and pigments [10, 11]. Nanoparticle dispersion depends on many factors, such as the solvent, pH, added ion, dispersant, and particle size. In particular, the preparation of a stable suspension of metallic nanoparticles is difficult owing to the high density and agglomeration of particles. Carbon-encapsulated metal nanoparticles are expected to have a large advantage for preventing the coalescence of the particles in the fluid. In this study, we introduce Ni and carbon-coated Ni (Ni@C) nanoparticles synthesized using LGC [11]. We also report on the dispersion stability in various solutions, such as water, ethanol, and ethylene glycol.

## 2. Experiment

High purity Ni and Ni@C nanopowders were synthesized by a LGC method using a micron powder feeding (MPF) system

FIGURE 1: The shape of inductor and the concept of system for LGC.



FIGURE 2: X-ray diffraction patterns for the Ni and Ni@C nanoparticles.

The as-prepared sample was characterized by X-ray diffraction (XRD), transmission electron microscopy (TEM), and a vibrating sample magnetometer (VSM). The suspensions of Ni@C nanoparticles were prepared as follows: we prepared solvents of ethanol and polyethylene glycol (MW 20000) in 100 mL; we then added 0.01 wt.% of nanoparticles and ultrasonicated the suspension for 20 min. To characterize the dispersion stability, we used Turbiscan Lab. and took measurements every 1 hour for 3 days.

## 3. Results and Discussion

The Ni and Ni@Cs materials were obtained using the LGC. A liquid droplet which is levitated by the magnetic force acted against the gravitational force from the coupled induction coils. The induction heat coil and the concept of LGC system are displayed at Figure 1. The inductor is heated up to 2000°C and the metallic atoms evaporated from the overheated surface of the liquid droplet and condensed by cold inert gas and then collected into the filter [11]. The mechanism for the formation of Ni nanoparticles is evaporation and condensation. At the same time, the molecular $CH_4$ introduced into the chamber is converted into atomic C and H with high activity under high temperature. The highly active C atoms can react with Ni atoms. The H atoms converted into $H_2$ molecules. The newly created $H_2$ gas is vented out of the reaction chamber by continuous vacuum operation. The mechanism for the formation of graphitic carbon shell is reaction between active C atom and metal without chemical compounds of carbides [12].

Nanoparticles Ni and Ni@C synthesized by LGC using a micron powder feeding system were confirmed by an XRD pattern, as shown in Figure 2. The XRD results for Ni shows lattice parameters and the position of the main peaks of the Ni powders. The small amount of NiO phase was found in the XRD patterns and in the TEM images, which results from a passivation on the powder surface. The microstructure and phase composition of Ni powders were studied using TEM. A particle consists of a single domain. The powders with

[11]. The apparatus consists of a high-frequency induction generator of 6 kW, a levitation and evaporation chamber, and a methane ($CH_4$) concentration control unit. Ni powder (99.9 at.%, ~500 $\mu$m) was used as a starting material for the synthesis of carbon encapsulated Ni nanoparticles. The Ni powders were mixed into the micron powder feeding system consisting of a rotation part for supplying the Ni micron powders to the melted droplet and a vibrating part for protecting the aggregation of the powder. The Ni micron powders were fed into a powder feeding system with the feeding rate of 80 mg/min. A Ni ingot of 87 mg, as a seed material for levitation and evaporation reactions, was melted by electric induction heat. The gas pressure for the Ar in chamber was 100 torr. The ratio of $CH_4$ was 10% of the mixture gas, when the carbon coated Ni was prepared.

(a) (b)

FIGURE 3: TEM images of (a) the Ni and (b) the Ni@C nanoparticles.

single domains are synthesized by a special gas phase method, though the average particle size is over 100 nm [12]. The thin oxide layer on powders forms a continuous coating with a thickness of 2-3 nm. Fig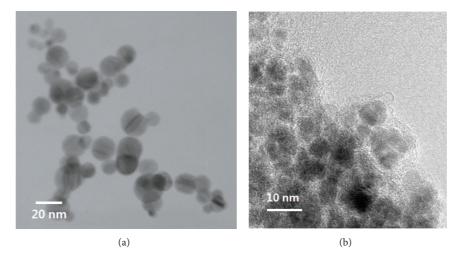ure 2(b) shows the XRD patterns of the as-obtained Ni@C. All the main reflection peaks can be indexed to Ni. The strong nature of the peaks indicates that the final products are well crystallized and have high purity. The case of Ni@Cs materials is due to the (0 0 2) diffraction of graphite layers. However, the intensity for the (0 0 2) peak of the sample is broad and low. The shell layer in the Ni@Cs samples is made of amorphous carbon. For the Ni@Cs material, the diffraction peaks at 44.4°, 51.8°, and 76.3° are due to the (1 1 1), (2 0 0), and (2 2 0) planes of fcc-Ni, respectively.

The carbon shell structure of the Ni@Cs samples, which is further confirmed by the TEM results, is discussed in Figure 3. Nanoparticles Ni and Ni@C synthesized by LGC show a spherical shape as shown in Figure 3. The TEM image shows that nanocrystalline Ni powders consist of particles with the size ranges from 15 nm to 40 nm. The magnetic properties of nanopowders were affected by the size effect resulting from the anisotropy field and magnetic domain effect on the particles [13]. The morphologies of the carbon-coated Ni nanocrystallites were characterized by TEM as shown in Figure 3(b). The results indicated that all of the as-made materials were composed of only nanocapsules with a uniform particle size at and below 10 nm. At the previous study, nanocapsules consisted of outer multishells of carbon were observed using a high resolution TEM [13].

The powders synthesized by LGC method show low saturation magnetization for Ni. This results from a spin-canting effect and oxide phase on the surface [11]. The magnetic properties would be weak due to antiferromagnetic NiO phase on the powder surface. The saturation magnetization is Ms = 42 emu/g. In Figure 4(a), the hysteresis loop of Ni in the low fields is shown. The slightly shifted hysteresis loop for the Ni sample can be explained by exchange bias between the ferromagnetic core of Ni and antiferromagnetic surface of NiO [12, 14]. The initial magnetization curve is not explained by the size effect. At previous studies, the

virgin magnetization curve slightly spills over the limited hysteresis loop at 655 Oe [13]. We assume that this effect enhances when the size of the particles is reduced, at previous study. With a decreasing particle size, the defects and the different magnetic structure on the surface of the particles are increased [13]. The nature of this irreversibility in high magnetic fields allows for the description of a physical model [12, 13]. This irreversibility can be explained by a spin-glass or spin-canting behavior. The VSM magnetic measurement results for the synthesized Ni@Cs materials are shown in Figure 4(b). The hysteresis loop of the as-made M@Cs materials in the magnetic field up to 1 T reveals the intrinsic magnetic behaviour, indicated by the magnetization (M), the remanent magnetization (Mr) and the coercive force (Hc) for the M@Cs samples (Figure 4(b)). The saturation magnetization demonstrated that the carbon-coated Ni nanocrystallites exhibited a superparamagnetic behaviour at room temperature. The magnetization was not saturated in the applied field up to 2 T as shown in Figure 4(c). The size of the nanoparticles may affect the value of the coercive field due to the size influence of the magnetization of the nanoparticles [13, 14]. In the case of very small nanoparticles one can observe superparamagnetic behaviour, related to the demagnetization effect arising from the additional energy of the magnetic fields outside the graphitic carbon encapsulation. The coercive force (Hc) and magnetization (M) were 76.6 Oe and 19.6 (emu/g), respectively. The ratio of remanence to the saturation magnetization (Mr/M) of the Ni@Cs samples is 0.04. The low magnetization comparing with the Ni nanoparticles without carbon-shell results in the coexistence of nonmagnetic carbon and a large surface spin percentage with disordered magnetization orientation for the nanoparticles [14, 15]. The magnetization and coercive force for Ni and Ni@C nanaoparticles were influenced by both the particle size and the surface status on the particle.

To evaluate the dispersion stability and agglomeration phenomena of the carbon encapsulated Ni nanoparticles in solvents of ethanol and polyethylene glycol (PEG), the time-dependent sedimentation behavior was investigated by the

(a)



(b)



(c)
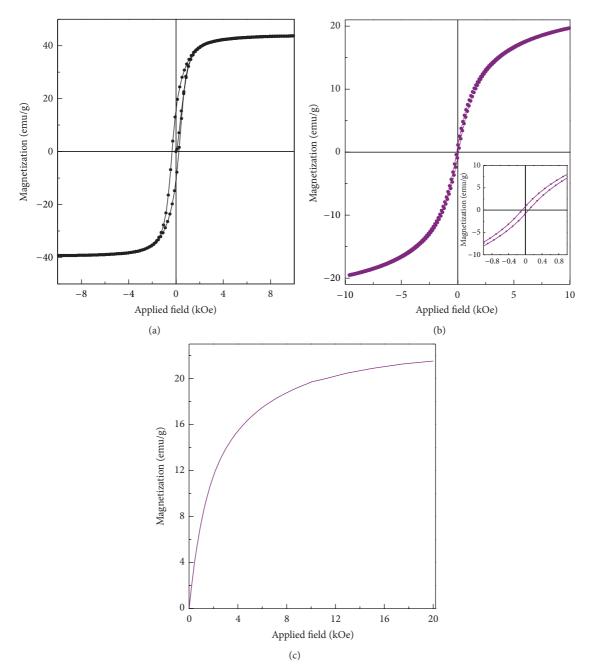
FIGURE 4: The hysteresis loops of (a) Ni and (b) Ni@C nanoparticles at room temperature. (Magnification of hysteresis loop for Ni@C is represented.) (c) Initial magnetization curve for Ni@C nanoparticles at room temperature.

transmission profile measurements using a Turbiscan Lab. The transmission profiles were taken every 1 hr for 72 hrs when the suspending medium was ethyl alcohol. It was found that the transmission intensity decreased at the sample top owing to a clarification and increased at the sample bottom from sedimentation, as shown in Figure 5 (a2) and (b2). A very stable Ni@C dispersion was observed without showing any clarification or sedimentation, as shown in Figure 5 (a1) and (b1). On the contrary, a progressive fall of the signal, which was observed as a function of time in the middle region of the Ni nanoparticles with an average particle size of 20 nm,

can be explained by flocculation-induced particle growth as shown in Figure 5 (a2) and (b2).

## 4. Conclusions

Nanopaticles Ni and carbon coated Ni were prepared by LGC. A simple approach to fabricate a carbon-shell layer is to use methane ($CH_4$) gas as the carbon source. The particle size of carbon-coated Ni with diameters in the range of up to 10 m was smaller than those of Ni nanoparticles

(a1)



(b1)



(a2)



(b2)
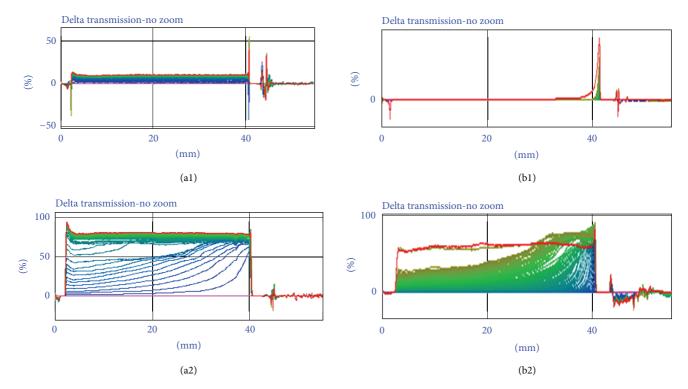
FIGURE 5: Transmission profiles for (a1) Ni@C and (a2) Ni nanopowders in ethanol and (b1) Ni@C and (b2) Ni nanoparticles in polyethylene glycol (PEG) at 25°C.

without a carbon shell. The dispersion stability kinetics of the PEG showed good dispersion. However, the sedimentation and flocculation behavior were observed in Ni nanoparticles without a carbon shell. The fully coated carbon shell layers of the Ni nanoparticles positively affected the stable dispersion in the fluid. Both the particle size and surface layer influence the magnetic hysteresis behavior of nanopowders.

## Acknowledgment

## References

[1] R. S. Ruoff, D. C. Lorents, B. Chan, R. Malhotra, and S. Subramoney, "Single crystal metals encapsulated in carbon nanoparticles," *Science*, vol. 259, no. 5093, pp. 346–348, 1993.

[2] J. H. J. Scott and S. A. Majetich, "Morphology, structure, and growth of nanoparticles produced in a carbon arc," *Physical Review B*, vol. 52, no. 17, pp. 12564–12571, 1995.

[3] Y. Kinemuchi, K. Ishizaka, H. Suematsu, W. Jiang, and K. Yatsui, "Magnetic properties of nanosize $NiFe_2O_4$ particles synthesized by pulsed wire discharge," *Thin Solid Films*, vol. 407, no. 1-2, pp. 109–113, 2002.

[4] J. Fang, N. Shama, L. Duc Tung et al., "Ultrafine $NiFe_2O_4$ powder fabricated from reverse microemulsion process," *Journal of Applied Physics*, vol. 93, no. 10, pp. 7483–7485, 2003.

[5] U. Jeong, X. Teng, Y. Wang, H. Yang, and Y. Xia, "Superparamagnetic colloids: controlled synthesis and niche applications," *Advanced Materials*, vol. 19, no. 1, pp. 33–60, 2007.

[6] S. Subramoney, "Novel nanocarbons—structure, properties, and potential applications," *Advanced Materials*, vol. 10, no. 15, pp. 1157–1171, 1998.

[7] B. H. Liu, J. Ding, Z. Y. Zhong, Z. L. Dong, T. White, and J. Y. Lin, "Large-scale preparation of carbon-encapsulated cobalt nanoparticles by the catalytic method," *Chemical Physics Letters*, vol. 358, no. 1-2, pp. 96–102, 2002.

[8] H. Caoa, G. Huangb, S. Xuana, Q. Wu, F. Gua, and C. Li, "Synthesis and characterization of carbon-coated iron core/shell nanostructures," *Journal of Alloys and Compound*, vol. 448, pp. 272–276, 2008.

[9] T. Hayashi, S. Hirono, M. Tomita, and S. Umemura, "Magnetic thin films of cobalt nanocrystals encapsulated in graphite-like carbon," *Nature*, vol. 381, no. 6585, pp. 772–774, 1996.

[10] S. H. Woo, M. K. Lee, and C. K. Rhee, "Sedimentation properties of $TiO_2$ nanaoparticles in organic solvents," *Solid State Phenomina*, vol. 119, pp. 267–270, 2007.

[11] B. S. Han, C. K. Rhee, M. K. Lee, and Y. R. Uhm, "Synthesis of nano crystalline Ni and Fe by levitational gas condensation method," *IEEE Transactions on Magnetics*, vol. 42, no. 11, pp. 3779–3781, 2006.

[12] Y. R. Uhm, J. H. Park, W. W. Kim, C.-H. Cho, and C. K. Rhee, "Magnetic properties of nano-size Ni synthesized by the pulsed wire evaporation (PWE) method," *Materials Science and Engineering B*, vol. 106, no. 3, pp. 224–227, 2004.

[13] A. Y. Yermakov, M. A. Uimin, A. A. Mysik et al., "Magnetism and structure of nanoparticles and mesoscopic systems," *Materials Science Forum*, vol. 386–388, pp. 455–464, 2002.

[14] B. D. Cullity, *Introduction To Magnetic Materials*, Addison-Wesley, Reading, Mass, USA, 1972.

[15] C. Yu and J. S. Qiu, "Preparation and magnetic behavior of carbon-encapsulated cobalt and nickel nanoparticles from starch," *Chemical Engineering Research and Design*, vol. 86, no. 8, pp. 904–908, 2008.

*Review Article*

# Recent Advances in Understanding Magnetic Nanoparticles in AC Magnetic Fields and Optimal Design for Targeted Hyperthermia

## Hiroaki Mamiya

*National Institute for Materials Science, Tsukuba 305-0047, Japan*

Correspondence should be addressed to Hiroaki Mamiya; mamiya.hiroaki@nims.go.jp

Targeted hyperthermia treatment using magnetic nanoparticles is a promising cancer therapy that enables selective heating of hidden microcancer tissues. In this review, I outline the present status of chemical synthesis of such magnetic nanoparticles. Then, the latest progress in understanding their heat dissipation mechanisms under large magnetic fields is overviewed. This review covers the recently predicted novel phenomena: magnetic hysteresis loops of superparamagnetic states and steady orientations of easy axes at the directions parallel, perpendicular, or oblique to the AC magnetic field. Finally, this review ends with future prospects from the viewpoint of optimal design for efficacy with a low side-effect profile.

## 1. Introduction

Hippocrates said, "those diseases which drugs cannot cure, the knife cures; those which the knife cannot cure, fire cures; those which fire does not cure must be considered incurable." In one respect, medicine has not changed over time; even today, several treatments are used in combination to treat illnesses that have no established effective treatment protocol, the most prominent example being cancer. The current standard treatments for cancer include surgery, chemotherapy, and radiotherapy. Beyond these treatments, much research is being undertaken to create several new treatment options such as immunotherapy, and the modern equivalent of Hippocrates' "fire": thermotherapy. Thermotherapy is a treatment method that exploits the lowered heat resistance of cancerous tissues compared with that of normal tissues. Cancerous tissues undergo cell death even at temperatures within the range of 42 to 43°C, thus rendering thermotherapy as a promising option to reduce the disease burden in a patient [1].

To reduce damage to normal tissues using standard treatments, endo-/laparoscopic surgical techniques have been developed as a modern equivalent of Hippocrates' "knife." For chemotherapy, much effort has focused on drug delivery to selectively transport anticancer agents to tumor tissues using antigen-antibody reactions. Such drug delivery systems are also used to concentrate boron compounds in tumor tissues. In the treatment known as boron neutron capture therapy, the patient is radiated with epithermal neutrons, which selectively induce $\alpha$-decay of boron nuclei concentrated inside hidden tumors, thus specifically destroying cancer cells. Along these lines, could thermotherapy also utilize drug delivery technology to specifically deliver thermal seeds to cancer cells at unknown locations? For example, if it were possible to develop miniature induction-heating cooking pans and selectively send these to hidden tumors, then would this result in selective heating of the tumor tissues in a human body on an induction-heating cooker? In contrast to a microwave oven, we know that placing one's hand over the induction-heating cooker will not immediately result in a burn. (Usually, we cannot confirm this feature using the commercial IH cooker, because it automatically stops working when we take off a metal pan from it.) This experience shows that a radio-waveband AC magnetic field generated in the cooker can easily penetrate deep into tissues where a tumor may be embedded. Therefore, we believe that the simple idea mentioned here, targeted hyperthermia

using magnetic nanoparticles, has the potential to selectively destroy cancer cells hidden deep in the body [2–8].

Of course, there are many questions about this concept that need to be addressed. Is it safe to put magnetic nanoparticles in the body? Can magnetic nanoparticles really be concentrated in hidden tumor tissues? Can magnetic nanoparticles be heated within the body? To answer these questions, DeNardo et al. injected iron oxide nanoparticles conjugated with monoclonal antibodies into mouse tails and found that they accumulated at a concentration $c$ of approximately $0.3 \, \text{kg/m}^3$ ($0.3 \, \text{mg/cm}^3$) in tumors [9]. (The side effects of iron oxide nanoparticles as an MRI contrast agent had been previously studied and approved for intravenous injection.) Wust et al. showed that injecting high concentrations ($c \sim 10 \, \text{kg/m}^3$) of magnetic nanoparticles directly into tumors at known locations and irradiating them with an AC magnetic field caused the temperature of the tumors to increase to $43°\text{C}$ [10]. Therefore, it is known that iron oxide nanoparticles are safe, can be selectively accumulated in hidden tumors to some degree, and can be adequately heated when existing at high concentrations. Nevertheless, problems with targeted hyperthermia using magnetic nanoparticles are still evident. Does the density of magnetic nanoparticles delivered to tumors increase as it does when they are directly injected into tumors? If not, is it possible to compensate for a lower density of magnetic nanoparticles by maximizing their heat dissipation? The first problem is primarily a biochemical one, so materials researchers have primarily focused on improving the heating performance of magnetic nanoparticles [11–30]. Consequent advances in chemical synthesis technology have resulted in the fabrication of magnetic nanoparticles of engineered size, shape, and structure. With respect to physical heating mechanisms, the nature of the nonlinear response and nonequilibrium dissipation in AC magnetic fields of magnetic nanoparticles, which are in contrast to the properties of cooking pans, have been uncovered. This review addresses this progress as follows. In Section 2, conventional models that are the basis of the traditional design of hyperthermia treatments are introduced. In Section 3, advances in the synthesis of magnetic nanoparticles are described and limitations in the conventional models when the monodisperse nanoparticles are used in actual thermotherapy are considered. In Section 4, recent advances in the knowledge of heating mechanisms provided by numerical simulations are explained. Finally, we summarize the optimal design of magnetic nanoparticles for hyperthermia treatment and discuss their potential as an effective and safe version of Hippocrates' "fire" in Section 5.

## 2. Conventional Models for Magnetic Response to AC Magnetic Fields [31–34]

The main advantage of hyperthermia treatment using magnetic nanoparticles is that the nanoparticles can reach the cancer tissue directly by travelling through the submicrometer spaces between blood cell walls. Therefore, for practical use, the nanoparticles should not form long chains or large clusters. Even though the many-body effects caused

by dipole-dipole coupling $J_{\text{dd}}$ are not fully understood [35–38], it is known that a dispersion becomes unstable if $J_{\text{dd}}$ between the closest nanoparticles is more than five times the thermal energy [35, 38]. Under these conditions, the minimum allowable distance between iron nanoparticles with diameter $d$ of 12 nm is roughly 27 nm, and that between ferrite nanoparticles with $d$ of 25 nm is almost 40 nm. In contrast, small-angle neutron scattering experiments have indicated that the thickness of an absorbed layer is normally several nanometers [39]. Therefore, the upper limit of $d$ is estimated to be roughly 12 nm for iron and 25 nm for ferrite. These values would be references for considering the criteria for easy delivery of the nanoparticles, although agglomeration, aggregation, or flocculation may occur depending on the surface charge of biofunctionalized nanoparticle or on the interaction between tumor-targeting ligands. Note that these values are smaller than the critical diameters for the transition into a single-domain configuration and for the coherent reversal of all spins [40]. Therefore, it has been considered that a magnetic nanoparticle used in hyperthermia treatment has only one magnetic moment, $\boldsymbol{\mu} = \mathbf{M}_s V$, where $\mathbf{M}_s$ is the spontaneous magnetization and $V = \pi/6 \cdot d^3$ is the volume of the magnetic core of the nanoparticle. Such magnetic nanoparticles have been conventionally classified as "ferromagnetic" or "superparamagnetic," depending on whether the direction of $\boldsymbol{\mu}$ thermally fluctuates or not.

Firstly, a ferromagnetic nanoparticle with uniaxial magnetic anisotropy, anisotropy constant $K$, is considered, where $V$ is large enough that its magnetic anisotropy barrier with a height of $KV$ blocks the thermal fluctuations; accordingly, the remanent state appears to be permanent [41]. If a magnetic field $\mathbf{H}$ is applied in the direction antiparallel to $\boldsymbol{\mu}$, the state becomes metastable, as depicted in Figure 1(a). Then, $\boldsymbol{\mu}$ reverses when the barrier disappears at the anisotropy field $H_K = 2K/(\mu_0 M_s)$; consequently, the Zeeman energy falls from $\mu_0 \mu H_K$ to $-\mu_0 \mu H_K$ and the energy corresponding to the difference dissipates, where $\mu_0$ is permeability of vacuum. In this case, the work done in one cycle of the AC magnetic field $H_{\text{ac}} \sin(2\pi f \cdot t)$ is 0 for $H_{\text{ac}} < H_K$ and $4\mu_0 \mu H_K$ for $H_{\text{ac}} > H_K$. This kind of heat dissipation has been termed "hysteresis loss." Briefly, the heat dissipation from nanoparticles with unit weight during unit time, also called specific loss power $P_H$, abruptly increases from zero to $4\mu_0 \mu H_K \cdot f \cdot w^{-1}$ (= $4\mu_0 M_s H_K \cdot f \cdot \rho^{-1}$) when $H_{\text{ac}}$ becomes higher than $H_K$, where $w$ and $\rho^{-1}$ are the weight and density of the magnetic core of the nanoparticles, respectively. Then, $P_H$ flattens out even if $H_{\text{ac}}$ is strengthened further. According to this argument, the guiding principle for maximizing $P_H$ of ferromagnetic nanoparticles is that $H_{\text{ac}}$ is adjusted to $H_K$ and the number of cycles $f$ is maximized.

Next we move to smaller superparamagnetic nanoparticles with thermally fluctuating reversal of $\boldsymbol{\mu}$ [42]. The reversal probability in a zero magnetic field is expressed as

$$\tau_N^{-1} = f_0 \cdot \exp\left(\frac{-KV}{k_B T}\right), \tag{1}$$

where $\tau_N$ is the Néel relaxation time, $f_0$ is the attempt frequency of $10^9 \, \text{s}^{-1}$, $k_B$ is the Boltzmann constant, and $T$ is
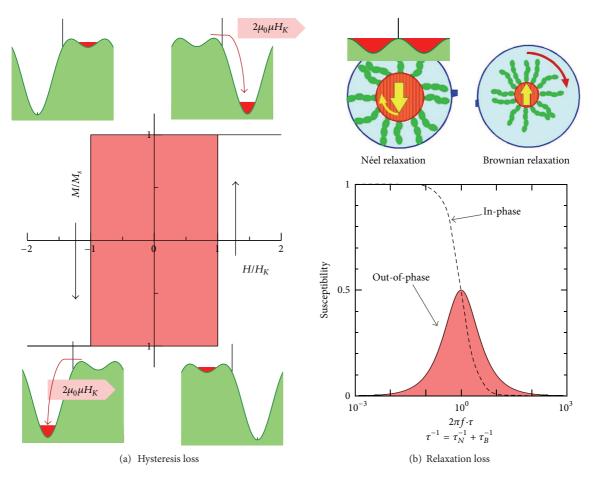
(a) Hysteresis loss

(b) Relaxation loss

FIGURE 1: Schematic diagrams of conventional models for magnetic loss. (a) Hysteresis loss equivalent to the area of $M$-$H$ loop, and the potential energy in magnetic fields. (b) Relaxation loss given by the out-of-phase component of AC susceptibility. As illustrated in the sketches, in Néel relaxation, the magnetic moment shown by the yellow arrow reverses (the particle does not rotate), while in Brownian relaxation, the magnetic core (the red sphere) rotates with absorbed molecules (the green chains) as a whole (the magnetic moment does not reverse).

the temperature. We must also consider Brownian rotation of the nanoparticles if they are dispersed in a liquid phase. In this case, the characteristic time of the rotation, Brownian relaxation time, in a zero magnetic field is given by

$$\tau_B = \frac{3\eta V_H}{(k_B T)}, \qquad (2)$$

where $\eta$ is the viscosity of the liquid phase and $V_H$ is the hydrodynamic volume of the nanoparticles including surface modification layers. If reversal and rotation occur in parallel, the characteristic time of relaxation $\tau$ could be expressed as the following equation:

$$\tau^{-1} = \tau_N^{-1} + \tau_B^{-1}. \qquad (3)$$

For very small superparamagnetic nanoparticles, $\tau$ is determined only by $\tau_N$ because $\tau_N^{-1}$ increases exponentially with decreasing $V$, while the increase of $\tau_B^{-1}$ is inversely proportional to $V_H$.

   If a linear response of the thermodynamic equilibrium state of such nanoparticles is assumed for small $H_{ac}$,

the average out-of-phase component of AC susceptibility, $\chi''$, contributed from each nanoparticle is given by

$$\chi'' = \frac{\mu_0 \mu^2}{(3k_B T)} \cdot \frac{2\pi f \cdot \tau}{\left[1 + \left(2\pi f \cdot \tau\right)^2\right]}. \qquad (4)$$

Consequently, "relaxation loss" occurs and its heat dissipation $P_H$ is expressed as

$$
\begin{aligned}
P_H &= \pi \mu_0 \chi'' \cdot H_{ac}^2 \cdot f \cdot w^{-1} \\
&= \frac{1}{2} \frac{\left[\mu_0^2 M_s^2 V / (3k_B T \tau \rho)\right] \cdot H_{ac}^2 \cdot \left(2\pi f \cdot \tau\right)^2}{\left[1 + \left(2\pi f \cdot \tau\right)^2\right]}.
\end{aligned}
\qquad (5)
$$

Equation (5) indicates that $P_H$ increases in proportion to $f^2$ in the low frequency range, $2\pi f \ll \tau$, whereas it flattens out at $1/2[\mu_0^2 M_s^2 V/(3k_B T \tau \rho)] \cdot H_{ac}^2$ even if $f$ is increased further in the high frequency range, $2\pi f \gg \tau$. According to this argument, the guiding principle for maximizing $P_H$ of superparamagnetic nanoparticles is that $f$ is adjusted to $\tau^{-1}$ and $H_{ac}$ is maximized.

# 3. Progress in Synthesis of Magnetic Nanoparticle and Their Use in Thermotherapy

*3.1. Size-, Shape- and Composite-Controlled Synthesis of Magnetic Nanoparticles.* As discussed above, to improve hysteresis loss, ferromagnetic nanoparticles with an anisotropy field ($H_K = 2K/(\mu_0 M_s)$) matching the amplitude $H_{ac}$ of the AC magnetic field generated in the oscillator of realistic medical equipment need to be synthesized. In contrast, increasing relaxation loss involves the synthesis of superparamagnetic nanoparticles that have $\tau_N$ matching $f$ of the AC magnetic field. For these reasons, a large number of studies have focused on controlling the size, shape, or composite structure of nanoparticles to optimize $H_K$ and $\tau_N$.

The history of colloids (magnetic fluids) stably dispersing magnetic nanoparticles in solution goes back to the 1960s, when magnetic suspensions were prepared by pulverizing bulk iron oxide and used for fuel delivery in a weightless environment [43], such as those involving NASA expeditions. Elsewhere, Sato of Tohoku University created magnetic fluids from minute iron oxide particles using chemical methods [44]. There have also been several major subsequent advances in magnetic fluid development, such as the monodisperse iron nitride-based magnetic fluids developed by Nakatani et al. [45]; however, because the industrial applications of magnetic fluids at that time did not require precise control of size, shape, or structure, more extensive research was not conducted in this field. However, in 2000, Sun et al. from IBM described an ordered self-assembled film of monodisperse iron-platinum nanoparticles that could serve as an ultrahigh-tech magnetic recording medium [46]. Since then, researchers have focused on developing methods to synthesize well-controlled nanoparticles, which have been reviewed extensively [47, 48]. Next, we briefly summarize these methods.

Generally, formation of nanoparticles starts with nucleation in a supersaturated melt, solution, or vapor. Particle growth continues until the concentration of solute atoms falls below the saturation solubility. If nucleation and growth proceed in parallel, nanoparticles formed initially have already grown when the last nanoparticle is formed, thus resulting in nanoparticles of variable size. Furthermore, processes such as coarsening and aggregation simultaneously occur in many cases. One way to obtain monodisperse nanoparticles is the two-stage growth method: in the first stage, rapid heating causes fast supersaturated-burst nucleation, and in the second stage, the gradual precipitation of solute atoms at a temperature below the critical point of supersaturation allows only the existing nanoparticles to grow slowly. In this process, surfactants are often introduced to the solution to prevent coarsening and aggregation. Because all nanoparticles follow the same growth process in this method, their size after growth should in principle be uniform. In practice, different groups have developed particular methods to produce nanoparticles of specific composition and size.

With respect to controlling the shape of a nanoparticle, growth kinetics is essential in addition to thermodynamic stability to minimize surface free energy. For example, if the growth rate for cubic {111} surfaces is slower than for {100} surfaces, the surface area of {100} facets will decrease with growth, and the particles finally become octahedrons of {111} facets only. Similarly, if the growth of {001} surfaces in a hexagonal crystal system is fast, rods or, conversely, plates can be formed. For this reason, the adsorption of surfactants on particular surfaces has been intensively studied to fabricate a desired shape by controlling the growth rate of each surface. Figure 2 shows examples of regular octahedral and cubic nanoparticles [49, 50]. With regard to compositing, nanoparticles dispersed in solution are regularly conjugated by substances such as surfactants to lower their surface energy or prevent aggregation, forming a kind of composite material. Advanced compositing techniques have been developed to protect easily oxidized metal cores or to enable the simultaneous expression of multiple functions. For example, dumbbell-shaped junctions in different kinds of nanoparticles [51] and core-shell structures [27] have been produced recently (Figure 3).

*3.2. Magnetic Nanoparticles to Maximize Heat Dissipation.* Using these advanced synthesis techniques, researchers have fabricated magnetic nanoparticles to maximize heat dissipation based on the guiding principles described above. As an example, I highlight the recent report by Lee et al. [27], who fabricated novel superparamagnetic nanoparticles with a uniform diameter $d$ of 15 nm (see Figure 3 again). One of the reasons why they chose such a size may be to avoid aggregation. In addition, the oscillator of their equipment can generate an AC magnetic field of frequency $f = 500$ kHz. As discussed above, superparamagnetic nanoparticles that have a Néel relaxation time ($\tau_N$) that matches $f$ are required to maximize relaxation loss. Briefly, $\tau_N$ should be $(2\pi f)^{-1} = 318$ ns. (Overall, $\tau$ needs to be set to 400 ns when also considering the Brownian relaxation time $\tau_B = 1.6 \mu$s.) Substituting $\tau_N = 318$ ns in (1), the required energy barrier height ($KV$) is calculated to be $2.4 \times 10^{-20}$ J. This value corresponds to a uniaxial anisotropic particle with $d = 15$ nm and $K = 1.4 \times 10^4$ J/m$^3$. However, examination of parameters such as bulk crystalline magnetic anisotropy [40] revealed that no suitable candidate substances had been reported. For substances with cubic symmetry, the magnitude of $K_1$ and the barrier height, $-(1/12)K_1 V$ for negative $K_1$ or $(1/4)K_1 V$ for positive $K_1$, calculated using $d = 15$ nm are as follows: $-1.2 \times 10^4$ J/m$^3$ and $0.18 \times 10^{-20}$ J (Fe$_3$O$_4$); $-0.46 \times 10^4$ J/m$^3$ and $0.08 \times 10^{-20}$ J ($\gamma$-Fe$_2$O$_3$); $-0.25 \times 10^4$ J/m$^3$ and $0.04 \times 10^{-20}$ J (MnFe$_2$O$_4$); and $18 \times 10^4$ J/m$^3$ and $8.0 \times 10^{-20}$ J (CoFe$_2$O$_4$). As a result, shape control, which affects shape and surface magnetic anisotropy, or composition control or composite structure control, which influences the crystalline magnetic anisotropy, are therefore required. From among the possibilities mentioned, Lee et al. selected core-shell structures of cobalt and manganese ferrites and used a core-and-shell exchange coupling to control the magnitude of effective magnetic anisotropy. As a result, they obtained the core-shell structure shown in Figure 3, with a measured magnetic anisotropy constant $K$ of $1.7 \times 10^4$ J/m$^3$ (Table 1).
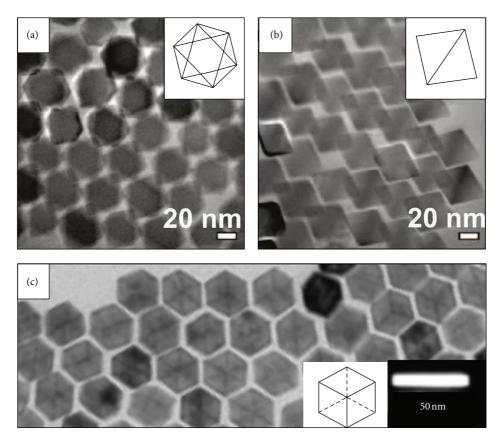
FIGURE 2: Transmission electron micrographs of shape-controlled magnetic nanoparticles with different projection shapes: (a) hexagonal outlines of octahedron-shaped $Fe_3O_4$ nanoparticles (zone axis: $\langle 111 \rangle$), and (b) parallelogram outlines of the same $Fe_3O_4$ nanoparticles as in (a) (zone axis: $\langle 110 \rangle$). *Reproduced from Li et al. [49] with permission (Copyright 2010 American Chemical Society). (c) Hexagonal outlines of cube-shaped Ni-Pt nanoparticles (zone axis: $\langle 111 \rangle$). Private communication (Copyright 2011 B. Jeyadevan).
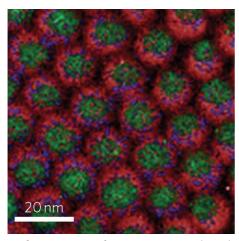


FIGURE 3: Electron energy-loss spectroscopy (EELS) mapping analysis of $CoFe_2O_4@MnFe_2O_4$ nanoparticles, where Co, Fe, and Mn atoms are indicated as green, red, and blue, respectively. *Reproduced from Lee et al. [27] with permission (Copyright 2011 Nature).

TABLE 1: Size, saturation magnetization ($M_s$), anisotropy constant ($K$), and heat dissipation rate per unit weight $P_H$ (at $H_{ac}$ = 37.3 kA/m, $f$ = 500 kHz) of ferrite nanoparticles experimentally determined in [27].

| Sample | Size (nm) | $M_s$ (kA/m) | $K$ (kJ/m$^3$) | $P_H$ (MW/kg) |
|---|---|---|---|---|
| $CoFe_2O_4$ | 12 | 510 | 200 | 0.4 |
| $MnFe_2O_4$ | 18 | 700 | 3 | 0.2 |
| $MnFe_2O_4@CoFe_2O_4$ | 15 | 570 | 17 | 3.0 |

When these core-shell nanoparticles were irradiated with an AC magnetic field of frequency $f$ = 500 kHz and amplitude $H_{ac}$ = 37.3 kA/m, the heat dissipation ($P_H$) per unit weight reached 3 MW/kg (3 kW/g), which was significantly higher than that using nanoparticles of cobalt ferrite (0.4 MW/kg) or manganese ferrite (0.2 MW/kg). The heat generation of these core-shell nanoparticles is unprecedented so they have received widespread attention.

This example suggests optimized design of nanoparticle synthesis has succeeded in producing nanoparticles that generate large amounts of heat. However, further consideration revealed two notable points. First, the actual amplitude of $H_{ac}$ reached 37.3 kA/m or 80% that of the anisotropic magnetic field, $H_K$ = $2K/M_s$ = 47.3 kA/m. This is large enough for the energy barrier to magnetization reversal to disappear because of the Zeeman energy in cases where the direction of the AC magnetic field is not completely parallel to the easy axis of nanoparticles. Thus, these conditions do not permit the application of the guiding principles

given in (2)–(5) because these assume a linear response for superparamagnetic nanoparticles in zero magnetic field limit. This raises the question of whether irradiation with an AC magnetic field with $f$ of 500 kHz and $H_{ac}$ of 37.3 kA/m for core-shell structured nanoparticles with $d$ of 15 nm and $K$ of $1.7 \times 10^4$ J/m$^3$ are really the optimum conditions. However, it is difficult to apply the other guiding principle to maximize hysteresis loss of ferromagnetic nanoparticles because thermally assisted reversals of $\mu$ occur stochastically before the barrier disappears at $H_K$. Recalling that the characteristic time of thermal fluctuation was estimated to be a few hundred nanoseconds even in a zero magnetic field, the conditions used by Lee et al. are outside the scope of applicability of conventional models for ferromagnetic nanoparticles at a temperature of absolute zero and for superparamagnetic nanoparticles in a zero magnetic field. Consequently, new guiding principles to maximize heat dissipation $P_H$ are required. The second point is that $H_{ac} = 37.3$ kA/m is much larger than the exposure restriction for this waveband [52]. This point is examined further in Section 5. The next section will present results of recent numerical studies on the behavior of nanoparticles under conditions outside the scope of applicability of conventional models. This knowledge will be useful to establish sophisticated guiding principles that are adapted to advanced technologies that control the size, shape, and composite structure of nanoparticles.

## 4. Recent Numerical Simulations for Novel Responses to AC Magnetic Fields

To further improve the guiding principles for the design of magnetic nanoparticles, we must clarify the behavior of nanoparticles under conditions outside the scope of applicability of conventional models. However, it is difficult to discuss nonlinear nonequilibrium responses algebraically; as an alternative, numerical simulation has been performed extensively because of recent advances in computing speed. Noteworthy results obtained from these studies will be introduced in this section. To fully discuss their features from the viewpoint of efficiency, the results are shown as the ratio of the simulated value of $P_H$ to the theoretical upper limit of $P_H : P_{H\,\mathrm{Max}}$, where $P_{H\,\mathrm{Max}}$ is expressed as $4\mu_0 M_s H_{ac} \cdot f \cdot \rho^{-1}$ for irradiating AC magnetic field $H_{ac} \sin(2\pi f \cdot t)$, because the loss dissipated in one cycle is the area of the hysteresis loop.

In most of the simulations, it was assumed that magnetic nanoparticles were individually delivered to tumor tissues and accumulate randomly inside them, apart from the present status of this treatment [53]. Because the actual concentration of nanoparticles in tumors $c$ does not exceed 10 kg/m$^3$ (10 mg/cm$^3$) as stated above, effects caused by dipole-dipole interactions $J_{dd}$ between the accumulated nanoparticles were considered insignificant at room temperature. For example, at the mean distance $\langle r \rangle \approx d \cdot \rho^{1/3} \cdot c^{-1/3}$, $J_{dd}/k_B \approx \mu_0 \mu^2 / (\langle r \rangle^3 k_B)$ is estimated to be 25 K for magnetite nanoparticles with $d = 15$ nm, $M_s = 450$ kA/m, and $c = 10$ kg/m$^3$. Thus, the nanoparticles in this hyperthermia treatment simulation were considered magnetically isolated from each other.

*4.1. Néel Relaxation in Magnetic Fields.* In a magnetically isolated nanoparticle, the potential energy, $U$, with respect to the direction of $\mu$ is simply given by the sum of magnetic anisotropy energy and Zeeman energy. As a first approximation, uniaxial magnetic anisotropy has usually been assumed for the former term, although it contains contributions from various kinds of magnetic anisotropy such as shape, crystalline, and surface anisotropy. In this case, $U$ can be expressed as

$$U(\phi, \psi) = KV\sin^2\phi - \mu_0\mu H_{ac} \sin(2\pi f \cdot t)\cos\psi, \qquad (6)$$

where $\phi$ is the angle between the easy axis and $\mu$, and $\psi$ is the angle between $\mu$ and $\mathbf{H}$. The detailed trajectories of $\mu$ in this potential can be precisely simulated by solving the stochastic Landau-Lifshitz-Gilbert equations [53–57]. However, we are only interested in the reversal of $\mu$ once every microsecond because the frequency used for hyperthermia treatment is limited. Carrey et al. calculated the behavior of $\mu$ using a well-known coarse-grained approach or "two-level approximation" [58, 59], which considers thermally activated reversals between the metastable directions *via* the midway saddle point in the energy barrier. In this calculation, easy axes of the accumulated nanoparticles were assumed to be fixed. This assumption seems valid when the nanoparticles are strongly anchored to structures resembling organelles.

Figures 4(a), 5(a), and 6(a) show contour plots of $P_H/P_{H\,\mathrm{Max}}$ calculated for cobalt ferrite, manganese ferrite and their core-shell nanoparticles introduced above, respectively, where the time evolution of the occupation probabilities of the directions parallel to the randomly oriented easy axes are simulated in the same way as Carrey et al. using the parameters given in Table 1. At low $H_{ac}$ of 1 kA/m, $P_H/P_{H\,\mathrm{Max}}$ of the core-shell nanoparticles increases with $f$, and a single maximum is found at a peak frequency, $f_p$, of 110 kHz (Figure 6(a)). This behavior is consistent with the above prediction that $P_H$ is maximized when $f^{-1}$ is adjusted to the Néel relaxation time. It is notable that $f_p$ shifts to higher frequency as $H_{ac}$ increases. This acceleration of Néel relaxation can be attributed to lowering of the energy barrier by the Zeeman energy. As indicated by the dashed line in Figure 6(a), the shift of $f_p$ can be explained by $\tau_N(H_{ac})$ calculated using the conventional Brown's equation as follows [60]:

$$
\begin{aligned}
\left[\tau_N\left(H_{ac}\right)\right]^{-1} &= f_0 \cdot \left(1 - h^2\right) \\
&\times \left\{ (1+h)\exp\left[\left(\frac{-KV}{k_BT}\right)(1+h)^2\right] \right. \\
&\left. + (1-h)\exp\left[\left(\frac{-KV}{k_BT}\right)(1-h)^2\right] \right\},
\end{aligned}
\qquad (7)
$$

where $h$ is $H/H_K$. In Figure 6(a), $f_p$ at $H_{ac} = 20$ kA/m, a typical $H_{ac}$ for hyperthermia treatment, is about 40 times faster than that in a zero magnetic field. This fact clearly indicates that maximum heat dissipation cannot be obtained if we prepare nanoparticles according to the conventional guiding principles expressed in (1)–(5). This problem becomes serious
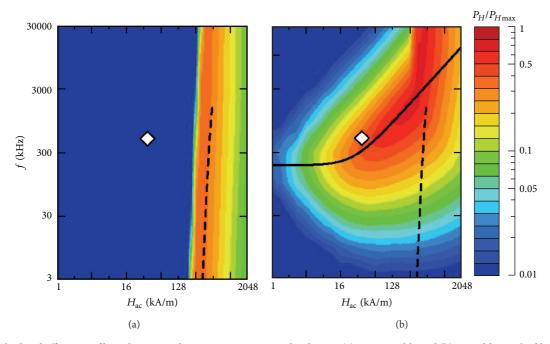
FIGURE 4: Calculated efficiency of heat dissipation by $CoFe_2O_4$ nanoparticles that are (a) nonrotatable and (b) rotatable. Dashed lines represent the Néel relaxation time $(2\pi\tau_N)^{-1}$ and the solid line indicates $f_p$, which was calculated using (11). Diamonds denote the conditions used in the experiment.
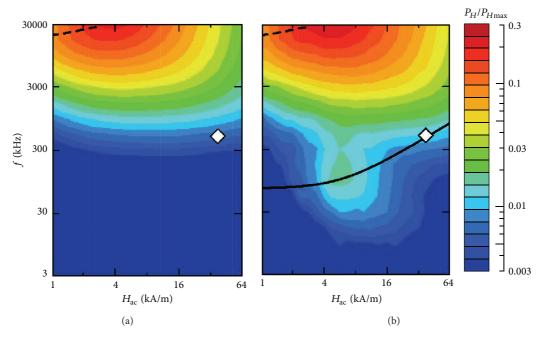


FIGURE 5: Calculated efficiency of heat dissipation by $MnFe_2O_4$ nanoparticles that are (a) non-rotatable and (b) rotatable. Dashed lines represent the Néel relaxation time $(2\pi\tau_N)^{-1}$ and the solid line indicates $f_p$, which was calculated using (11). Diamonds denote the conditions used in the experiment.

when monodisperse nanoparticles are synthesized, although we barely noticed the problem because we used polydisperse nanoparticles with a broad distribution of $\tau_N$.

It is very important that these calculated results are compared with experimental data, even under only one set of conditions with $f = 500\,kHz$ and $H_{ac} = 37.3\,kA/m$.

In Figure 6(a), 40% of $P_{H\,Max}$, that is 1.4 MW/kg, is expected for the core-shell nanoparticles at $f = 500\,kHz$ and $H_{ac} = 37.3\,kA/m$ (diamonds), whereas a larger value of 3.0 MW/kg was actually observed. In Figure 4(a), almost zero dissipation was calculated for the cobalt ferrite nanoparticles under the same conditions, because these nanoparticles
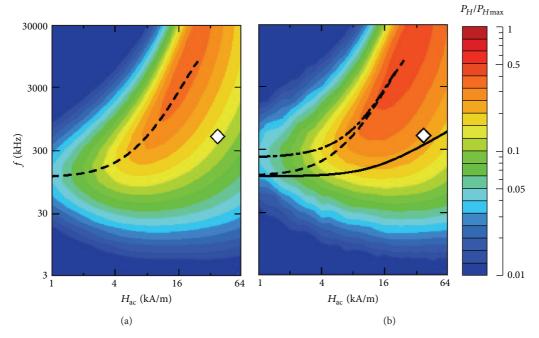
FIGURE 6: Calculated efficiency of heat dissipation by core-shell nanoparticles that are (a) non-rotatable and (b) rotatable. Dashed lines represent the Néel relaxation time $(2\pi\tau_N)^{-1}$, the solid line indicates $f_p$, which was calculated using (11), and the dashed-dotted line shows the value calculated using (12). Diamonds denote the conditions used in the experiment.

are ferromagnetic, so no hysteresis loss is dissipated when $H_{ac}$ = 37.3 kA/m because it is sufficiently lower than $H_K$ = 630 kA/m. In contrast, considerable dissipation of 0.4 MW/kg was experimentally reported for the cobalt ferrite nanoparticles. In Figure 5(a), a small amount of dissipation is expected for the manganese ferrite nanoparticles under the same conditions, because these nanoparticles are typically superparamagnetic and little relaxation loss dissipates at $f$ = 500 kHz that is sufficiently lower than $[2\pi\tau_N(H_{ac})]^{-1}$ of several tens of megahertz. However, a considerable dissipation of 0.2 MW/kg was experimentally reported for the manganese ferrite nanoparticles. Some of these inconsistencies may be attributed to the fact that the magnetic nanoparticles were easily rotatable in a low viscous liquid of toluene. Hence, Brownian rotations would be described next.

*4.2. Brownian Relaxation in Magnetic Fields.* In this subsection, ferromagnetic nanoparticles in Newtonian fluids are considered because toluene is a typical Newtonian fluid ($\eta$ = 0.55 mPa·s), although the actual microviscoelasticity of the local environment in cancer cells is still unknown. In this case, the inertia of nanoparticles with a typical size of 10 nm can be neglected in considering their rotation by Brownian dynamics simulation [61, 62]. In the inertia-less limit, frictional torque for the rotation of a sphere balances with magnetic torque $\mu(t) \times H(t)$ and Brownian torque $\lambda(t)$ as follows:

$$6\eta V_H \cdot \boldsymbol{\omega}(t) = \mu_0\boldsymbol{\mu}(t) \times \mathbf{H}(t) + \boldsymbol{\lambda}(t) \qquad (8)$$

$$\langle \lambda_i(t) \rangle = 0, \qquad (9)$$

$$\langle \lambda_i(t_1)\,\lambda_i(t_2) \rangle = 2k_B T \cdot (6\eta V_H) \cdot \delta(t_1 - t_2), \qquad (10)$$

where $\boldsymbol{\omega}(t)$ is the angular velocity of rotation for the unit vector $\mathbf{e}(t)$ along the easy axis given by $de/dt = \boldsymbol{\omega}(t) \times \mathbf{e}(t)$, and $\delta(t_1 - t_2)$ is the Dirac delta function. Yoshida and Enpuku [63] simulated the rotation of ferromagnetic nanoparticles using the Fokker-Planck equation equivalent to the above relationships; they assumed that $\boldsymbol{\mu}(t)$ was permanently fixed at the direction parallel to $\mathbf{e}(t)$ as long as $H_{ac} < H_K$. As a result, they confirmed that, at zero magnetic field limit, the frequency-dependence of heat dissipation exhibits a single maximum at $f_p = (2\pi\tau_B)^{-1}$, as predicted by (2)–(5). They also found that $f_p$ increases with $H_{ac}$ according to the equation:

$$2\pi f_p \approx \tau_B^{-1}\left[1 + 0.07\left(\frac{\mu_0\mu H_{ac}}{k_B T}\right)^2\right]^{0.5}$$

$$\approx \begin{cases} \tau_B^{-1} & \text{at } \mu_0\mu H_{ac} \ll k_B T \\ 0.5\left(\dfrac{\mu_0\mu H_{ac}}{6\eta V_H}\right) & \text{at } \mu_0\mu H_{ac} \gg k_B T. \end{cases} \qquad (11)$$

This equation indicates that the driving force of the rotation changes from Brownian random torque to magnetic torque as $H_{ac}$ increases.

As an example, this equation is applied to the cobalt ferrite nanoparticles discussed above. The solid curve in Figure 4(b) shows the values of $2\pi f_p$ calculated using (11) with the parameters in Table 1. The obtained line is close to the position of the diamond located at $f$ = 500 kHz and $H_{ac}$ = 37.3 kA/m. In other words, the magnetic torque from the magnetic field at 37.3 kA/m happened to satisfy the conditions of rotating the cobalt ferrite nanoparticles

with an appropriate delay to the alternation at 500 kHz; consequently, a considerable amount of heat, 3.7 MW/kg, dissipates. Apart from the magnitude, this is the reason why $P_H = 0.4$ MW/kg was experimentally observed for the cobalt ferrite nanoparticles, despite the conventional prediction of no hysteresis loss under the experimental conditions. As exemplified here, delayed rotations are caused by magnetic torque (not Brownian torque) even at $H_{\mathrm{ac}}$ much lower than $H_K$, resulting in significant heat dissipation.

Researchers are also interested in the magnetic response when $H_{\mathrm{ac}}$ becomes comparable to $H_K$. In this case, the abovementioned assumption that $\boldsymbol{\mu}(t)$ is permanently fixed at the direction parallel to $\mathbf{e}(t)$ is invalid, because $\boldsymbol{\mu}(t)$ is canted from the easy axis by the Zeeman energy. Furthermore, $\boldsymbol{\mu}(t)$ stochastically reverses by thermal fluctuations even in ferromagnetic nanoparticles, because the Zeeman energy lowers the barrier height sufficiently. Therefore, I simultaneously computed the rotations of the nanoparticles using (8)–(10) with the thermally activated reversals of $\boldsymbol{\mu}(t)$ on the potential given by (6) [64]. Note that (8) is valid within the two-level approximation [65]. The results calculated for these cobalt ferrite nanoparticles are shown as the contour lines (and color difference) in Figure 4(b). Firstly, we are certain that, at $H_{\mathrm{ac}} \ll H_K \approx 630$ kA/m, the location of the ridge in the contour plot of $P_H/P_{H\,\mathrm{Max}}$ is consistent with the solid line given by (11). This result indicates that ferromagnetic nanoparticles are rotated by the magnetic torque before the reversal of $\boldsymbol{\mu}(t)$ occurs within it. However, the ridge seems turn to the position extrapolated from the dashed curve given by (7) when $H_{\mathrm{ac}}$ becomes comparable to $H_K$. In other words, $\boldsymbol{\mu}(t)$ is promptly reversed before the rotation because the Néel relaxation is accelerated enough in this $H_{\mathrm{ac}}$ range. These relationships can be written as

$$2\pi f_p \approx \left[\tau_N\left(H_{\mathrm{ac}}\right)\right]^{-1} + \tau_B^{-1}\left[1 + 0.07\left(\frac{\mu_0\mu H_{\mathrm{ac}}}{k_B T}\right)^2\right]^{0.5}. \tag{12}$$

This equation is an extended relationship of $\tau^{-1} = \tau_N^{-1} + \tau_B^{-1}$ ((3)) for a large AC magnetic field. It is noteworthy that the first term $\tau_N(H_{\mathrm{ac}})$ usually becomes extremely small for ferromagnetic nanoparticles at $H_{\mathrm{ac}} \approx H_K$ in an aligned case ($\mathbf{e}//\mathbf{H}$) or at $H_{\mathrm{ac}} \approx H_K/2$ in tilted cases, while the second term is approximately expressed as $0.5(\mu_0\mu H_{\mathrm{ac}}/6\eta V_H)$ when $\mu_0\mu H_{\mathrm{ac}} \gg k_B T$. Therefore, the changeover from rotation to reversal occurs at $2\pi f \approx 0.5(\mu_0\mu H_K/6\eta V_H) = KV/(6\eta V_H)$ or $KV/(12\eta V_H)$ for aligned and tilted cases, respectively. For example, this changeover frequency corresponds to 4 MHz for the aligned cobalt ferrite nanoparticles with $d = 12$ nm, $V/V_H = 0.63$, $K = 200$ kJ/m$^3$, and $\eta = 0.55$ mPa·s. Importantly, the changeover frequency is independent of the size of nanoparticles as long as the ratio $V/V_H$ is constant. In other words, rotations predominate over the magnetic response at 1 MHz even for much larger cobalt ferrite nanoparticles ($d = 120$ nm, $(2\pi\tau_B)^{-1} = 200$ Hz). We must keep in mind that, even when ferromagnetic nanoparticles are large enough for their Brownian relaxation to be negligible, magnetic torque can easily rotate such nanoparticles at a time scale of microseconds if they are in a liquid phase. This

knowledge is helpful when considering the optimal frequency for hyperthermia treatment, even if it is for a simplified system.

*4.3. Easy Axes Oriented to the Directions Parallel, Perpendicular, or Oblique to the AC Field.* As described above, the fast reversals of $\boldsymbol{\mu}(t)$ are predominant in the magnetic response of ferromagnetic nanoparticles at frequencies higher than the changeover frequency. The simulations, however, revealed that, at the frequencies, the rotation induces various kinds of stationary orientations of the easy axes $\mathbf{e}(t)$, which critically affect the reversals [64, 66]. In this section, we also examine the results determined for cobalt ferrite nanoparticles with $d = 12$ nm, $V/V_H = 0.63$, $K = 200$ kJ/m$^3$, and $\eta = 0.55$ mPa·s. In the initial state before irradiation with the AC magnetic field, the easy axes are set to be randomly oriented in the fluid, as shown in Figure 7(a). Therefore, in the first cycle, the major hysteresis loop obtained at $H_{\mathrm{ac}} = 640$ kA/m $> H_K$ is consistent with the magnetization curve predicted by the Stoner-Wohlfarth model (see the inset). If the irradiation of the AC magnetic field at $H_{\mathrm{ac}} = 640$ kA/m is continued in the simulation, the easy axes gradually turn toward the direction parallel to $\mathbf{H}$. Note that, in the case where the easy axis is not parallel to $\mathbf{H}$, the direction of $\boldsymbol{\mu}$ is not completely parallel to $\mathbf{H}$ even though $\boldsymbol{\mu}$ is already reversed at $H \geq H_K$. Therefore, a large magnetic torque proportional to $\sin\psi$ can turn the easy axis even if the magnetization seems almost saturated at $H \approx H_K$. For example, $\sin\psi$ is 0.43 when $\cos\psi$ is 0.9. Consequently, a longitudinally oriented structure of the easy axes is formed in the fluid (see Figure 7(d)). The formation of this nonequilibrium structure makes the dynamic hysteresis loop squarer than the initial curve, as shown in the inset of upper panel of Figure 7(d).

In contrast, the magnetization curve at $H_{\mathrm{ac}} = 300$ kA/m $< H_K/2$ is a minor hysteresis loop, as shown in Figure 7(b). In this case, the easy axis turns toward the direction perpendicular to $\mathbf{H}$ and they maintain planar orientations if the ferromagnetic nanoparticles are continuously irradiated by an AC magnetic field at $H_{\mathrm{ac}} = 300$ kA/m. A question now arises because we know that the longitudinal orientation is preferred when the Zeeman energy is considered. To clarify the reason for this, we consider an initial state in which a nanoparticle with an easy axis at angle $\theta$ has a magnetic moment $\boldsymbol{\mu}$ at a parallel direction $\psi = \theta$. When a small magnetic field $H < H_K/2$ is applied to the nanoparticle, $\boldsymbol{\mu}$ immediately tilts to $\psi = \theta - \phi$ without reversals (see Figure 7(e)), because the position of the local minimum on $U(\phi, \psi)$ is changed. Then, the magnetic torque, $-\mu_0\mu H \sin(\theta - \phi)$, rotates $\boldsymbol{\mu}$ toward the longitudinal direction: $\psi \to 0$. Because $\boldsymbol{\mu}$ drags the easy axis, $\theta$ also decreases. In other words, the easy axis turns toward the direction parallel to $\mathbf{H}$. If $\mathbf{H}$ is reversed subsequently, the direction of $\boldsymbol{\mu}$ at this moment is almost antiparallel to $\mathbf{H}$ at $\psi = \theta + \pi - \phi$. Then $\psi$ instantly changes to $\theta + \pi + \phi$ because of the effect of variation of the minimum on $U(\phi, \psi)$ (see Figure 7(e)). The magnetic torque at this stage, $-\mu_0\mu H \sin(\theta + \pi + \phi) = \mu_0\mu H \sin(\theta + \phi)$, forces $\boldsymbol{\mu}$ to rotate toward the direction $\psi = 2\pi$ *via* $\psi = (3/2)\pi$. Because $\boldsymbol{\mu}$ is bound on the easy axis, $\theta$ also increases. In other words,
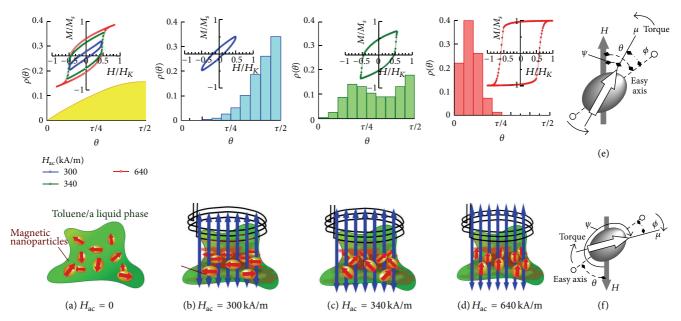
FIGURE 7: Calculated orientation distribution of the easy axes $\rho(\theta)$ of $CoFe_2O_4$ nanoparticles in (a) thermal equilibrium at $H = 0$, and (b)–(d) nonequilibrium steady states under AC magnetic field at various $H_{ac}$ and $f = 30$ MHz. The inset shows the dynamic hysteresis loops. Diagrams of the magnetic torques in the AC field are depicted in (e) and (f), where the ellipsoid in each figure shows a nanoparticle, and the broken line, open and closed arrows indicate the directions of the easy axis, magnetic moment of the particle, and the AC magnetic field, respectively. The nonequilibrium structures under the high-frequency AC magnetic field are illustrated in the sketches in the lower column.

the easy axis starts to turn toward the plane perpendicular to **H**. If the direction of **H** alternates at a high frequency, a planar orientation of the easy axis is formed on average, because $\mu_0\mu H \sin(\theta + \phi)$ is larger than $\mu_0\mu H \sin(\theta - \phi)$. This reduces the remanence of the hysteresis loop. In contrast, a longitudinal orientation is formed in a large AC magnetic field $H \geq H_K$ as discussed above, because $\mu$ is always reversed to the direction parallel to **H** immediately after **H** is reversed. Overall, $\theta$ decreases toward 0 when the reversal of $\mu$ occurs with alternation of the direction of **H**, whereas $\theta$ increases toward $\pi/2$ without reversal of $\mu$.

This feature leads to formation of novel nonequilibrium structures such as the obliquely oriented state found at an intermediate amplitude of $H_{ac} = 340$ kA/m. Without considering thermal fluctuations, the reversals should occur in the range of $\theta$ from $0.15\pi$ to $0.35\pi$ for Stoner-Wohlfarth nanoparticles with $H_K = 630$ kA/m, while $\mu$ never reverses in the other ranges. If this feature simply applies, $\theta$ should decrease with time in the range between $0.15\pi$ and $0.35\pi$, whereas it should increase both between 0 and $0.15\pi$ and between $0.35\pi$ and $\pi/2$. These variations certainly lead to formation of a bimodal $\rho(\theta)$ with double maxima at $\theta = 0.15\pi$ and $\pi/2$, as found in Figure 7(c). Consequently, the easy axes are oriented in both the planes perpendicular and oblique to the magnetic field.

Concisely, in ferromagnetic nanoparticles in toluene or an aqueous phase, longitudinal, conical, or planar orientations are formed, irrespective of the free energy, as nonequilibrium structures under a high-frequency AC magnetic field. As a result, the major hysteresis loop becomes squarer and the minor loop becomes narrower compared with

the magnetization curve calculated for randomly oriented nanoparticles. These variations of the area of the loops cause the maximum of $P_H/P_{H\,\text{Max}}$ to shift towards higher $H_{ac}$ from the optimal conditions predicted by the conventional models in Section 2. This kind of averaging of the oscillating rotations, discussed using the cobalt ferrite nanoparticles as an example, should always occur as long as the alternation of the magnetic field is much more frequent than the characteristic time of rotation, $0.5(\mu_0\mu H_{ac}/6\eta V_H)$. For this reason, these nonequilibrium structures would form in the radio-waveband used for hyperthermia treatment if the amplitude is somewhat smaller ($\sim$10 kA/m) or the viscosity is considerably higher ($\sim$10 mPa·s). Therefore, we must keep in mind the important effects of nonequilibrium structures on heat dissipation when establishing the optimal design of ferromagnetic nanoparticles for hyperthermia treatment.

*4.4. Magnetic Hysteresis of Superparamagnetic States.* Let us leave ferromagnetic nanoparticles and move on to superparamagnetic manganese ferrite nanoparticles, from which a considerable amount of heat dissipation, 0.2 MW/kg, was experimentally reported at $f = 500$ kHz. The orientation of $\mu$ on these nanoparticles is easily equilibrated in the magnetic potential expressed in (6) within the scale of the Néel relaxation time $\tau_N(H_{ac} = 0)$ of $1 \times 10^{-8}$ s. Therefore, little relaxation loss is expected using the conventional model. For this reason, I wish to examine this inconsistency from the viewpoint of the effects of slow rotations on the fast reversals in superparamagnetic nanoparticles.

The contour lines (and color difference) in Figure 5(b) show the results obtained from the simultaneous simulation
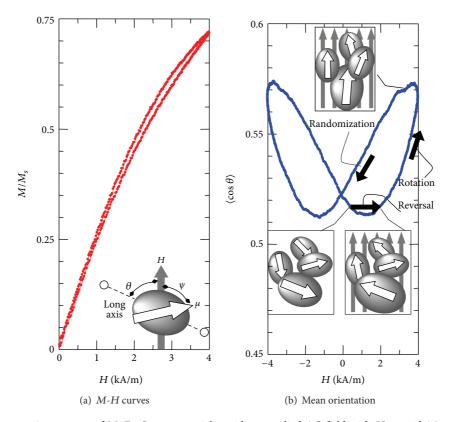
(a) $M$-$H$ curves

(b) Mean orientation

FIGURE 8: Calculated magnetic response of $MnFe_2O_4$ nanoparticles with an applied AC field with $H_{ac} = 4\,kA/m$ and $f = 100\,kHz$. (a) Steady magnetization curves, and (b) mean orientation of the easy axis of the nanoparticles, $\langle \cos \theta \rangle$. In the inset in (a), the ellipsoid shows a nanoparticle, and the broken line, open and closed arrows indicate the directions of the easy axis, magnetic moment of the particle, and the AC magnetic field, respectively. The variation of easy axis orientations is illustrated in the sketches in (b).

of rotations and reversals for the manganese ferrite nanoparticles. Firstly, we find a secondary maximum of $P_H/P_{H\,Max}$ around $f = 100\,kHz$ in addition to the primary ridge of $P_H/P_{H\,Max}$ indicated by the dashed curve at frequencies of several tens of megahertz, which is explained by (7) for $\tau_N(H_{ac})$ above. To clarify the origin of the new kind of heat dissipation, the magnetization curve calculated under the conditions of $H_{ac} = 4\,kA/m$ and $f = 100\,kHz$ is presented in Figure 8(a). An S-shaped hysteresis loop without remanence is observed. In this cycle, the directions of the easy axes have butterfly-shaped hysteresis, as shown in Figure 8(b). This behavior is explained by the following atypical magnetic response in the period $f^{-1}$ (10 $\mu$s). Initially (at $t = 0$), no magnetization exists because the occupation probabilities of $\mu$ in the two stable directions parallel to the easy axis are equalized in a zero magnetic field. As $H$ increases, the occupation probability in the more stabilized direction immediately increases because of reversals on a time scale of $\tau_N$ ($\leq$10 ns). The reversed $\mu$ in the stabilized direction is not completely parallel to $H$, $\psi \neq 0$, and the magnetic torque $\mu_0 \mu H \sin \psi$ turns the easy axis towards the direction of the field. The time constant of this process is approximately expressed as $[0.5(\mu_0 \mu H_{ac}/6\eta V_H)]^{-1}$ using the second term in (11). For the manganese ferrite nanoparticles, it is 3 $\mu$s when $H$ is 4 kA/m. Therefore, rotation is not negligible in the peak period of the oscillations of $H$. Subsequently, $H$ decreases to

zero at $t = 0.5f = 5\,\mu$s, and the occupation probabilities are again equalized because reversal is rapid, so the magnetic torque disappears. Alternatively, the Brownian torque randomizes the orientation of the easy axis on a time scale of $\tau_B$ (= 2 $\mu$s). Therefore, competition between the magnetic and Brownian torques can cause the butterfly-shaped hysteresis of $\langle \cos \theta \rangle$. Because the equilibrium magnetization of the superparamagnetic nanoparticles with easy axes parallel to $H$ is higher than that of randomly oriented ones [58, 67], the magnetization curve shows hysteresis without remanence. Consequently, a secondary maximum appears even though $\tau_N \ll \tau_B$ if the nanoparticles are rotatable. As discussed here, we should remove the stereotype of a single peak at a $2\pi f_p$ value of $\tau^{-1}(= \tau_N^{-1} + \tau_B^{-1})$.

Needless to say, there is still room for further study. For example, $P_H$ simulated at $f = 500\,kHz$ and $H_{ac} = 37.3\,kA/m$ is 0.13 MW/kg, which is inconsistent with the observed $P_H$ of 0.2 MW/kg. At present, it is unclear whether the difference can be attributed to the nontrivial polydisperse nature of the prepared sample or the accuracy of the simulations, because the experiment was performed under only one set of conditions with $f = 500\,kHz$ and $H_{ac} = 37.3\,kA/m$. Thus, measurement of $P_H$ under various conditions will be helpful to establish a model of heat dissipation in superparamagnetic nanoparticles. In addition, it is certain that the protocols of these simulations are also improvable, because it has been

assumed that the direction of $\mu$ is fixed at one of the local minima in the energy potential given by (6), although we know $\mu$ stochastically explores all over the potential well [65]. Briefly, the magnetic torque is overestimated. Recently, more strict calculations were carried out and they also show the same kind of butterfly-shaped hysteresis [67]. As described here, much still remains to be done.

*4.5. Intermediate State between Ferromagnetic and Superparamagnetic Nanoparticles.* Core-shell nanoparticles, which can generate the largest amount of heat out of various nanoparticle structures, fit neither ferromagnetic ($\tau_N(H_{ac} = 0) \gg f^{-1}$) nor superparamagnetic ($\tau_N(H_{ac} = 0) \ll f^{-1}$) conditions. This is because the value of the Néel relaxation time $\tau_N(H_{ac} = 0)$ calculated using the parameters in Table 1 is $1\,\mu$s, which is comparable with the alternation time of the AC magnetic field used in hyperthermia treatment. Furthermore, the Brownian relaxation time $\tau_B$ is also estimated to be $1\,\mu$s. Therefore, it is worth discussing this intermediate case before concluding this section. Figure 6(b) shows the results obtained by simultaneous simulation of rotation and reversal as contour lines (and color difference). In this figure, we are certain that location of the ridge in the contour plot of $P_H/P_{H\,\text{Max}}$ is consistent with neither the dashed curve (7) nor the solid curve (11), but instead with the dashed-dotted curve given by (12). Furthermore, the iso-height contour lines, for example, the boundary between yellow and light green, shift toward lower frequency compared with the randomly fixed case in Figure 6(a). Figure 9 shows the magnetization curve and variation of the directions of the easy axes calculated for the core-shell nanoparticles under the conditions of $H_{ac} = 37.3\,$kA/m and $f = 500\,$kHz. We observe eyeglass-shaped hysteresis in the variation of the directions of the easy axes. This behavior is attributed to complicated competition between normal rotations when $\mu$ is parallel to **H**, counter-rotations when $\mu$ is antiparallel to **H**, and randomization at **H** $\approx 0$. The major point is that the first term seems to dominate the other terms, because the baseline of the eyeglass-shaped oscillations of the easy axes is considerably higher than the 0.5 expected for randomly oriented nanoparticles. This longitudinal orientation makes the dynamic hysteresis loop squarer and leads to an increase in $P_H$ (see Figure 9(a)). In addition to this effect, on average, oscillation of the directions of the easy axes induced by the alternation of the counter-rotations and randomization further increases $P_H$. Indeed, we can observe that the hysteresis loop of the rotatable nanoparticles in Figure 9(a) opens even in the higher magnetic field where the loop of the non-rotatable nanoparticles in Figure 9(a) is closed after all $\mu$ are reversed. Overall, both the phenomena discussed for ferromagnetic and superparamagnetic nanoparticles contribute to amplification of the hysteresis loop area in this intermediate state; as a result, $P_H$ increases from 1.4 MW/kg for the non-rotatable case to 2.4 MW/kg for the rotatable one. We can say that this value is fairly consistent with the observed $P_H$ of 3 MW/kg in consideration that the simulation was carried out for completely isolated monodisperse nanoparticles with uniform uniaxial anisotropy.
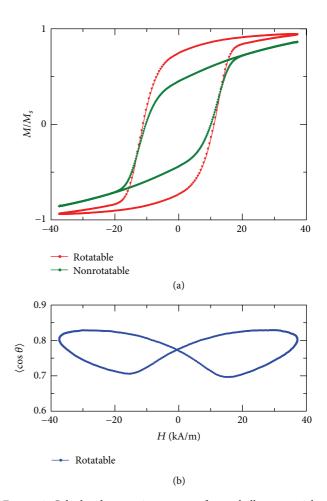


FIGURE 9: Calculated magnetic response of core-shell nanoparticles with an applied AC field with $H_{ac} = 37.3\,$kA/m and $f = 500\,$kHz. (a) Steady magnetization curves, and (b) mean orientation of the easy axis of the nanoparticles, $\langle \cos\theta \rangle$.

## 5. Optimized Design and Future Outlook

Magnetic nanoparticles for thermotherapy, particularly rotatable nanoparticles, have been predicted to exhibit various novel responses to AC magnetic fields, as described above. Examples include magnetic hysteresis observed for superparamagnetic states and nonequilibrium structures with easy axes oriented to the directions parallel, perpendicular, or oblique to the magnetic field. These nonlinear and nonequilibrium phenomena cannot be explained using conventional models. Further systematic simulations and their experimental verification are required to establish sophisticated guiding principles for such magnetic nanoparticles. However, some feel that the heat generation of 3 MW/kg achieved by Lee et al. is sufficient for practical use in hyperthermia treatment, so more sophisticated guidelines may not be necessary. In this final section, we discuss this issue.

Tumors less than 0.01 m (= 1 cm) in size are considered difficult to find with existing diagnostic methods, so here we examine whether or not the heat dissipation from current magnetic nanoparticles is enough to treat hidden tumors of such size. According to Andrä et al. [68], raising

the temperature of a tumor by $\Delta T$ requires heat generation of approximately $3\lambda\Delta T R^{-2}$ without considering blood flow, where $\lambda$ is thermal conductivity and $2R$ is the diameter of a tumor. If we assume $\lambda = 0.6\,\text{WK}^{-1}\,\text{m}^{-1}$, $\Delta T = 5\,\text{K}$, and $2R = 0.005$ or $0.01\,\text{m}$, the required heat generation would be 1.5 or $0.4\,\text{MW/m}^3$, respectively. The rate of blood flow in tumor tissues is typically 1% per second by volume (60 mL/min/100 g) [69]; thus, when $\Delta T = 5\,\text{K}$, the heat transport caused by blood flow is estimated to be $0.2\,\text{MW/m}^3$ using a value of $\sim 4\,\text{MJ-m}^{-3}\,\text{K}^{-1}$ for the specific heat of blood. Therefore, the total cooling power of hidden tumors is between 0.6 and $2\,\text{MW/m}^3$ for $\Delta T = 5\,\text{K}$. This assessment indicates that the amount of heat dissipation $P_H$ required to kill metastatic cancer cells is estimated to be within 0.3 and $1\,\text{MW/kg}$ if we can expect a nanoparticle concentration within tumors of approximately $2\,\text{kg/m}^3$. The developed core-shell magnetic nanoparticles thus clearly enable adequate heat dissipation. However, are they actually suitable for use in hyperthermia treatment?

Note that Section 4 described how nanoparticles with $P_H$ of $3\,\text{MW/kg}$ was obtained from irradiation using an AC magnetic field of $H_{ac} = 37.3\,\text{kA/m}$ and $f = 500\,\text{kHz}$. When this AC magnetic field is irradiated on a simple model body composed of a homogenous column with electrical conductivity $\sigma = 0.2\,\text{Sm}^{-1}$ and radius $r = 0.1\,\text{m}$, the maximum voltage generated on the outer circumference is $V = \pi r^2 2\pi f(\mu_0 H_{ac}) = 4{,}600\,\text{V}$ per revolution, at which point the eddy current loss $P_e = 1/2\pi^2\mu_0^2\sigma r^2 f^2 H_{ac}^2$ is $5\,\text{MW/m}^3$ ($5\,\text{W/cm}^3$). This heat generation is sufficient to raise the temperature of thermally insulated tissues by $10\,\text{K}$ or more in 10 seconds. For this reason, we cannot ignore the side effects of $P_e$ on normal tissues, although the model assuming a constant $\sigma$ is oversimplified. According to guidelines published by the International Commission on Non-Ionizing Radiation Protection [52], the upper limit for work-related exposure of the torso is $10\,\text{W/kg}$ (corresponding to $0.01\,\text{MW/m}^3$). However, because this value is the upper limit for routine exposure, it may not be indicative of the maximum exposure in medical treatment. A slightly more specific value can be calculated as follows. Heat generation only occurs in the outer edge of a human body if a magnetic field is irradiated over the whole body; therefore, the heated region can be considered as a cylinder that is a few centimeters thick. This region can be cooled from the body surface area in medical treatment. Its cooling power, $\lambda\partial^2 T/\partial r^2 \sim \lambda\Delta T(\Delta r)^{-2}$, is roughly estimated to be $0.03\,\text{MW/m}^3$ under the conditions of $\Delta T = 20\,\text{K}$ and $\Delta r = 0.02\,\text{m}$. Because blood vessels expand when temperature rises, blood flow increases even in tissues with little blood flow normally. In subcutaneous tissues, for example, a blood flow rate of approximately 0.2% per second by volume (12 mL/min/100 g) has been reported at $42°\text{C}$ [69, 70]. Under these conditions, calculating the heat transport caused by blood flow using the same method yields a value of $0.03\,\text{MW/m}^3$ when the temperature difference from the outside of the irradiated region is set at $\Delta T = 4\,\text{K}$. These values are the result of rough calculations that do not consider the detailed structure of a human body [71],

but their sum, which is about $0.06\,\text{MW/m}^3$, can be used as an approximation of cooling ability. When a magnetic field is applied to the model body mentioned above, this value corresponds to $P_e$ for the condition $H_{ac}f = 2 \times 10^9\,\text{Am}^{-1}\,\text{s}^{-1}$. Calculating the behavior of the above-mentioned core-shell nanoparticles ($d = 15\,\text{nm}$) within this restriction (see Figure 10) shows that $P_H$ does not reach the requirement of $0.3\,\text{MW/kg}$. However, Figure 10 indicates that if the size of the particle is increased slightly, sufficient $P_H$ can be obtained from the rotatable nanoparticles at higher $H_{ac}$ (equivalent to lower $f$) even under this restriction, and adequate heating is expected inside hidden tumors with a diameter of $0.01\,\text{m}$ without serious side effects on normal tissues from $P_e$.

Our discussion up to this point applies to treatment using continuous irradiation where heat balance holds. Irradiation time and interval can be controlled in medical treatment. For example, when tumors with a specific heat of $4\,\text{MJm}^{-3}\,\text{K}^{-1}$ containing the above-mentioned core-shell nanoparticles with a concentration $c$ of $2\,\text{kg/m}^3$ were irradiated with an AC magnetic field of $H_{ac} = 37.3\,\text{kA/m}$ and $f = 500\,\text{kHz}$, heat of approximately $cP_H = 6\,\text{MW/m}^3$ was generated. Relative to this value, the quantity of heat diffused to the surrounding areas from 10 mm tumors is negligible when $\Delta T < 5\,\text{K}$; thus, the temperature will rise by 5 K after approximately 3 seconds. Because the eddy current loss $P_e$ in this case is $5\,\text{MW/m}^3$, it will take approximately 4 seconds for the temperature of normal tissue to rise by 5 K. Stopping irradiation after 3 seconds will thus enable selective heating of tumors by 5 K or more. This is an extreme example; however, it does indicate that there is another option apart from continuous irradiation. The ratio of $cP_H$ to $P_e$ is important. Although obtaining robust values requires detailed protocol, a factor of 4-5 or so might be a criterion for $cP_H/P_e$. As an example, we calculated $cP_H/P_e$ for the core-shell nanoparticles and found that this condition is satisfied for lower frequencies/smaller amplitudes than those indicated by the solid line in Figure 11 [72]. This finding reflects the fact that $P_H$ is the area of the $M$-$H$ curve $\times$ frequency, which is proportional to $H_{ac}f$ at most, whereas $P_e$ increases in proportion to $(H_{ac}f)^2$, as previously described. Because it is impossible to attain a rise in temperature of 5 K if $cP_H$ is at least 0.6 (or 2) $\text{MW/m}^3$, irradiation must therefore be conducted using a higher frequency and larger amplitude to ensure that this condition is met (see dashed lines in Figure 12 [72]). Ultimately, stronger, faster conditions are needed to destroy cancer cells, and weaker, slower conditions are needed to limit damage to normal tissue. Using the core-shell nanoparticles of $d = 15\,\text{nm}$, a frequency of $f = 500\,\text{kHz}$ is thus acceptable, but $H_{ac}$ needs to be maintained at 9 kA/m to resolve the conflicting requirements.

As discussed above, the combination of the core-shell nanoparticles of $d = 15\,\text{nm}$ and $K = 1.7 \times 10^4\,\text{J/m}^3$ with an AC magnetic field of $f = 500\,\text{kHz}$ and $H_{ac} = 37.3\,\text{kA/m}$ may not be optimal. A narrow range of combinations of these parameters will facilitate efficient hyperthermia treatment and prevent side effects. We have not yet optimized the conditions for hyperthermia treatment; however, establishing the optimal combinations may be difficult, particularly if
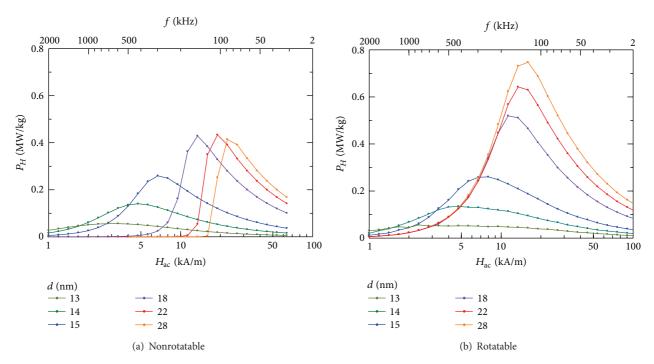
(a) Nonrotatable

(b) Rotatable

FIGURE 10: Calculated heat dissipation by core-shell nanoparticles that are (a) non-rotatable and (b) rotatable, where $H_{ac}f$ is always $2 \times 10^9$ Am$^{-1}$ s$^{-1}$ (corresponding to the restriction that the eddy current loss $P_e$ is 0.06 MW/m$^3$ in normal tissue). The size $d$ is changed in the simulation, but the other parameters were fixed at the values shown in Table 1.
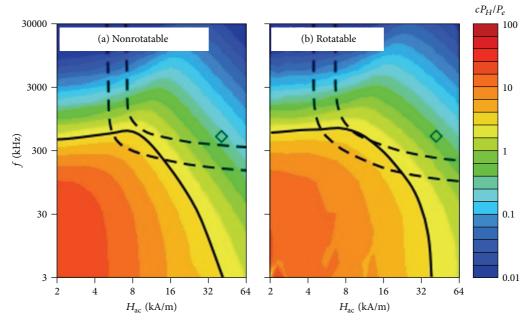


FIGURE 11: Calculated selection ratio $cP_H/P_e$ for core-shell nanoparticles in AC magnetic fields with various $H_{ac}$ and $f$. Rotatable nanoparticles are compared with randomly oriented ones. The dashed lines show the isoplethic curves at $P_H = 0.3$ and 1 MW/kg (see **Figure 12**), while the solid lines show the isoplethic curves at $cP_H/P_e = 4$. *Reproduced from Mamiya [72] with permission (Copyright 2012 TIC).

a trial and error approach is used. The routes used to synthesize magnetic nanoparticles of controlled size, shape, and composite structure have become increasingly advanced, as described in this paper. Dramatic advances in computing speed have also promoted numerical simulation of non-linear nonequilibrium responses to AC magnetic fields. If

we continue to improve material design on the bases of such advanced nanotechnology and computer simulations, optimal conditions will eventually be clarified. Remarkable advances are still continually being reported in clinical trials are being conducted, even though the combination of nanoparticles and oscillation of the equipment has not been
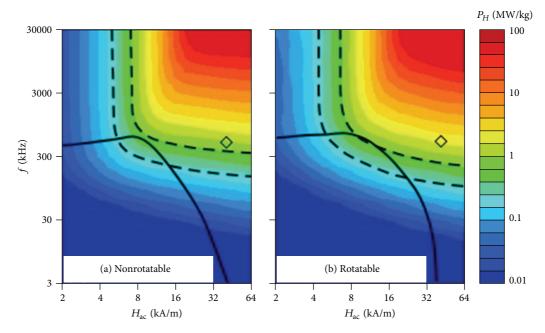
FIGURE 12: Calculated magnetic loss $P_H$ for core-shell nanoparticles in AC magnetic fields for various $H_{ac}$ and $f$. Rotatable nanoparticles are compared with randomly oriented ones. The dashed lines show the isoplethic curves at $P_H = 0.3$ and $1\,\text{MW/kg}$, while the solid lines show the isoplethic curves at the selection ratio $cP_H/P_e = 4$ (see **Figure 11**). *Reproduced from Mamiya [72] with permission (Copyright 2012 TIC).

optimized yet [73, 74]. Once optimization improves local heating ability, then thermotherapy should be established as a fourth or fifth standard cancer treatment method to reduce the disease burden of a patient.

## Acknowledgment

## References

[1] W. C. Dewey, L. E. Hopwood, S. A. Sapareto, and L. E. Gerweck, "Cellular responses to combinations of hyperthermia and radiation," *Radiology*, vol. 123, no. 2, pp. 463–474, 1977.

[2] S. Mornet, S. Vasseur, F. Grasset, and E. Duguet, "Magnetic nanoparticle design for medical diagnosis and therapy," *Journal of Materials Chemistry*, vol. 14, no. 14, pp. 2161–2175, 2004.

[3] P. Tartaj, M. Del Puerto Morales, S. Veintemillas-Verdaguer, T. González-Carreño, and C. J. Serna, "The preparation of magnetic nanoparticles for applications in biomedicine," *Journal of Physics D*, vol. 36, no. 13, pp. R182–R197, 2003.

[4] T. Neuberger, B. Schöpf, H. Hofmann, M. Hofmann, and B. von Rechenberg, "Superparamagnetic nanoparticles for biomedical applications: possibilities and limitations of a new drug delivery system," *Journal of Magnetism and Magnetic Materials*, vol. 293, no. 1, pp. 483–496, 2005.

[5] Q. A. Pankhurst, N. K. T. Thanh, S. K. Jones, and J. Dobson, "Progress in applications of magnetic nanoparticles in biomedicine," *Journal of Physics D*, vol. 42, no. 22, Article ID 224001, 2009.

[6] K. M. Krishnan, "Biomedical nanomagnetics: a spin through possibilities in imaging, diagnostics, and therapy," *IEEE Transactions on Magnetics*, vol. 46, no. 7, pp. 2523–2558, 2010.

[7] B. Jeyadevan, "Present status and prospects of magnetite nanoparticles-based hyperthermia," *Journal of the Ceramic Society of Japan*, vol. 118, no. 1378, pp. 391–401, 2010.

[8] I. Sharifi, H. Shokrollahi, and S. Amiri, "Ferrite-based magnetic nanofluids used in hyperthermia applications," *Journal of Magnetism and Magnetic Materials*, vol. 324, no. 6, pp. 903–915, 2012.

[9] S. J. DeNardo, G. L. DeNardo, A. Natarajan et al., "Thermal dosimetry predictive of efficacy of 111In-ChL6 nanoparticle AMF-induced thermoablative therapy for human breast cancer in mice," *Journal of Nuclear Medicine*, vol. 48, no. 3, pp. 437–444, 2007.

[10] P. Wust, U. Gneveckow, M. Johannsen et al., "Magnetic nanoparticles for interstitial thermotherapy—feasibility, tolerance and achieved temperatures," *International Journal of Hyperthermia*, vol. 22, no. 8, pp. 673–685, 2006.

[11] R. Hergt, R. Hiergeist, I. Hilger et al., "Maghemite nanoparticles with very high AC-losses for application in RF-magnetic hyperthermia," *Journal of Magnetism and Magnetic Materials*, vol. 270, no. 3, pp. 345–357, 2004.

[12] M. Ma, Y. Wu, J. Zhou, Y. Sun, Y. Zhang, and N. Gu, "Size dependence of specific power absorption of $Fe_3O_4$ particles in AC magnetic field," *Journal of Magnetism and Magnetic Materials*, vol. 268, no. 1-2, pp. 33–39, 2004.

[13] T. N. Brusentsova, N. A. Brusentsov, V. D. Kuznetsov, and V. N. Nikiforov, "Synthesis and investigation of magnetic properties of Gd-substituted Mn-Zn ferrite nanoparticles as a potential low-TC agent for magnetic fluid hyperthermia," *Journal of Magnetism and Magnetic Materials*, vol. 293, no. 1, pp. 298–302, 2005.

[14] G. Glöckl, R. Hergt, M. Zeisberger, S. Dutz, S. Nagel, and W. Weitschies, "The effect of field parameters, nanoparticle

properties and immobilization on the specific heating power in magnetic particle hyperthermia," *Journal of Physics*, vol. 18, no. 38, pp. S2935–S2949, 2006.

[15] J. P. Fortin, C. Wilhelm, J. Servais, C. Ménager, J.-C. Bacri, and F. Gazeau, "Size-sorted anionic iron oxide nanomagnets as colloidal mediators for magnetic hyperthermia," *Journal of the American Chemical Society*, vol. 129, no. 9, pp. 2628–2635, 2007.

[16] G. Baldi, D. Bonacchi, C. Innocenti, G. Lorenzi, and C. Sangregorio, "Cobalt ferrite nanoparticles: the control of the particle size and surface state and their effects on magnetic properties," *Journal of Magnetism and Magnetic Materials*, vol. 311, no. 1, pp. 10–16, 2007.

[17] L. Y. Zhang, H.-C. Gu, and X.-M. Wang, "Magnetite ferrofluid with high specific absorption rate for application in hyperthermia," *Journal of Magnetism and Magnetic Materials*, vol. 311, no. 1, pp. 228–233, 2007.

[18] D.-H. Kim, D. E. Nikles, D. T. Johnson, and C. S. Brazel, "Heat generation of aqueously dispersed $CoFe_2O_4$ nanoparticles as heating agents for magnetically activated drug delivery and hyperthermia," *Journal of Magnetism and Magnetic Materials*, vol. 320, no. 19, pp. 2390–2396, 2008.

[19] J.-P. Fortin, F. Gazeau, and C. Wilhelm, "Intracellular heating of living cells through Néel relaxation of magnetic nanoparticles," *European Biophysics Journal*, vol. 37, no. 2, pp. 223–228, 2008.

[20] L.-M. Lacroix, R. B. Malaki, J. Carrey et al., "Magnetic hyperthermia in single-domain monodisperse FeCo nanoparticles: evidences for Stoner-Wohlfarth behavior and large losses," *Journal of Applied Physics*, vol. 105, no. 2, Article ID 023911, 4 pages, 2009.

[21] C. L. Dennis, A. J. Jackson, J. A. Borchers et al., "Nearly complete regression of tumors via collective behavior of magnetic nanoparticles in hyperthermia," *Nanotechnology*, vol. 20, no. 39, Article ID 395103, 2009.

[22] M. Gonzales-Weimuller, M. Zeisberger, and K. M. Krishnan, "Size-dependant heating rates of iron oxide nanoparticles for magnetic fluid hyperthermia," *Journal of Magnetism and Magnetic Materials*, vol. 321, no. 13, pp. 1947–1950, 2009.

[23] R. Sharma and C. J. Chen, "Newer nanoparticles in hyperthermia treatment and thermometry," *Journal of Nanoparticle Research*, vol. 11, no. 3, pp. 671–689, 2009.

[24] E. Kita, T. Oda, T. Kayano et al., "Ferromagnetic nanoparticles for magnetic hyperthermia and thermoablation therapy," *Journal of Physics D*, vol. 43, no. 47, Article ID 474011, 2010.

[25] B. Mehdaoui, A. Meffre, L.-M. Lacroix et al., "Large specific absorption rates in the magnetic hyperthermia properties of metallic iron nanocubes," *Journal of Magnetism and Magnetic Materials*, vol. 322, no. 19, pp. L49–L52, 2010.

[26] T. Kikuchi, R. Kasuya, S. Endo et al., "Preparation of magnetite aqueous dispersion for magnetic fluid hyperthermia," *Journal of Magnetism and Magnetic Materials*, vol. 323, no. 10, pp. 1216–1222, 2011.

[27] J.-H. Lee, J.-T. Jang, J.-S. Choi et al., "Exchange-coupled magnetic nanoparticles for efficient heat induction," *Nature Nanotechnology*, vol. 6, no. 7, pp. 418–422, 2011.

[28] S.-H. Noh, W. Na, J. Jang et al., "Nanoscale magnetism control via surface and exchange anisotropy for optimized ferrimagnetic hysteresis," *Nano Letters*, vol. 12, no. 7, pp. 3716–3721, 2012.

[29] K. Nakamura, K. Ueda, A. Tomitaka et al., "Self-heating temperature and AC hysteresis of magnetic iron oxide nanoparticles and their dependence on secondary particle size," *IEEE Transactions on Magnetics*, vol. 49, no. 1, pp. 240–243, 2013.

[30] C. Martinez-Boubeta, K. Simeonidis, A. Makridis et al., "Learning from nature to improve the heat generation of iron-oxide nanoparticles for magnetic hyperthermia applications," *Scientific Reports*, vol. 3, article 1652, 2013.

[31] J. L. Dormann, D. Fiorani, and E. Tronc, "Magnetic relaxation in fine-particle systems," *Advances in Chemical Physics*, vol. 98, pp. 283–494, 1997.

[32] X. Batlle and A. Labarta, "Finite-size effects in fine particles: magnetic and transport properties," *Journal of Physics D*, vol. 35, no. 6, pp. R15–R42, 2002.

[33] H. Mamiya, *Magnetic Properties of Nanoparticles*, Yushodo, Tokyo, Japan, 2003.

[34] P. E. Jönsson, "Superparamagnetism and spin glass dynamics of interacting magnetic nanoparticle systems," *Advances in Chemical Physics*, vol. 128, pp. 191–248, 2004.

[35] P. C. Scholten, "How magnetic can a magnetic fluid be?" *Journal of Magnetism and Magnetic Materials*, vol. 39, no. 1-2, pp. 99–106, 1983.

[36] H. Mamiya, I. Nakatani, and T. Furubayashi, "Blocking and freezing of magnetic moments for iron nitride fine particle systems," *Physical Review Letters*, vol. 80, no. 1, pp. 177–180, 1998.

[37] H. Mamiya, I. Nakatani, and T. Furubayashi, "Slow dynamics for spin-glass-like phase of a ferromagnetic fine particle system," *Physical Review Letters*, vol. 82, no. 21, pp. 4332–4335, 1999.

[38] H. Mamiya, I. Nakatani, and T. Furubayashi, "Phase transitions of iron-nitride magnetic fluids," *Physical Review Letters*, vol. 84, no. 26, pp. 6106–6109, 2000.

[39] A. Wiedenmann, M. Kammel, A. Heinemann, and U. Keiderling, "Nanostructures and ordering phenomena in ferrofluids investigated using polarized small angle neutron scattering," *Journal of Physics*, vol. 18, no. 38, pp. S2713–S2736, 2006.

[40] H. Kronmüller and M. Fähnle, *Micromagnetism and the Microstructure of Ferromagnetic Solids*, Cambridge University Press, Cambridge, UK, 2003.

[41] R. Hergt, S. Dutz, and M. Röder, "Effects of size distribution on hysteresis losses of magnetic nanoparticles for hyperthermia," *Journal of Physics*, vol. 20, no. 38, Article ID 385214, 2008.

[42] R. E. Rosensweig, "Heating magnetic fluid with alternating magnetic field," *Journal of Magnetism and Magnetic Materials*, vol. 252, pp. 370–374, 2002.

[43] S. S. Papell, US Patent No. 3, 215, 1965.

[44] T. Sato, S. Higuchi, and J. Shimoiizaka, in *Proceedings of the 19th Annual Meeting of the ChemicalSociety of Japan*, 293, 1966.

[45] I. Nakatani, M. Hijikata, and K. Ozawa, "Iron-nitride magnetic fluids prepared by vapor-liquid reaction and their magnetic properties," *Journal of Magnetism and Magnetic Materials*, vol. 122, no. 1–3, pp. 10–14, 1993.

[46] S. Sun, C. B. Murray, D. Weller, L. Folks, and A. Moser, "Monodisperse FePt nanoparticles and ferromagnetic FePt nanocrystal superlattices," *Science*, vol. 287, no. 5460, pp. 1989–1992, 2000.

[47] X.-M. Lin and A. C. S. Samia, "Synthesis, assembly and physical properties of magnetic nanoparticles," *Journal of Magnetism and Magnetic Materials*, vol. 305, no. 1, pp. 100–109, 2006.

[48] A. H. Lu, E. L. Salabas, and F. Schüth, "Magnetic nanoparticles: synthesis, protection, functionalization, and application," *Angewandte Chemie*, vol. 46, no. 8, pp. 1222–1244, 2007.

[49] L. Li, Y. Yang, J. Ding, and J. Xue, "Synthesis of magnetite nanooctahedra and their magnetic field-induced two-/three-dimensional superstructure," *Chemistry of Materials*, vol. 22, no. 10, pp. 3183–3191, 2010.

[50] J. L. C. Huaman, S. Fukao, K. Shinoda, and B. Jeyadevan, "Novel standing Ni-Pt alloy nanocubes," *CrystEngComm*, vol. 13, no. 10, pp. 3364–3369, 2011.

[51] Y. Li, Q. Zhang, A. V. Nurmikko, and S. Sun, "Enhanced magnetooptical response in dumbbell-like Ag-CoFe$_2$O$_4$ nanoparticle pairs," *Nano Letters*, vol. 5, no. 9, pp. 1689–1692, 2005.

[52] The International Commission on Non-Ionizing Radiation Protection, "Guide-lines for limiting exposure to time-varying electric, magnetic, and electro-magnetic fields (up to 300 GHz)," *Health Physics*, vol. 74, no. 4, pp. 494–522, 1998.

[53] E. Lima Jr., E. de Biasi, and M. V. Mansilla, "Heat generation in agglomerated ferrite nanoparticles in an alternating magnetic field," *Journal of Physics D*, vol. 46, no. 4, Article ID 045002, 2013.

[54] S. M. Morgan and R. H. Victora, "Use of square waves incident on magnetic nanoparticles to induce magnetic hyperthermia for therapeutic cancer treatment," *Applied Physics Letters*, vol. 97, no. 9, Article ID 093705, 2010.

[55] E. L. Verde, G. T. Landi, and M. S. Carriao, "Field dependent transition to the non-linear regime in magnetic hyperthermia experiments: comparison between maghemite, copper, zinc, nickel and cobalt ferrite nanoparticles of similar sizes," *AIP Advances*, vol. 2, no. 3, Article ID 032120, 23 pages, 2012.

[56] G. T. Landi and A. F. Bakuzis, "On the energy conversion efficiency in magnetic hyperthermia applications: a new perspective to analyze the departure from the linear regime," *Journal of Applied Physics*, vol. 111, no. 8, Article ID 083915, 2012.

[57] N. A. Usov, S. A. Gudoshnikov, and O. N. Serebryakova, "Properties of dense assemblies of magnetic nanoparticles promising for application in biomedicine," *Journal of Superconductivity and Novel Magnetism*, vol. 26, no. 4, pp. 1079–1083, 2013.

[58] J. Carrey, B. Mehdaoui, and M. Respaud, "Simple models for dynamic hysteresis loop calculations of magnetic single-domain nanoparticles: application to magnetic hyperthermia optimization," *Journal of Applied Physics*, vol. 109, no. 8, Article ID 083921, 17 pages, 2011.

[59] Z. P. Mendoza, G. A. Pasquevich, and S. J. Stewart, "Structural and magnetic study of zinc-doped magnetite nanoparticles and ferrofluids for hyperthermia applications," *Journal of Physics D*, vol. 46, no. 12, Article ID 125006, 2013.

[60] W. F. Brown Jr., "Thermal fluctuations of a single-domain particle," *Physical Review*, vol. 130, no. 5, pp. 1677–1686, 1963.

[61] H. Mamiya and B. Jeyadevan, "Optimal design of nanomagnets for targeted hyperthermia," *Journal of Magnetism and Magnetic Materials*, vol. 323, no. 10, pp. 1417–1422, 2011.

[62] D. B. Reeves and J. B. Weaver, "Simulations of magnetic nanoparticle Brownian motion," *Journal of Applied Physics*, vol. 112, no. 12, Article ID 124311, 6 pages, 2012.

[63] T. Yoshida and K. Enpuku, "Simulation and quantitative clarification of AC susceptibility of magnetic fluid in nonlinear Brownian relaxation region," *Japanese Journal of Applied Physics*, vol. 48, Article ID 127002, 7 pages, 2009.

[64] H. Mamiya and B. Jeyadevan, "Hyperthermic effects of dissipative structures of magnetic nanoparticles in large alternating magnetic fields," *Scientific Reports*, vol. 1, article 157, 2011.

[65] N. A. Usov and B. Ya. Liubimov, "Dynamics of magnetic nanoparticle in a viscous liquid: application to magnetic nanoparticle hyperthermia," *Journal of Applied Physics*, vol. 112, no. 2, Article ID 023901, 11 pages, 2012.

[66] H. Mamiya and B. Jeyadevan, "Formation of non-equilibrium magnetic nanoparticle structures in a large alternating magnetic field and their influence on magnetic hyperthermia treatment,"

*IEEE Transactions on Magnetics*, vol. 48, no. 11, pp. 3258–3262, 2012.

[67] H. Mamiya and B. Jeyadevan, "Magnetic hysteresis loop in a superparamagneticstate," in press. *IEEE Transactions on Magnetics*.

[68] W. Andrä, C. G. D'Ambly, R. Hergt, I. Hilger, and W. A. Kaiser, "Temperature distribution as function of time around a small spherical heat source of local magnetic hyperthermia," *Journal of Magnetism and Magnetic Materials*, vol. 194, no. 1, pp. 197–203, 1999.

[69] C. W. Song, "Effect of local hyperthermia on blood flow and microenvironment: a review," *Cancer Research*, vol. 44, no. 10, supplement, pp. 4721s–4730s, 1984.

[70] T. Hasegawa, R. Kudaka, K. Saito et al., *Bulletin of Suzuka University of Medical Science*, vol. 11, pp. 58–64, 2004.

[71] J. Bohnert and O. Dössel, "Simulations of temperature increase due to time varying magnetic fields up to 100 kHz," in *Proceedings of the 5th European Conference of the International Federation for Medical and Biological Engineering*, vol. 37 of *IFMBE Proceedings*, pp. 303–306, 2012.

[72] H. Mamiya, "Magnetic response of nanoparticles to AC magnetic fields and targeted thermotherapy," *Materials Integration*, vol. 25, pp. 11–23, 2012.

[73] T. Kobayashi, "Cancer hyperthermia using magnetic nanoparticles," *Biotechnology Journal*, vol. 6, no. 11, pp. 1342–1347, 2011.

[74] B. Thiesen and A. Jordan, "Clinical applications of magnetic nanoparticles for hyperthermia," *International Journal of Hyperthermia*, vol. 24, no. 6, pp. 467–474, 2008.

*Research Article*

# Bentonite/Iron Oxide Composites: Preparation and Characterization by Hyperfine Methods

**Petr Křišťan,[1] Vojtěch Chlan,[1] Helena Štěpánková,[1] Richard Řezníček,[1] Karel Kouřil,[1] Josef Štěpánek,[1] Kateřina Poláková,[2] Vít Procházka,[2] Jan Čuda,[2] and Ivo Medřík[2]**

[1] *Faculty of Mathematics and Physics, Charles University in Prague, V Holešovičkách 2, 18000 Prague 8, Czech Republic*
[2] *Palacky University, Šlechtitelů 11, 783 71 Olomouc, Czech Republic*

Correspondence should be addressed to Helena Štěpánková; helena.stepankova@mff.cuni.cz

Bentonite/iron oxide system is prepared by isothermal calcination of powder composed of bentonite clay and precursor containing ferric acetate. This preparation technique enables one to get the composite material directly, that is, iron oxide particles embedded in a bentonite matrix. Calcination temperature $T_{calc}$ is varied from 320°C to 700°C. The resulting series of samples is characterized by local methods based on hyperfine interactions: $^{57}$Fe nuclear magnetic resonance (NMR) and the Mössbauer spectroscopy. The results show that the phase composition changes significantly in dependence on calcination temperature. The amount of maghemite phase rapidly increases up to $T_{calc} = 420$°C and decreases abruptly for $T_{calc}$ higher than 460°C.

## 1. Introduction

Magnetic or superparamagnetic iron oxide particles of submicron and nanoscale dimensions are successfully applied in biomedical and bioengineering applications [1–4]. They are functional, for example, in magnetic resonance imaging (MRI) as contrast agents for diagnostic purposes, for location and tracking of labeled cell or in drug delivery studies. Maghemite ($\gamma$-Fe$_2$O$_3$) attached to the surface of the bentonite clay forms an efficient negative oral contrast agent for MRI diagnostics in gastroenterology [5] or should be used, for example, for magnetic separation of composite from the medium after sorption processes [6]. In this paper, we report on a bentonite/iron oxide sample series obtained by isothermal calcination of powder composed of bentonite and ferric acetate. The proposed technique enables to prepare directly the composite material of iron oxide particles embedded in a bentonite matrix preventing the particles from aggregation.

The prepared bentonite/iron oxide samples are characterized by two local methods based on hyperfine interactions: $^{57}$Fe nuclear magnetic resonance (NMR) spectroscopy and the Mössbauer spectroscopy (MS). Both methods are sensitive to the iron ionic state and environments; however, they differ in sensitivity, resolution, evaluated parameters, accuracy, and certainly in experimental demands and laboriousness. The Mössbauer measurements become a standard method for monitoring of preparation processes of submicron and nanoscale maghemite and related iron oxides; see, for example, [7–9]. On the other hand, maghemite itself, though it is used in MRI, has been studied by NMR [10–14] only rarely.

## 2. Materials and Methods

*2.1. Synthesis.* Powder composite samples were prepared by thermal decomposition of iron (II), (CH$_3$CO$_2$)$_2$Fe (Sigma Aldrich) in air. 1000 mg of (CH$_3$CO$_2$)$_2$Fe was mixed with 2000 mg of bentonite (Tamda-Fagron), and the mixture was homogenized in an agate mortar and then calcined for 1 hour at isothermal conditions at various temperatures $T_{calc}$ from 320°C to 700°C. The calcinations were done in a porcelain crucible inside a muffle furnace LM 112.27 (Linn High Therm GmbH).

*2.2. The Mössbauer Spectroscopy.* The room temperature $^{57}$Fe Mössbauer spectra were collected in a zero external magnetic
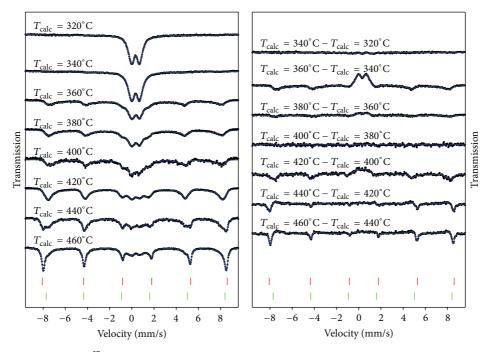
FIGURE 1: Left: the room temperature $^{57}$Fe Mössbauer spectra measured in zero external magnetic field, experiment (symbols), and fit (lines). Right: differences between the successive spectra. In both parts of the figure, positions of spectral lines in sextets of well-crystallized hematite and maghemite calculated from hyperfine parameters in [7] are marked by short vertical lines (red lines, hematite; green lines, maghemite).

field in the range $(-10, +10)$ mm/s using a constant acceleration spectrometer with a $^{57}$Co (Rh) source. The velocity scale was calibrated relative to $^{57}$Fe in $\alpha$-Fe. The spectra were analyzed by the CONUSS software package [15] and in parallel by our purpose-made software.

*2.3. Nuclear Magnetic Resonance.* The $^{57}$Fe NMR spectra of all samples were recorded in a zero external field at 4.2 K using the pulse Bruker Avance spectrometer console. The measured sample was fixed in the copper coil of a tuned parallel resonant circuit and submerged in liquid helium. Additional NMR measurements of selected samples were done at room temperature.

A frequency-swept regime was employed with a step of 100 kHz. The following parameters were used in a spin echo sequence: pulse duration of $2\,\mu$s and $4\,\mu$s for the first and second pulse, respectively, time delay $23\,\mu$s, repetition time ~10 ms, and optimal amplitude of the radiofrequency field was found. In order to reach a sufficient signal/noise $(S/N)$ ratio, 4096 scans were acquired at each frequency. To further increase $S/N$ and verify the impact of nuclear spin-spin relaxation rate on spectral shape, the Carr-Purcell-Meiboom-Gill (CPMG) multiecho pulse sequence [16] was applied where all generated echoes in the train were recorded, and coherent summation of selected echoes was done.

Time domain data obtained at each excitation frequency were transformed to frequency domain using fast Fourier transform (FFT), and the final spectrum was plotted as modules of Fourier transform at particular excitation frequencies.

## 3. Results and Discussion

The room temperature Mössbauer spectra of bentonite/iron oxide samples prepared by an annealing process at calcination temperatures ($T_{calc}$) 320, 340, 360, 380, 400, 420, 440, and 460°C are shown in Figure 1 together with the differences between the successive spectra in the series. Three spectral components can be resolved in the spectral set: a doublet and two sextets. The line positions of the sextets correspond to maghemite ($\gamma$-Fe$_2$O$_3$) and hematite ($\alpha$-Fe$_2$O$_3$) [7].

Figure 1 provides a qualitative view of the effect of the calcination temperature. First two samples (calcination at 320 and 340°C) exhibit paramagnetic behavior because a doublet component, representing according to its hyperfine parameters [17] amorphous Fe$_2$O$_3$, is dominant in their spectra. The other spectra bring out the samples to be a mixture of paramagnetic and magnetically ordered materials. It is evident that the doublet intensity decreases while the maghemite and then the hematite phases are formed when $T_{calc}$ is increased.

Quantitative determination of the phase composition is complicated by the overlap of the spectral components, namely, of the doublet and the maghemite sextet which can be broadened by a hyperfine field distribution. In order to get proper quantitative evaluation of sample composition in dependence on $T_{calc}$, a suitable fitting model for spectral analysis is needed. To minimize the influence of systematic errors of particular models, we therefore employed three different decomposition procedures. The first and the second
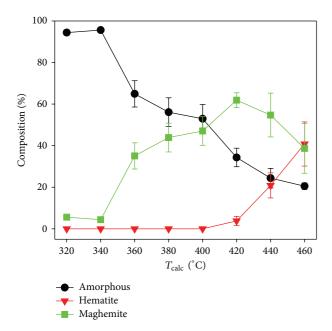
FIGURE 2: Concentration of maghemite, amorphous $Fe_2O_3$, and hematite determined from the Mössbauer spectra.

approaches utilized the CONUSS package, while the third utilized our purpose-made software.

In the first model, the doublet was reconstructed by a distribution of electric quadrupole interaction (quadrupole splitting) corresponding to amorphous $Fe_2O_3$, paramagnetic at the given temperature above the Curie point [17]. The maghemite phase formed during the annealing was associated with a spectral component featuring magnetic dipole interactions with Gaussian distribution of hyperfine magnetic field and very low or zero quadrupole splitting. For the samples prepared at temperature $T_{calc} = 420°C$ and higher, the third spectral component was added which was identified according to its hyperfine parameters (magnetic splitting, isomer shift, and quadrupole splitting) as hematite.

The spectra with magnetite component exhibit asymmetric shape of sextet lines which can be easily seen for samples with $T_{calc} = 420$ and $440°C$.

This behavior is typically determined by the presence of $^{57}Fe$ nuclei in significantly lower magnetic hyperfine field and assigned to maghemite with not fully developed magnetic structure. The second model then accounted for a broad maghemite sextet, and for this purpose, the first model was amended by fourth component characterized by a large asymmetric distribution that gradually decreased at the side of low hyperfine fields.

The third analysis of the Mössbauer spectra was performed via decomposition into a set of a doublet and two sextets by using a least-square fit. The line shapes of the doublet and the hematite sextet were approximated by the Pearson VII functions. The maghemite spectrum was modelled as a superposition of contributions from $^{57}Fe$ nuclei in the tetrahedral (A) and octahedral (B) sites of spinel structure (with 3 : 5 intensity ratio and 0.14 mm/s difference of isomer
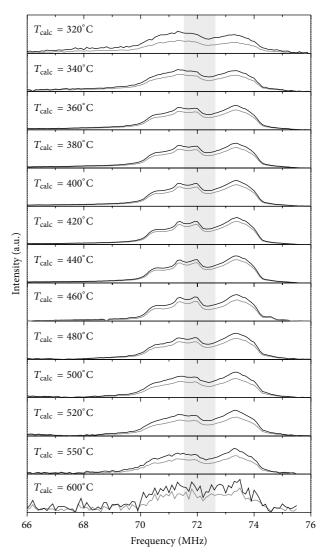


FIGURE 3: NMR spectra of $^{57}Fe$ (gyromagnetic ratio 1.38 MHz/T) in maghemite phase measured at 4.2 K in zero external magnetic field. Gray spectral area marks superposed signals from $^{57}Fe$ in A and B sites; left parts of the spectra belong to A sites, right part to B sites. (Black lines, the spectra evaluated from echoes 1–10 and normalized to equal areas; grey lines, spectra from echoes 1–21.) Maghemite signals of samples with $T_{calc} = 600°C$ and $700°C$ were very weak due to negligible content of the phase; the latter spectrum is not shown.

shifts [7]). The fit provided the hyperfine field distributions approximated by a sum of two Gaussian curves with different magnitudes, and the position of the lesser one corresponded to a hyperfine field lowered from 10 to 17% in respect to the main curve. The fitting procedure was primarily applied to the first and the last spectrum of the series and to the differences between subsequent spectra. The decompositions of the original spectra (except the first and the last one) were calculated afterwards. Results of this fit are shown in Figure 1.

Results of the three analyses are slightly different but show similar dependence of the composition on the calcination temperature. The average values of the amorphous, maghemite, and hematite phases amounts are plotted in
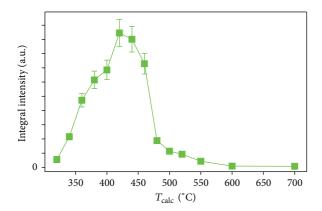
FIGURE 4: Relative amount of maghemite phase in sample series evaluated from NMR in dependence on calcination temperature.

Figure 2 with error bars corresponding to a standard deviation.

Our NMR measurements focused on the spectral region of $^{57}$Fe resonance in maghemite phase and monitored spectral shape and intensity in dependence on $T_{calc}$ from 320°C to 700°C. The spectra recorded at 4.2 K are shown in Figure 3. The spectra evaluated from echoes 1–10 in comparison with those from echoes 1–21 help to estimate the impact of spin-spin relaxation on the spectral shapes and intensities. The spectral shape is almost independent of the number of considered echoes; the nuclear spin-spin relaxation is slowest for $T_{calc}$ 400–440°C.

It is known [10] that subspectra of $^{57}$Fe in tetrahedral (A) and octahedral (B) sites in zero external field are partially overlapped, which is marked in Figure 3. Maximal intensity of B line is at 73.4 MHz, and the spectrum of A sites exhibits characteristic features (with three local maxima at 70.50, 71.35, and 71.95 MHz) which become well resolved for $T_{calc}$ from 400 to 460°C. This effect is most likely connected with higher degree of atomic/vacancy ordering in maghemite spinel structure. The maghemite signal intensity rapidly increases up to $T_{calc}$ = 420°C, and then, its abrupt decrease appears for $T_{calc}$ above 460°C. Evaluation of integral intensities of NMR spectra allowed us to compare the relative amounts of maghemite phase within the sample series. The obtained dependence is shown in Figure 4.

For $T_{calc}$ = 700°C, also $^{57}$Fe NMR of hematite was measured at 4.2 K. The maximum of hematite spectrum appears at 73.5 MHz, in agreement with [18]. In this sample, the signals of hematite and maghemite were of comparable intensities. Separation of the signals was achieved due to difference in enhancement factors which resulted in different optimal excitation conditions: radiofrequency field needed for hematite was approximately an order stronger than that for maghemite (using the same pulse lengths). The hematite signal at 4.2 K in samples with higher content of maghemite (for lower $T_{calc}$) was most likely buried in strong maghemite contribution. However, hematite signals were detected at room temperature at ~71.1 MHz, and the spectral linewidths were of ~0.2 MHz.

## 4. Conclusions

Composite bentonite/iron oxide samples were prepared by isothermal calcination of bentonite and precursor containing ferric acetate and were characterized by $^{57}$Fe NMR and the Mössbauer spectroscopy. The dependence of the maghemite content on the calcination temperature monitored by both methods is in a reasonable agreement and shows maximum around $T_{calc}$ = 420°C. Contents of other iron oxide phases are determined from the Mössbauer spectra, while NMR yields more details of hyperfine magnetic field distribution in well-ordered magnetite phase.

## Acknowledgment

## References

[1] A. K. Gupta and M. Gupta, "Synthesis and surface engineering of iron oxide nanoparticles for biomedical applications," *Biomaterials*, vol. 26, no. 18, pp. 3995–4021, 2005.

[2] S. Purushotham and R. V. Ramanujan, "Modeling the performance of magnetic nanoparticles in multimodal cancer therapy," *Journal of Applied Physics*, vol. 107, no. 11, Article ID 114701, 2010.

[3] S. Mornet, S. Vasseur, F. Grasset, and E. Duguet, "Magnetic nanoparticle design for medical diagnosis and therapy," *Journal of Materials Chemistry*, vol. 14, no. 14, pp. 2161–2175, 2004.

[4] Q. A. Pankhurst, J. Connolly, S. K. Jones, and J. Dobson, "Applications of magnetic nanoparticles in biomedicine," *Journal of Physics D*, vol. 36, no. 13, pp. R167–R181, 2003.

[5] K. Kluchová, R. Zbořil, J. Tucek et al., "Superparamagnetic maghemite nanoparticles from solid-state synthesis—their functionalization towards peroral MRI contrast agent and magnetic carrier for trypsin immobilization," *Biomaterials*, vol. 30, no. 15, pp. 2855–2863, 2009.

[6] Z. Orolinová and A. Mockovčiaková, "Structural study of bentonite/iron oxide composites," *Materials Chemistry and Physics*, vol. 114, pp. 956–961, 2009.

[7] R. Zboril, M. Mashlan, and D. Petridis, "Iron(III) oxides from thermal processes-synthesis, structural and magnetic properties, Mössbauer spectroscopy characterization, and applications," *Chemistry of Materials*, vol. 14, no. 3, pp. 969–982, 2002.

[8] J. Tuček, R. Zbořil, and D. Petridis, "Maghemite nanoparticles by view of Mössbauer spectroscopy," *Journal of Nanoscience and Nanotechnology*, vol. 6, no. 4, pp. 926–947, 2006.

[9] P. Tartaj, M. del Puerto Morales, S. Veintemillas-Verdaguer, T. González-Carreño, and C. J. Serna, "The preparation of magnetic nanoparticles for applications in biomedicine," *Journal of Physics D*, vol. 36, no. 13, pp. R182–R197, 2003.

[10] S.-J. Lee and S. Lee, "The spin structure of maghemite investigated by $^{57}$Fe NMR," *New Journal of Physics*, vol. 8, article 98, 2006.

[11] T. J. Bastow, A. Trinchi, M. R. Hill, R. Harris, and T. H. Muster, "Vacancy ordering in $\gamma$-Fe$_2$O$_3$ nanocrystals observed by $^{57}$Fe NMR," *Journal of Magnetism and Magnetic Materials*, vol. 321, no. 17, pp. 2677–2681, 2009.

[12] T. J. Bastow and A. Trinchi, "NMR analysis of ferromagnets: Fe oxides," *Solid State Nuclear Magnetic Resonance*, vol. 35, no. 1, pp. 25–31, 2009.

[13] T. J. Daou, J. M. Greneche, S. J. Lee et al., "Spin canting of maghemite studied by NMR and in-field Mössbauer spectrometry," *The Journal of Physical Chemistry C*, vol. 114, pp. 8794–8799, 2010.

[14] M. Fardis, A. P. Douvalis, D. Tsitrouli et al., "Structural, static and dynamic magnetic properties of dextran coated $\gamma$-Fe$_2$O$_3$ nanoparticles studied by $^{57}$Fe NMR, Mössbauer, TEM and magnetization measurements," *Journal of Physics Condensed Matter*, vol. 24, no. 15, Article ID 156001, 2012.

[15] W. Sturhahn and E. Gerdau, "Evaluation of time-differential measurements of nuclear-resonance scattering of x rays," *Physical Review B*, vol. 49, no. 14, pp. 9285–9294, 1994.

[16] S. Meiboom and D. Gill, "Modified spin-echo method for measuring nuclear relaxation times," *Review of Scientific Instruments*, vol. 29, no. 8, pp. 688–691, 1958.

[17] L. Machala, R. Zbořil, and A. Gedanken, "Amorphous iron(III) oxide—a review," *Journal of Physical Chemistry B*, vol. 111, no. 16, pp. 4003–4018, 2007.

[18] S.-J. Lee, H. Jung, S. Lee, and J. Dho, "Superparamagnetic behaviour of reentrant weak-ferromagnetic phase in haematite crystal at low temperatures," *New Journal of Physics*, vol. 11, Article ID 023020, 2009.

*Review Article*

# Spin Structures in Magnetic Nanoparticles

## Steen Mørup,[1] Erik Brok,[1,2] and Cathrine Frandsen[1]

[1] *Department of Physics, Technical University of Denmark, 2800 Kongens Lyngby, Denmark*
[2] *Center for Electron Nanoscopy, Technical University of Denmark, 2800 Kongens Lyngby, Denmark*

Correspondence should be addressed to Cathrine Frandsen; fraca@fysik.dtu.dk

Spin structures in nanoparticles of ferrimagnetic materials may deviate locally in a nontrivial way from ideal collinear spin structures. For instance, magnetic frustration due to the reduced numbers of magnetic neighbors at the particle surface or around defects in the interior can lead to spin canting and hence a reduced magnetization. Moreover, relaxation between almost degenerate canted spin states can lead to anomalous temperature dependences of the magnetization at low temperatures. In ensembles of nanoparticles, interparticle exchange interactions can also result in spin reorientation. Here, we give a short review of anomalous spin structures in nanoparticles.

## 1. Introduction

The magnetic properties of nanoparticles differ in many respects from those of the corresponding bulk materials [1]. In very small magnetic particles, the magnetization direction is not fixed but fluctuates at finite temperatures, and the magnetization may spontaneously be reversed (superparamagnetic relaxation) above the blocking temperature [2, 3]. At low temperatures, the spin wave excitations are dominated by the uniform mode ($q = 0$ spin waves), resulting in a linear temperature dependence of the magnetization in contrast to the Bloch $T^{3/2}$ law valid for bulk materials [4]. In several studies, it has been found that the saturation magnetization of nanoparticles of ferrimagnetic materials is smaller than the bulk value. This can in many cases be explained by spin canting, that is, noncollinear spin structures. The reduced number of magnetic neighbor ions around surface atoms can lead to magnetic frustration, which results in canted spin structures in materials with otherwise collinear spin structures [5, 6]. Near the surface, the low local symmetry can result in a large contribution to the local magnetic anisotropy, which also can influence the spin orientations. Both in nanoparticles and in bulk materials, defects in the interior, such as diamagnetic substitution or cation vacancies, can also lead to noncollinearity [7]. In materials with spin canting there may be different canted states that are separated by

very low energy barriers [7]. Therefore, magnetic fluctuations can take place at very low temperatures. Freezing of the spins can result in an anomalous temperature dependence of the magnetization at low temperatures. Moreover, exchange interaction between surface atoms of neighboring particles can have a profound influence on the magnetic properties because this can affect both the superparamagnetic relaxation [8–10] and the spin structure [9, 11]. For many applications of magnetic nanoparticles, a large saturation magnetization is desirable, and it is therefore important to control and minimize spin canting. In this paper, we present a short review on spin structures in magnetic nanoparticles.

## 2. Theoretical Models for Spin Canting

Canted spin structures at surfaces and around defects in the interior of a material are in general very complex, and analytical calculations of the magnetic properties may therefore not be feasible, but the spin structures can be elucidated by use of computer simulations. Kodama et al. [12] have performed computer simulations of the spin structure of 2.5 nm nanoparticles of the inverse spinel $NiFe_2O_4$. In the simulations, the magnetic anisotropy was neglected and it was assumed that the interior of the particles was defect-free. Therefore, there is only spin canting near the surface. Figure 1 shows a calculated spin structure for a (111) plane
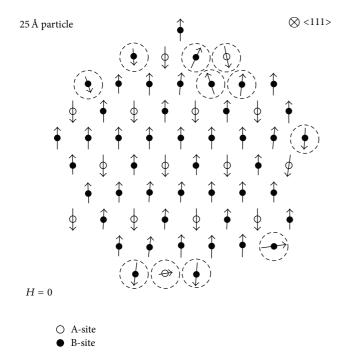
FIGURE 1: Calculated spin structures for a (111) cross-section of a 2.5 nm NiFe$_2$O$_4$ particle. Reproduced with permission from Kodama et al. [12].
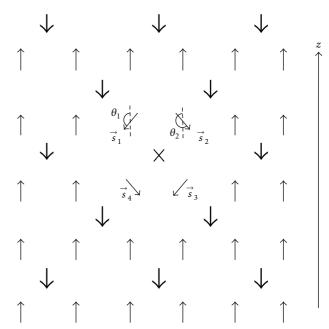


FIGURE 2: Schematic illustration of a canted two-dimensional spin structure. The bold arrows correspond to A-site spins and the other arrows correspond to B-site spins. The cross represents a missing A-site spin. Reproduced with permission from Jacobsen et al. [14].

of a 2.5 nm NiFe$_2$O$_4$ particle. Highly misoriented spins are indicated by dashed circles. It is noteworthy that some of the surface spins are completely reversed. The simulations also showed that different canted states commonly are separated by very low energy barriers. If surface anisotropy is included in the model, more surface spins will be strongly canted [13].

In very simple cases, analytical calculations of spin structures around defects and at surfaces can be performed. Although simple, these calculations show at least qualitatively that the magnetization may increase or decrease in an anomalous way at low temperatures. Figure 2 shows a simple two-dimensional canted spin structure, which allows obtaining analytical solutions for the spin directions and the temperature dependence of the magnetization by use of a classical model [7, 14]. In the model, spins at A-sites and B-sites are antiparallel in the defect-free structure. The bold arrows in Figure 2 represent A-site spins and the remaining arrows represent B-site spins. The cross represents a missing A-site spin, which can give rise to magnetic frustration and canting of neighboring B-site spins. In the calculations, the magnetic anisotropy and canting of next nearest spins are neglected. For symmetry reasons, the angles between the spins and the $z$-direction are assumed to be pairwise identical. The magnetic energy can then be written [7, 14]:

$$E\left(\theta_1, \theta_2\right) = a\left(\cos\theta_1 + \cos\theta_2\right) + b\cos\left(\theta_1 - \theta_2\right), \quad (1)$$

where $\theta_1$ and $\theta_2$ are defined in the figure, $a = 4\lambda_{BB} - 2\lambda_{AB} + 2\lambda_L - 2\mu B$, and $b = 4\lambda_{BB}$. Here, $\lambda_{BB}$ is the exchange parameter for nearest neighbor B-B coupling, $\lambda_{AB}$ is the exchange parameter for nearest neighbor A-B coupling, and $\lambda_L$ is the exchange parameter for the exchange interaction between a

B-site ion and all more distant ions. $\mu$ is the magnetic moment of a B-site ion, and $B$ is the applied magnetic field, defining the $z$-direction.

By differentiating (1), one can find the spin orientations, which give minimum energy. Calculations have been performed for $b/k_B = 200$ K ($k_B$ is Boltzmann's constant) and values of $a/b$ between 1.1 and 1.9 [14]. Energy minima are found for $\sin\theta_1 = -\sin\theta_2$ and $\cos\theta_1 = \cos\theta_2 = -a/2b$ with energy $E_{\min} = -b - a^2/2b$. They are separated by maxima at $\theta_1 = \theta_2 = 180°$ with $E(180°, 180°) = -2a + b$. A more comprehensive discussion of the energy maxima and minima in simple canted spin structures is given in [7].

For arbitrary values of $\theta_1$, the values of $\theta_2$, which minimize the energy, are given by [14]

$$tg\theta_2 = \frac{b\sin\theta_1}{a + b\cos\theta_1}, \quad (2)$$

and the magnetic energy as a function of the angle $\theta_1$ is given by [14]

$$E\left(\theta_1\right) = a\cos\theta_1 - \sqrt{a^2 + b^2 + 2ab\cos\theta_1}. \quad (3)$$

Figure 3 shows the magnetic energy as a function of $\theta_1$ for values of $a/b$ between 1.1 and 1.9. At very low temperatures, the system is found in an energy minimum, but at higher temperatures, the spin may perform transverse relaxation, that is, fluctuations of the spin directions across the energy barrier at $\theta_1 = 180°$. For $1.7 \leq a/b < 2.0$, the height of the energy barrier is less than 10 K, and transverse relaxation may therefore take place at very low temperatures.

In general, the average value of the $z$ component of the magnetic moment is given by $\langle M^z(T)\rangle = 2\mu\langle\cos\theta_1 + \cos\theta_2\rangle$,
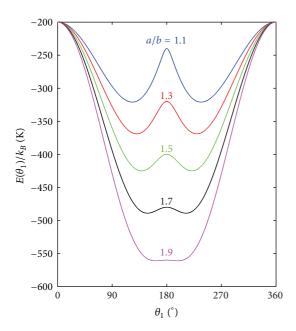
FIGURE 3: The energy of the canted spin structure, shown in **Figure 2**, as a function of the angle $\theta_1$ for the indicated values of $a/b$. The calculations were carried out using (3) with $b/k_B = 200$ K. Reproduced with permission from Jacobsen et al. [14].
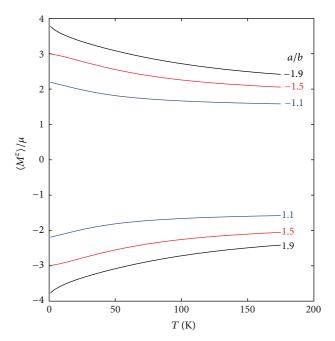


FIGURE 4: Temperature dependence of the thermal average of the canted spin structure, shown in **Figure 2**. The calculations were carried out using Boltzmann statistics for $b/k_B = 200$ K and the indicated values of $a/b$. Reproduced with permission from Jacobsen et al. [14].

where $\mu$ is the magnetic moment of a single atom. The temperature dependence of $\langle M^z(T) \rangle$ for values of $a/b$ between 1.1 and 1.9 and between $-1.1$ and $-1.9$ calculated by use of Boltzmann statistics is shown in **Figure 4**. At low temperatures, the thermal average of the magnetic moment increases or decreases rapidly with decreasing temperature. Several experimental studies of ferrimagnetic nanoparticles have shown anomalous temperature dependencies of the magnetization at low temperatures that are in accordance with this model [12, 17–24]. A quantum mechanical calculation gives results that are qualitatively similar to those of the classical model [14].

## 3. Experimental Studies of Spin Canting

Mössbauer spectroscopy in large applied magnetic fields is a very useful method to investigate spin canting in ferrimagnetic materials [5, 6]. The magnetic hyperfine splitting in Mössbauer spectra is proportional to the total magnetic field at the nucleus, $B_{\text{tot}}$, which has contributions from the hyperfine field, $B_{\text{hf}}$, and the applied field, $B_{\text{app}}$, and can be found from the relationship

$$B_{\text{hf}}^2 = B_{\text{tot}}^2 + B_{\text{app}}^2 - 2B_{\text{tot}}B_{\text{app}} \cos \theta, \qquad (4)$$

where $\theta$ is the angle between the direction of the total magnetic field at the nucleus and the gamma ray direction. The relative areas of the six lines of a $^{57}$Fe Mössbauer spectrum of a magnetic material depend on the angle $\theta$ as the relative areas are given by $3:p:1:1:p:3$, where

$$p = \frac{4 \sin^2 \theta}{2 - \sin^2 \theta}. \qquad (5)$$

In polycrystalline ferrimagnetic materials in zero applied field with random orientation of the crystallites, the orientations of the sublattice magnetization directions are random, and the relative areas are then $3:2:1:1:2:3$. If a large magnetic field is applied parallel to the gamma ray direction, the sublattice magnetization directions of a collinear ferrimagnetic material will be parallel and antiparallel to this direction, resulting in zero intensity of lines 2 and 5. However, in nanoparticles of ferrimagnetic materials, these two lines usually have nonzero intensity because of spin canting. In several publications, it has been suggested that this spin canting is located at the surface, because the reduced number of magnetic neighbor ions at the surface can result in magnetic frustration. However, in other studies it has been found that the canting does not vary with particle size in a regular way [25–27]. This strongly suggests that canting is not only a surface effect but also commonly occurs around defects in the interior of the particles [25–27].

As an example, **Figure 5** shows a Mössbauer spectrum of magnetic Dynabeads, consisting of $1\,\mu$m porous polymer beads containing 7.7 nm maghemite ($\gamma$-Fe$_2$O$_3$) particles in the pores. Such beads are used, for example, for preparation and handling of biological materials, and a large saturation magnetization of the maghemite particles is essential for the performance. The saturation magnetization of the maghemite particles in the beads was 336 kA m$^{-1}$ [28], which is about 10% less than the bulk value. The Mössbauer spectrum, shown in **Figure 5**, was obtained at 6.0 K with a magnetic field of 6.0 T applied parallel to the gamma ray direction. The spectrum
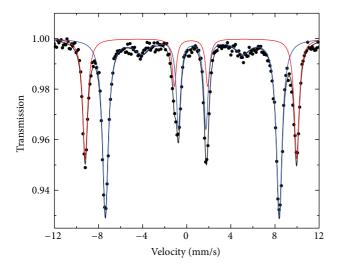
FIGURE 5: Mössbauer spectrum of $1\,\mu$m magnetic Dynabeads, containing 7 nm maghemite ($\gamma$-Fe$_2$O$_3$) nanoparticles. The spectrum was obtained at 6 K with a magnetic field of 6 T applied parallel to the gamma ray direction. The red and blue fit lines represent Fe$^{3+}$ in A- and B-sites, respectively.

was fitted with two sextets, corresponding to iron in the A-sites (red fit lines) with a total field of 59.4 T and B-sites (blue fit lines) with a total field of 48.9 T. The intensity of lines 2 and 5 of the A-site component is negligible, whereas the relative areas of lines 2 and 5 for the B-site component were $p \approx 0.55$, corresponding to an average canting angle, $\theta \approx 29°$ for the B-site spins. These results show that there is essentially no canting in A-sites but some canting in B-sites. The canting can affect all B-site ions or be restricted to a fraction of B-site spins with large canting angles, but the data can explain at least qualitatively the reduced value of the saturation magnetization compared to the bulk value.

A study of the temperature dependence of the spin structure has been made for 7 nm maghemite particles [15]. The Mössbauer spectra of the sample, shown in Figure 6, were obtained at the indicated temperatures with a magnetic field of 4 T applied parallel to the gamma ray direction. At low temperatures, lines 2 and 5 have nonzero intensity indicating the presence of spin canting. The best fits of the spectra were obtained with three sextets, two of which had zero intensity of lines 2 and 5, corresponding to iron in the tetrahedral A- and the octahedral B-sites of the spinel structure with a perfect collinear ferrimagnetic structure. The third sextet with nonzero intensity of lines 2 and 5 had an isomer shift indicating that it was mainly due to iron in the octahedral B-sites. Thus, the data indicate that the canting only affects a fraction of the B-site spins, whereas the remaining B-site spins and the A-site spins are essentially not affected by the canting. Sextets 1 and 2 had relatively narrow lines at all temperatures, but sextet 3 showed a substantial line broadening and a decreasing relative area of lines 2 and 5 with increasing temperature. Similar results have been found in studies of 2.7 nm and 4.6 nm maghemite particles [29]. This temperature dependence can be explained by transverse relaxation between canted states, characterized by canting
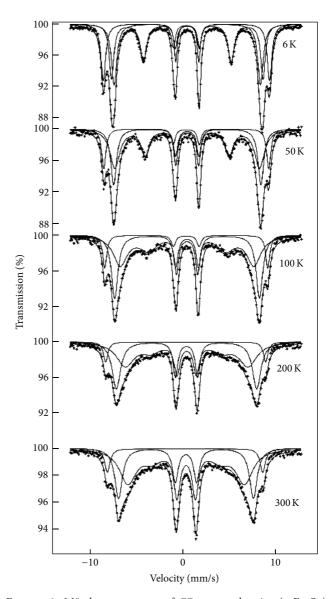


FIGURE 6: Mössbauer spectra of 7.7 nm maghemite ($\gamma$-Fe$_2$O$_3$) particles. The spectra were obtained at the indicated temperatures with a magnetic field of 4 T applied parallel to the gamma ray direction. Reproduced with permission from Helgason et al. [15].

angles $\theta_c$ and $-\theta_c$. At very low temperatures, the spins are fixed in one of two energy minima (curves plotted in Figure 3 for the simple canted structure shown in Figure 2). When the temperature is increased, relaxation takes place between the two minima and this results in line broadening, and for very fast relaxation, the nucleus only experiences the average field that is parallel (or antiparallel) to the applied field and the gamma ray direction. Similar data have been found in studies of diamagnetically substituted bulk ferrimagnets such as Mn$_{0.25}$Zn$_{0.75}$Fe$_2$O$_4$ [30] and Li$_{1.125}$Ti$_{1.25}$Fe$_{0.625}$O$_4$ [31].

When the transverse relaxation is fast, the magnitude of the average hyperfine field will be given by $B_0 \langle \cos \theta \rangle$. The fits of the spectra in Figure 6 show that the relative intensity of lines 2 and 5 of sextet 3 does not disappear completely even
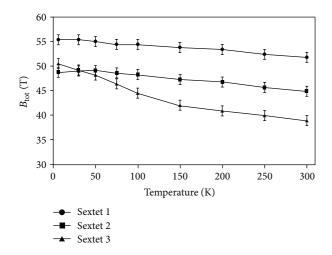
FIGURE 7: Temperature dependence of the total magnetic field at the nuclei, obtained from fits of the spectra shown in Figure 6. Reproduced with permission from Helgason et al. [15].

at 300 K indicating relaxation times of the same order of magnitude as the time scale of Mössbauer spectroscopy. The temperature dependence of the magnetic hyperfine fields of the three sextets is shown in Figure 7. For sextets 1 and 2, the hyperfine fields decrease by a few percent when heating up to 300 K. This is similar to the behavior of bulk maghemite. However, the hyperfine field of sextet 3 decreases much faster with increasing temperature, in accordance with the model for transverse relaxation of the canted spins and the overall temperature dependence of the particle magnetization.

## 4. Spin Reorientation due to Interparticle Interactions

Magnetic interactions between nanoparticles can have a large influence on the magnetic properties. Magnetic dipole interactions between ferromagnetic or ferrimagnetic nanoparticles can significantly affect the superparamagnetic relaxation time [10]. Nanoparticles of antiferromagnetic particles usually have a finite magnetic moment because of uncompensated spins, but this moment is typically so small that the dipole interactions are insignificant [8]. However, if antiferromagnetic nanoparticles are in close proximity, the superparamagnetic relaxation can be suppressed because of exchange interactions between surface atoms of neighboring particles [8, 10]. Such exchange interactions can in some cases also have a strong influence on the spin structure [9, 11, 16]. This can conveniently be investigated by Mössbauer spectroscopy studies. In hematite ($\alpha$-Fe$_2$O$_3$) nanoparticles, the magnitude and the sign of the quadrupole shift depend on the angle $\theta_0$ between the [001] direction of the hexagonal structure and the magnetic hyperfine field. The quadrupole shift is given by [11]

$$\varepsilon = \frac{\varepsilon_0 \left(3\cos^2\theta_0 - 1\right)}{2}, \tag{6}$$

where $\varepsilon_0 = 0.20$ mm/s. In bulk hematite, $\theta_0 = 0°$ below the Morin transition temperature at $T \approx 263$ K, whereas $\theta_0 = 90°$ above this temperature, such that $\varepsilon = -0.10$ mm/s. However, in noninteracting hematite nanoparticles with dimensions below ~20 nm, $\theta_0 = 90°$ at all temperatures, but interparticle interactions can change the spin orientation [11]. In a recent study of $\alpha$-Fe$_2$O$_3$/NiO nanocomposites [16], it was found that interactions between the hematite and nickel oxide nanoparticles can have a very strong influence on the spin orientation in the hematite nanoparticles. Figure 8(a) shows Mössbauer spectra of noninteracting 8 nm hematite particles, and Figure 8(b) shows Mössbauer spectra of hematite nanoparticles from the same batch, but interacting with NiO nanoparticles. At the lowest temperatures, the difference in quadrupole shift of the hematite nanoparticles in the two samples is easily measurable. Fitting the spectra of noninteracting hematite nanoparticles (Figure 8(a)) provides a spin angle of $\theta_0 = 90°$ for all particles. The spectra of the hematite nanoparticles interacting with NiO (Figure 8(b)) were well fitted with two sextets. The quadrupole shifts of the two sextets as a function of temperature are shown in Figure 9. For sextet 1, the quadrupole shift is around + 0.16 mm/s corresponding to $\theta_0 = 21°$, whereas sextet 2 has a quadrupole shift of 0.08 mm/s corresponding to $\theta_0 = 39°$. This clearly shows that the spin angle deviates significantly from that of noninteracting particles where $\theta_0 = 90°$, but we note that the bimodal distribution of spin angles ($\theta_0 = 21°$, $\theta_0 = 39°$) may be a consequence of the fitting procedure using only two sextets. With increasing temperature, the quadrupole shifts of both sextets decrease; that is, the spin angle $\theta_0$ increases. Neutron diffraction studies of the samples confirmed the Mössbauer data and furthermore found that the spin angle is the same within each particle (i.e., no domain formation) [16].

The data can be at least qualitatively understood by considering the interaction between the two particles shown in Figure 10. The magnetic energy of the two particles may be written as

$$E\left(\theta_p, \theta_q\right) = K_p V_p \sin^2\theta_p + K_q V_q \sin^2\theta_q \\ - J_{\text{eff}} M_p M_q \cos\left(\alpha - \theta_p - \theta_q\right). \tag{7}$$

The first two terms represent the anisotropy energies of particles $p$ and $q$, respectively, where $K_p$ and $K_q$ are the anisotropy constants, $V_p$ and $V_q$ the volumes, and $\theta_p$ and $\theta_q$ the angles between the sublattice magnetizations and the easy axes of the particles. The last term comes from the effective exchange interaction between the particles $p$ and $q$ where $J_{\text{eff}}$ is the exchange coupling constant between the sublattice magnetizations, $M_p$ and $M_q$, of the particles $p$ and $q$, and $\alpha$ denotes the angle between the easy axes $\vec{e}_p$ and $\vec{e}_q$. Because of the exchange interaction at the interface, the sublattice magnetization directions $\vec{M}_p$ and $\vec{M}_q$ are rotated by the angles $\theta_p$ and $\theta_q$, respectively. For an arbitrary value of $\theta_p$ the minimum energy is found for

$$\sin 2\theta_q = \frac{K_p V_p}{K_q V_q} \sin 2\theta_p. \tag{8}$$
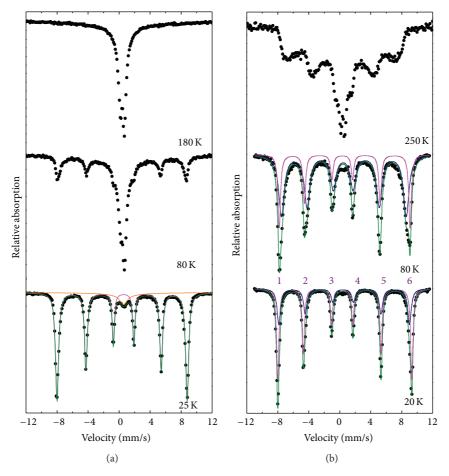
FIGURE 8: Mössbauer spectra of 8 nm hematite ($\alpha$-Fe$_2$O$_3$) nanoparticles obtained at the indicated temperatures. (a) Noninteracting hematite particles coated with oleic acid and in aqueous suspension. (b) Hematite particles mixed with NiO. The spectra of the $\alpha$-Fe$_2$O$_3$/NiO nanocomposite were fitted with two sextets, as shown in panel (b). Reproduced with permission from Frandsen et al. [16].
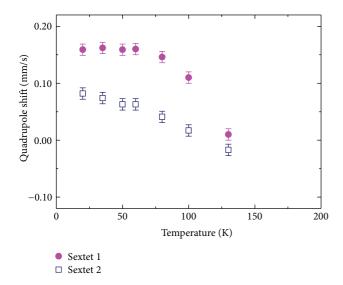


FIGURE 9: Temperature dependence of the quadrupole shift of the two sextet components shown in Figure 8(b). Reproduced with permission from Frandsen et al. [16].

To illustrate the effects of interactions, we here consider the simple case where $K_p V_p = K_q V_q \equiv KV$ for which one can find an analytical solution for the rotation angle $\theta_p = \theta_q \equiv \theta_r$

$$\cot 2\theta_r = \frac{KV}{E_{\text{int}} \sin \alpha} + \cot \alpha, \quad (9)$$

where $E_{\text{int}} = J_{\text{eff}} M_p M_q$. If the easy axes of the two particles are parallel ($\alpha = 0°$), one finds that $\theta_r = 0°$ irrespective of the strength of the interaction energy. However, a large interaction energy compared to the anisotropy in combination with a large value of the angle $\alpha$ results in a large rotation angle, $\theta_r$, at low temperatures. At higher temperatures, the sublattice magnetization directions perform fast fluctuations around the directions corresponding to the energy minima [1, 8, 10]. Therefore, $M_p$ and $M_q$ should be replaced by the thermal averages $\langle M_p \rangle$ and $\langle M_q \rangle$ such that the interaction energy is given by $E_{\text{int}} = J_{\text{eff}} \langle M_p \rangle \langle M_q \rangle$. With increasing temperature, $\langle M_p \rangle$ and $\langle M_q \rangle$ decrease leading to an increase of $\cot 2\theta_r$, that is, a decrease of the spin rotation angle. Such a mechanism
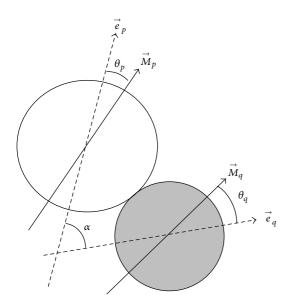
FIGURE 10: Schematic illustration of two interacting nanoparticles with easy axes $\vec{e}_p$ and $\vec{e}_q$ and sublattice magnetization directions $\vec{M}_p$ and $\vec{M}_q$. $\alpha$ is the angle between the two easy axes, and $\theta_p$ and $\theta_q$ denote the angles between the easy axes and the sublattice magnetization of the two particles. Reproduced with permission from Frandsen et al. [16].

can qualitatively explain the temperature dependence of the reorientation angle.

Also, in samples of interacting hematite particles, a spin reorientation has been observed, but the effect is smaller than that in the $\alpha$-Fe$_2$O$_3$/NiO nanocomposite [11].

## 5. Conclusions

Theoretical and experimental studies of magnetic nanoparticles show that the spin structures often differ from those of perfect bulk materials. The low symmetry around surface atoms and around defects in the interior of the particles can lead to localized spin canting, and also thermal fluctuations between almost degenerate spin states may take place even at low temperature. This can lead to anomalous magnetization behaviors of nanoparticles. Furthermore, exchange interactions between surface atoms of neighboring nanoparticles in close proximity can result in reorientation of the sublattice magnetization directions in the whole particles.

## Conflict of Interests

The authors declare no conflict financial of interests.

## References

[1] S. Mørup, M. F. Hansen, and C. Frandsen, "Magnetic nanoparticles," in *Comprehensive Nanoscience and Technology*, D. Andrews, G. Scholes, and G. Wiederrecht, Eds., vol. 1, pp. 437–491, Elsevier, 2011.

[2] L. Néel, "Théorie du traînage magnétique des ferromagnétiques en grains fins avec applications aux terres cuites," *Annales Geophysique*, vol. 5, pp. 99–136, 1949.

[3] W. F. Brown, "Thermal fluctuations of a single-domain particle," *Physical Review*, vol. 130, p. 1677, 1963.

[4] S. Mørup, C. Frandsen, and M. F. Hansen, "Uniform excitations in magnetic nanoparticles," *Beilstein Journal of Nanotechnology*, vol. 1, pp. 48–54, 2010.

[5] J. M. D. Coey, "Noncollinear spin arrangement in ultrafine ferrimagnetic crystallites," *Physical Review Letters*, vol. 27, pp. 1140–1142, 1971.

[6] A. H. Morrish and K. Haneda, "Surface magnetic properties of fine particles," *Journal of Magnetism and Magnetic Materials*, vol. 35, p. 105, 1983.

[7] S. Mørup, "Spin-canting and transverse relaxation at surfaces and in the interior of ferrimagnetic particles," *Journal of Magnetism and Magnetic Materials*, vol. 266, p. 110, 2003.

[8] M. F. Hansen, C. Bender Koch, and S. Mørup, "Magnetic dynamics of weakly and strongly interacting hematite nanoparticles," *Physical Review B*, vol. 62, p. 1124, 2000.

[9] C. Frandsen and S. Mørup, "Inter-particle interactions in composites of antiferromagnetic nanoparticles," *Journal of Magnetism and Magnetic Materials*, vol. 266, p. 36, 2003.

[10] S. Mørup, M. F. Hansen, and C. Frandsen, "Magnetic interactions between nanoparticles," *Beilstein Journal of Nanotechnology*, vol. 1, p. 182, 2010.

[11] C. Frandsen and S. Mørup, "Spin rotation in $\alpha$-Fe$_2$O$_3$ nanoparticles by interparticle interactions," *Physical Review Letters*, vol. 94, Article ID 027202, 2005.

[12] R. H. Kodama, A. E. Berkowitz, E. J. McNiff Jr., and S. Foner, "Surface spin disorder in NiFe$_2$O$_4$ nanoparticles," *Physical Review Letters*, vol. 77, no. 2, pp. 394–397, 1996.

[13] R. H. Kodama and A. E. Berkowitz, "Atomic-scale magnetic modeling of oxide nanoparticles," *Physical Review B*, vol. 59, p. 6321, 1999.

[14] H. Jacobsen, K. Lefmann, E. Brok, C. Frandsen, and S. Mørup, "Temperature dependence of the magnetization of canted spin structures," *Journal of Magnetism and Magnetic Materials*, vol. 324, p. 3218, 2012.

[15] Ö. Helgason, H. K. Rasmussen, and S. Mørup, "Spin-canting and transverse relaxation in maghemite nanoparticles and in tin-doped maghemite," *Journal of Magnetism and Magnetic Materials*, vol. 302, p. 413, 2006.

[16] C. Frandsen, K. Lefmann, B. Lebech et al., "Spin reorientation in $\alpha$-Fe$_2$O$_3$ nanoparticles induced by interparticle exchange interactions in $\alpha$-Fe$_2$O$_3$/NiO nanocomposites," *Physical Review B*, vol. 84, Article ID 214435, 2011.

[17] E. Tronc, A. Ezzir, R. Cherkaoui et al., "Surface-related properties of $\gamma$-Fe$_2$O$_3$ nanoparticles," *Journal of Magnetism and Magnetic Materials*, vol. 221, p. 63, 2000.

[18] H. Kachkachi, A. Ezzir, M. Nogués, and E. Tronc, "Surface effects in nanoparticles: application to maghemite $\gamma$-Fe$_2$O$_3$," *The European Physical Journal B*, vol. 14, p. 681, 2000.

[19] T. N. Shendruk, R. D. Desautels, B. W. Southern, and J. van Lierop, "The effect of surface spin disorder on the magnetism

of $\gamma$-$Fe_2O_3$ nanoparticle dispersions," *Nanotechnology*, vol. 18, no. 45, Article ID 455704, 2007.

[20] F. T. Parker, M. W. Foster, D. T. Margulies, and A. E. Berkowitz, "Spin canting, surface magnetization, and finite-size effects in $\gamma$-$Fe_2O_3$ particles," *Physical Review B*, vol. 47, no. 13, pp. 7885–7891, 1993.

[21] K. Mandal, S. Mitra, and P. A. Kumar, "Deviation from Bloch T3/2 law in ferrite nanoparticles," *Europhysics Letters*, vol. 75, no. 4, pp. 618–623, 2006.

[22] D. Peddis, C. Cannas, G. Piccaluga, E. Agostinelli, and D. Fiorani, "Spin-glass-like freezing and enhanced magnetization in ultra-small $CoF_2O_4$ nanoparticles," *Nanotechnology*, vol. 21, no. 12, Article ID 125705, 2010.

[23] C. N. Chinnasamy, A. Narayanasamy, N. Ponpandian et al., "Mixed spinel structure in nanocrystalline $NiFe_2O_4$," *Physical Review B*, vol. 63, no. 18, Article ID 184108, 2001.

[24] B. Martinez, X. Obradors, L. Balcells, A. Rouanet, and C. Monty, "Low temperature surface spin-glass transition in $\gamma$-$Fe_2O_3$ nanoparticles," *Physical Review Letters*, vol. 80, p. 181, 1997.

[25] C. J. Serna, F. Bødker, S. Mørup, M. P. Morales, F. Sandiumenge, and S. Veintemillas-Verdaguer, "Spin frustration in maghemite nanoparticles," *Solid State Communications*, vol. 118, no. 9, pp. 437–440, 2001.

[26] S. Chkoundali, S. Ammer, N. Jouini et al., "Nickel ferrite nanoparticles: elaboration in polyol medium via hydrolysis, and magnetic properties," *Journal of Physics: Condensed Matter*, vol. 16, p. 4357, 2004.

[27] A. G. Roca, D. Niznansky, J. Poltierova-Vejpravova et al., "Magnetite nanoparticles with no surface spin canting," *Journal of Applied Physics*, vol. 105, no. 11, Article ID 114309, 2009.

[28] G. Fonnum, C. Johansson, A. Molteberg, S. Mørup, and E. Aksnes, "Characterisation of Dynabeads (R) by magnetization measurements and Mössbauer spectroscopy," *Journal of Magnetism and Magnetic Materials*, vol. 293, p. 41, 2005.

[29] E. Tronc, P. Prené, J. P. Jolivet, J. L. Dormann, and G. M. Grenèche, "Spin canting in $\gamma$-$Fe_2O_3$ nanoparticles," *Hyperfine Interactions*, vol. 112, p. 97, 1998.

[30] T. A. Anhøj, B. Bilenberg, B. Thomsen et al., "Spin canting and magnetic relaxation phenomena in $Mn_{0.25}Zn_{0.75}Fe_2O_4$," *Journal of Magnetism and Magnetic Materials*, vol. 260, p. 115, 2003.

[31] J. L. Dormann, M. El Harfaoui, M. Noguès, and J. Jove, "Relaxation of the transverse spin component in randomly canted Li-Ti ferrite below $T_N$," *Journal of Physics C*, vol. 20, p. L161, 1987.

*Research Article*

# Synthesis of Silica-Coated Magnetic Nanoparticles and Application in the Detection of Pathogenic Viruses

**Dao Van Quy,[1] Nguyen Minh Hieu,[2] Pham Thi Tra,[1] Nguyen Hoang Nam,[2] Nguyen Hoang Hai,[2,3] Nguyen Thai Son,[4] Phan Tuan Nghia,[1] Nguyen Thi Van Anh,[1] Tran Thi Hong,[2] and Nguyen Hoang Luong[2,3]**

[1] *Key Laboratory for Enzyme and Protein Technology, VNU University of Science, 334 Nguyen Trai, Thanh Xuan, Hanoi, Vietnam*

[2] *VNU University of Science, 334 Nguyen Trai, Thanh Xuan, Hanoi, Vietnam*

[3] *Nano and Energy Center, Vietnam National University, 334 Nguyen Trai, Thanh Xuan, Hanoi, Vietnam*

[4] *Hospital 103, 104 Phung Hung, Ha Dong, Hanoi, Vietnam*

Correspondence should be addressed to Nguyen Hoang Luong; luongnh@vnu.edu.vn

Magnetic $Fe_3O_4$ nanoparticles were prepared by coprecipitation and then coated with silica. These $Fe_3O_4/SiO_2$ nanoparticles consisted of a 10–15 nm magnetic core and a silica shell of 2–5 nm thickness. The superparamagnetic property of the $Fe_3O_4/SiO_2$ particles with the magnetization of 42.5 emu/g was confirmed by vibrating sample magnetometer (VSM). We further optimized buffers with these $Fe_3O_4/SiO_2$ nanoparticles to isolate genomic DNA of hepatitis virus type B (HBV) and of Epstein-Barr virus (EBV) for detection of the viruses based on polymerase chain reaction (PCR) amplification of a 434 bp fragment of *S* gene specific for HBV and 250 bp fragment of nuclear antigen encoding gene specific for EBV. The purification efficiency of DNA of both HBV and EBV using obtained $Fe_3O_4/SiO_2$ nanoparticles was superior to that obtained with commercialized $Fe_3O_4/SiO_2$ microparticles, as indicated by (i) brighter PCR-amplified bands for both HBV and EBV and (ii) higher sensitivity in PCR-based detection of EBV load (copies/mL). The time required for DNA isolation using $Fe_3O_4/SiO_2$ nanoparticles was significantly reduced as the particles were attracted to magnets more quickly (15–20 s) than the commercialized microparticles (2-3 min).

## 1. Introduction

Isolation of nucleic acids from clinical samples is an essential step in diagnostics, such as in the detection of pathogenic viruses and bacteria using the polymerase chain reaction (PCR), paternity testing, DNA fingerprinting for crime detection, and DNA sequencing. The nucleic acid isolation method based on interaction with silica, created by Boom et al. in 1990 [1], is currently the most commonly used. Recently, micrometer-size silica-coated magnetic beads have been developed by different groups [2, 3] and biotech companies such as Roche Diagnostics, Life Technologies, Beckman Coulter, and Promega to improve the efficiency of purification and save working time because the purification procedures could be performed automatically. This development is very useful for enrichment of nucleic acids in clinical samples with a low copy number of the pathogen, tuberculosis bacterium in sputum, for example, thereby increasing the sensitivity of detection using PCR method [4]. In comparison to the micrometer-size silica-coated magnetic beads, silica-coated magnetic nanoparticles have larger total surface area, thus could be more functional in purification of DNA from samples. However, the synthesis of silica-coated magnetite nanoparticles for specific applications in nucleic acid purification of viruses in blood, which is a very important step in the diagnosis of viruses in specimen, is an emerging area. We therefore present a method for synthesizing the $SiO_2$-coated $Fe_3O_4$ magnetic nanoparticles and use the particles in the isolation of DNA of Hepatitis virus type B (HBV) and Epstein-Barr virus (EBV) from several real

serum samples. These viruses are commonly found in blood infection and the cause of hepatitis (HBV) and particular cancers and lymphomas (EBV) [4, 5].

## 2. Materials and Methods

*2.1. Synthesis of Silica-Coated Magnetic Nanoparticles.* Magnetic $Fe_3O_4$ nanoparticles were synthesized by using coprecipitation from iron (III) chloride and iron (II) chloride solutions with the assistance of aqueous ammonia solution as described elsewhere [6]. The synthesized magnetic nanoparticles were washed several times with alcohol and then distilled water until pH 7.0. $Fe_3O_4/SiO_2$ nanoparticles were prepared by coating magnetic nanoparticles with silica. 100 mL of the suspension of prepared magnetic nanoparticles (containing 1 g magnetite) was stored in a flask. 50 mL of the 10% solution of aqueous tetraethylorthosilicate (TEOS) was added to the flask together with 70 mL alcohol and mixed using an overhead stirrer. The pH of the suspension was adjusted to 9.0 with NaOH. The flask was then heated to 90°C and stirred at this temperature for 6 h. After cooling to room temperature (RT), the suspension was washed twice with alcohol and six times with distilled water. The final suspension volume was adjusted to 100 mL with water.

$Fe_3O_4/SiO_2$ nanoparticles were characterized using a transmission electron microscope (TEM JEM1010, JEOL) and Fourier-transform infrared (FTIR) spectroscopy (FT/IR-6300, JASCO). Magnetic curves were measured using a DMS-880 vibrating sample magnetometer (VSM) at RT.

For further experiments in nucleic acid isolation, $Fe_3O_4/SiO_2$ nanoparticles were stored in 100 mM Tris-HCl buffer (pH 7.0). For each DNA isolation reaction from 200 $\mu$L serum sample, 50 $\mu$L of $Fe_3O_4/SiO_2$ nanoparticles at a concentration of 25 mg/mL was used.

*2.2. Preparation of DNA Isolation Buffers.* A set of nucleic acid buffers were made based on the method described previously by Boom et al. [1] and optimized in this work suitably for properties of $Fe_3O_4/SiO_2$ nanoparticles. The set contained (i) Proteinase K 20 mg/mL (BioBasic), (ii) lysis buffer (LB: 30 mM Tris-HCl pH 7.0, 1 M NaCl, 4.5 M GuSCN, 20 mM EDTA, 1.5% Triton X-100), (iii) two types of washing buffers (WB1: 30 mM Tris-HCl, pH 7.0, 2.25 M GuSCN, 56% ethanol; WB2: 10 mM Tris-HCl pH 7.0, 70% ethanol), and (iv) elution buffer (EB: 10 mM Tris-HCl pH 8.5, 1 mM EDTA).

*2.3. Primer Design and Cloning of Plasmids Harbouring Specific Genes for HBV and EBV as Standards for PCR.* The primers for HBV (HBSF: 5′-CTTTCATCCTGCTGCTATGCCT; HBSR: 5′-AGGGTTCAAATGTATACCCAAAGACA-3′) were designed based on previous work by Abe et al. [7] and Nghia et al. [8], for the amplification of a 434 bp specific fragment of *S* gene for HBV. Sets of primers for nested PCR to detect EBV (EBVexF: 5′-TGGAAACCCGTCACTCTC-3′; EBVexR: 5′-AATGGCATAGGTGGAATG-3′; EBVinF: TGTTGGAAACCCGTCACTCTC-3′; EBVinR: 5′-GGG-TAATGGCATAGGTGGAATG-3′) were designed based on the modification of previous primer design studies by

van Baarle et al. [5], which was based on the conserved sequence of genes encoding the nuclear antigens EBNA-2 that generated a DNA product of 250 bp (named as EBV-250). The PCR primers (EBVF3: 5′-GGAACCTGGTCA-TCCTTGC-3′; EBFR3: 5′-ACGTGCATGGACCGGTTA-AT-3′; EBV Taqman probe: 5′-(FAM)-CGCAGGCACTCG-TACTGCTCGCT-(TAMRA)-3′) for real-time PCR using TaqMan probe (Roche Diagnostics) to measure EBV virus load were designed previously [9] based on the sequence encoding nonglycosylated membrane protein BNRF1 p143 and generating a PCR product of 74 bp named as EBV-74. The 434 bp for HBV and 250 bp and 74 bp for EBV were cloned into pGEM-T/A plasmid (Promega). The plasmids harbouring the specific 434 bp bands for HBV were named as pGEM-HBV. The ones harbouring the specific 250 bp and 74 bands for EBV were named as pGEM-EBV-250 and pGEM-EBV-74, respectively. The cloned plasmids were then purified and used as a template for sequencing their specific inserted genes for HBV (HBV-434) and EBV (EBV-250, EBV-74). The sequences were compared for homology to the above-mentioned standard genes for HBV and EBV (as posted on the international gene bank). The plasmids were diluted into 10-fold serial concentrations ranging from $4 \times 10^9$ to $4 \times 10^2$ copies/mL.

*2.4. Recovery of Standard DNA Plasmid and Isolation of Genomic DNA of Viruses from Serum.* HBV and EBV negative and positive serum samples were collected at the National Hospital of Tropical Diseases, Hospital 103, and Bach Mai Hospital, Vietnam. Either standard DNA plasmids pGEM-HBV, pGEM-EBV-250, and pGEM-EBV-74 or serum samples containing HBV and EBV were recovered or purified using obtained $Fe_3O_4/SiO_2$ nanoparticles and the optimized buffers in this work. Silica-coated $Fe_3O_4/SiO_2$ microparticles named Dynabeads Myone Silane (Life Technologies) were used as controls for our $Fe_3O_4/SiO_2$ nanoparticles. The protocol for isolating DNA of the virus from multi-serum samples was set up using special 96-well ELISA plastic plates (Thermo Scientific, code 5530100) and MagnaBot 96 Magnetic Separation (Promega), which included four steps. (i) Lysis to release virus genomic DNA: 20 $\mu$L proteinase K (10 mg/mL) and 300 $\mu$L LB were added into 200 $\mu$L of serum sample. The solution was mixed well by pipetting 3–5 times before incubating at RT for 10 min. (ii) Binding of the released DNA onto $Fe_3O_4/SiO_2$ nanoparticles in LB. Next, 50 $\mu$L of $Fe_3O_4/SiO_2$ nanoparticles and 150 $\mu$L isopropanol were added to the LB-treated serum. The mixture was incubated for 3 min at RT for binding of DNA onto the $Fe_3O_4/SiO_2$ nanoparticles. Then MagnaBot 96 Magnetic Separation (Promega) was applied for 30 s to attract $Fe_3O_4/SiO_2$ nanoparticles bound with DNA and for 3 min to attract Dynabeads Myone Silane bound with DNA or until the solution was clear/white. Next, the clear solution was removed. (iii) Washing off contaminated non-DNA biomolecules using WB1 and WB2: MagnaBot 96 was switched off and WB1 was added into the wells containing $Fe_3O_4/SiO_2$ nanoparticles, followed by mixing well the suspension pipetting 5 times. Then MagnaBot 96 was applied again for attracting $Fe_3O_4/SiO_2$ nanoparticles,
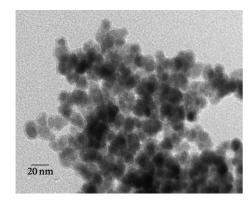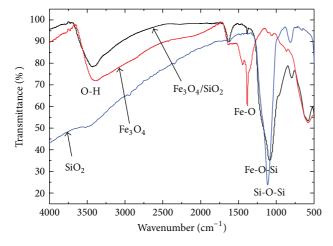
FIGURE 1: TEM image of $Fe_3O_4/SiO_2$ nanoparticles.



FIGURE 2: FTIR spectra of $SiO_2$, $Fe_3O_4$, and $Fe_3O_4/SiO_2$ nanoparticles.



FIGURE 3: Magnetization curves of $Fe_3O_4$ and $Fe_3O_4/SiO_2$ at room temperature.

allowing removal of the washing solution. This step was repeated with WB2. In this case, WB2 must be completely removed and residual ethanol evaporated by air drying. (iv) Elution using EB: MagnaBot 96 was switched off and 100 $\mu$L EB was added in to each well for mixing by pipetting 5 times. The suspension was incubated at 65°C for 3 min. The solution containing DNA was eluted after applying MagnaBot 96 to attract the nanoparticles. For recovery of standard DNA plasmids, the same protocol was intentionally applied. Isolated DNA concentration was measured and calculated by absorbance at 260 nm using a NanoDrop spectrophotometer (Thermo Scientific). The samples were used immediately or stored at −80°C for PCR detection of specific DNA bands for EBV and HBV.

*2.5. Polymerase Chain Reaction to Detect HBV and EBV.* Purified DNA of HBV from serum samples were used as a template for PCR detection of HBV, as described by Nghia et al. [8]. Amplification of 250 bp specific fragments for EBV was optimized in this work under 35 cycles of the following conditions: 94°C for 30 s, 52°C (initial 5 cycles) and 56°C (following 25 cycles) for 45 s, and 72°C for 60 s. Real-time PCR to quantitatively measure the EBV virus
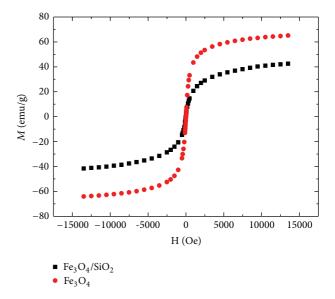
load through amplification of 74 bp specific for EBV was performed following Niesters et al. [9] using 45 cycles of the following conditions: 95°C for 15 s and 60°C for 1 min.

## 3. Results and Discussion

*3.1. Properties of Silica-Coated Magnetic Nanoparticles.* Figure 1 shows the TEM image of $Fe_3O_4/SiO_2$ nanoparticles. From this image it can be seen that $Fe_3O_4/SiO_2$ nanoparticles were formed by 10–15 nm diameter of seed and the surrounding layer has a thickness of about 2–5 nm. Figure 2 shows the FTIR spectra of prepared $Fe_3O_4$, $Fe_3O_4/SiO_2$ nanoparticles and $SiO_2$ for comparison. In all spectra, the absorption bands at $3650 \div 3200$ cm$^{-1}$ correspond to O–H stretching mode. The spectra of $Fe_3O_4$ and $Fe_3O_4/SiO_2$ show the absorption bands near 500 cm$^{-1}$ which are assigned to Fe–O stretching mode. The spectrum of $SiO_2$ shows the Si–O–Si stretching vibration at $1070 \div 1080$ cm$^{-1}$. The spectrum of $Fe_3O_4$ shows an absorption at around 1390 cm$^{-1}$ which is assigned to Fe–O stretching mode. This absorption also appears in the spectrum of $Fe_3O_4/SiO_2$ but with smaller intensity. This can be explained by the covering of $SiO_2$ layers. The existence of $SiO_2$ layers in the spectrum of $Fe_3O_4/SiO_2$ can be seen by the Si–O–Si stretching vibration at $1070 \div 1080$ cm$^{-1}$ as well as the Fe–O–Si stretching vibration at $1050 \div 1250$ cm$^{-1}$. The data strongly suggest that the $Fe_3O_4$ nanoparticles were successfully coated with $SiO_2$ layers. The FTIR results can be used for confirming the silica coating on nanoparticles as recently discussed by Luong et al. [10] on $SiO_2$-coated FePt nanoparticles.

Figure 3 shows the magnetic curves of $Fe_3O_4$ and $Fe_3O_4/SiO_2$ nanoparticles measured at room temperature. Both of them show superparamagnetic property (i.e., no remanence effect) with high saturation magnetization of

TABLE 1: Quantitation of EBV load in serum using DNA templates purified by $Fe_3O_4/SiO_2$ nanoparticles and Dynabeads.

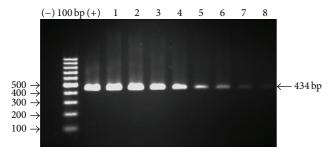| Sample number | Material for DNA isolation | $C_t$ (threshold cycle) | Virus load (copies/mL) |
|---|---|---|---|
| 7 | $Fe_3O_4/SiO_2$ nanoparticles | 36.2 | $7.17 \times 10^3$ |
|   | Dynabeads | 40.62 | $6.53 \times 10^2$ |
| 10 | $Fe_3O_4/SiO_2$ nanoparticles | 26.78 | $1.18 \times 10^6$ |
|   | Dynabeads | 27.73 | $7.04 \times 10^5$ |



FIGURE 4: Electrophoresis result of PCR products of HBV specific gene using recovered DNA plasmids pGEM-HBV as templates. (−) negative control, 100 bp DNA ladder, (+) positive control: PCR product of purified pGEM-HBV, lane 1–8: PCR products using DNA plasmids after recovering by $Fe_3O_4/SiO_2$ nanoparticles at tenfold diluted initial DNA concentrations, ranging from $4 \times 10^9$ copies/mL (lane 1) to $4 \times 10^2$ copies/mL (lane 8).

42.5 emu/g and 65.1 emu/g for $Fe_3O_4/SiO_2$ and $Fe_3O_4$ samples, respectively. The $Fe_3O_4/SiO_2$ sample had a smaller magnetization because the magnetic nanoparticles were coated with nonmagnetic layers of $SiO_2$. From the above values of magnetization, the average thickness of the $SiO_2$ layers can be estimated to be 1–1.5 nm, in good agreement with that obtained from TEM measurements.

*3.2. Purification of DNA of Hepatitis Virus Type B (HBV) Using Silica-Coated Magnetic Nanoparticles and Optimized Buffers.* Before testing the DNA purification procedure with real serum samples, we measured the efficiency of DNA recovery of the $Fe_3O_4/SiO_2$ nanoparticles and the optimized buffers using standard pure pGEM-HBV plasmid at 10-fold diluted concentrations ranging from $4 \times 10^9$ copies/mL to $4 \times 10^2$ copies/mL. The enriched DNA solutions were used as templates for amplification of 434 bp fragment of *S* gene specific for HBV. As shown in Figure 4, from left to right, we could detect bands of about 434 bp with reducing intensities proportional to reducing concentrations from $4 \times 10^9$ copies/mL to $4 \times 10^2$ copies/mL (Figure 4, lane 1–8). This result indicates that $Fe_3O_4/SiO_2$ nanoparticles and the optimized buffer could successfully enrich DNA from solution and that the purified DNA was qualified for further PCR-based detection of HBV at a sensitivity of $4 \times 10^2$ copies/mL.

We then used $Fe_3O_4/SiO_2$ nanoparticles and the buffers to isolate DNA of HBV in six real serum samples (one negative Figure 5 lane 5 and five positives Figure 5 lane 1–4, 6). As a result, we could observe faint specific bands of 434 bp for HBV in samples in lanes 1 and 3, and very bright bands of
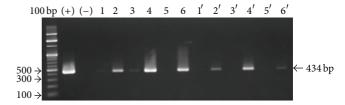


FIGURE 5: Electrophoresis result of PCR products of HBV specific gene using DNA purified by $Fe_3O_4/SiO_2$ nanoparticles: 100 bp DNA ladder, (+) positive control: PCR product of purified pGEM-HBV, (−) negative control, lanes 1 to 6: PCR products using purified DNA from samples from number 1 to 6 by $Fe_3O_4/SiO_2$ nanoparticles, lane 1′ to 6′: PCR products using purified DNA from samples from number 1 to 6 by Dynabeads.

434 bp for HBV in samples in lanes 2, 4, and 6. Meanwhile, no band was observed in the sample in lane 5. The data indicates that six real serum samples had different concentrations of virus copies, of which the sample in lane 6 had the highest virus load. Our data were in good agreement with those confirmed by the hospital where the samples were collected. In parallel, we performed similar experiments with these six serum samples using the commercialized silica-coated magnetic microparticles Dynabeads Myone Silane (short name: Dynabeads, Life Technologies). As shown in Figure 5, clear bands of 434 bp for HBV were observed in the samples in lane 2′, 4′, and 6′. However, intensities of those bands were weaker compared to those in the same samples in lanes 2, 4, and 6 obtained in the case of $Fe_3O_4/SiO_2$ nanoparticles. We could not observe the specific PCR-amplified bands in the samples in lanes 1′ and 3′, possibly due to the low levels of purified template DNA obtained when using Dynabeads. We conclude then that $Fe_3O_4/SiO_2$ nanoparticles may be more efficient than Dynabeads in DNA isolation of HBV from serum.

*3.3. Purification of DNA of Epstein-Barr Viruses (EBV) Using Silica-Coated Magnetic Nanoparticles and Optimized Buffers.* $Fe_3O_4/SiO_2$ nanoparticles and the buffers were then used to isolate DNA of EBV in real serum samples, in comparison to Dynabeads. Among 10 suspected EBV infected serum samples, we could detect clearly 250 bp specific bands for EBV in the samples 7 and 10 using both $Fe_3O_4/SiO_2$ nanoparticles (Figure 6(a), lanes 7 and 10) and Dynabeads (Figure 6(b), lanes 7′ and 10′). However, the brighter signals were observed when using $Fe_3O_4/SiO_2$ nanoparticles, indicating that the DNA isolation efficiency of EBV by $Fe_3O_4/SiO_2$ nanoparticles was higher than that using Dynabeads. Further, real-time
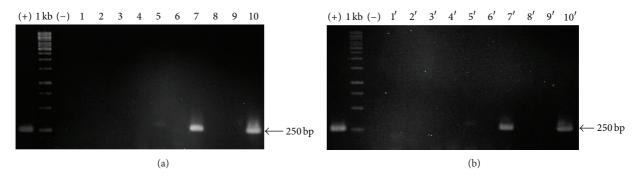
(a)



(b)

FIGURE 6: Electrophoresis result of PCR products of EBV specific gene using DNA purified by $Fe_3O_4/SiO_2$ nanoparticles (a) and Dynabeads (b). (a) (+): PCR product of positive control pGEM-EBV, 1 Kb DNA ladder, (−): negative control, lane 1–10: PCR products using purified DNA of EBV from serum samples from number 1 to 10 by $Fe_3O_4/SiO_2$ nanoparticles. (b) Lane $1'$–$10'$: PCR products using purified DNA of EBV from serum samples from number 1 to 10 by Dynabeads.
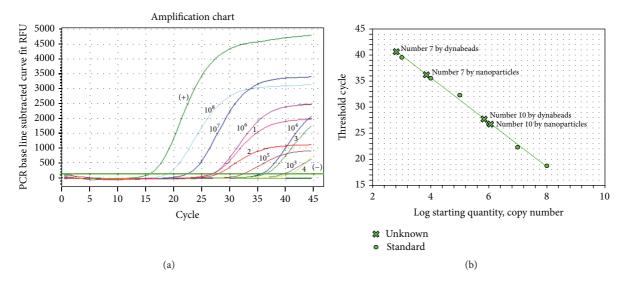


(a)

(b)

FIGURE 7: Real-time PCR for qualitative measurement EBV virus load using DNA templates purified by $Fe_3O_4/SiO_2$ nanoparticles and Dynabeads. (a) Amplification chart of EBV-74 fragments specific for EBV from sample 7, sample 10, standards, and positive and negative controls. (+): PCR product of positive control pGEM-EBV-74 at $5 \times 10^8$ copies/mL, (−) negative controls, $10^3$ to $10^8$ copies/mL were labeled next to each respective amplification curves of standards. (b) Linear regression line based on standards and featured with samples 7 and 10 purified by $Fe_3O_4/SiO_2$ nanoparticles and Dynabeads ($R^2 = 0.996$). 1, 2, 3, and 4 were labeled next to amplification curves of samples number 7 by Nanoparticles, number 7 by Dynabeads, number 10 by Nanoparticles, and number 10 by Dynabeads, respectively.

PCR based on highly specific Taqman probe dually labeled with FAM at $5'$-end and TAMRA at $3'$-end was performed with samples 7 and 10 to quantify the EBV virus load. As shown in the amplification chart of Figure 7, the negative control had no amplification curve while the positive control had an amplification curve occurring earlier ($C_t = 15.65$). All standards together with samples 7 and 10 purified by both particles had amplification curves. The linear regression line of standards had $R^2 = 0.996$ value, indicating that the reliability of the qualitative measurement for EBV virus load was high. The concentration of EBV in sample 7 using DNA purified by $Fe_3O_4/SiO_2$ nanoparticles ($= 7.17 \times 10^3$ copies/mL), although this was much lower than that in sample 10 ($= 1.18 \times 10^6$ copies/mL), but was not too low because it fell in the range of standards. Nanoparticles are therefore suitable for isolating DNA at such low virus concentration. The result in Table 1 indicates that higher concentrations of EBV (copies/mL) in both samples were measured with using $Fe_3O_4/SiO_2$ nanoparticles to purify DNA compared to those with using Dynabeads. The increase in DNA isolation efficiency by $Fe_3O_4/SiO_2$ nanoparticles is likely due to a larger total surface of silica-coated magnetic nanoparticles. During the process of DNA isolation, we have found that the time required for magnets to attract completely the Dynabeads from solution was much longer, about 2-3 min, compared to 15–20 s for $Fe_3O_4/SiO_2$ nanoparticles. This phenomenon is probably also due to the fact that $Fe_3O_4/SiO_2$ nanoparticles have a larger total surface area compared to that of the Dynabeads.

## 4. Conclusion

Our study demonstrates that $Fe_3O_4/SiO_2$ nanoparticles and the optimized buffers can isolate genomic DNA of two types

of viruses, HBV and EBV, for further PCR-based detection of the viruses in serum samples. The obtained primary data indicates that $Fe_3O_4/SiO_2$ nanoparticles provided better sensitivity and were time saving in detection of HBV and EBV, compared to that of the commercialized silica-coated magnetic microparticles. Further experiments on nucleic acid isolation of other pathogenic viruses infected in blood using the $Fe_3O_4/SiO_2$ nanoparticles are in progress.

## Conflict of Interests

The authors declare no conflict of interests.

## Acknowledgments

## References

[1] R. Boom, C. J. A. Sol, M. M. M. Salimans, C. L. Jansen, P. M. E. Wertheim-van Dillen, and J. van der Noordaa, "Rapid and simple method for purification of nucleic acids," *Journal of Clinical Microbiology*, vol. 28, no. 3, pp. 495–503, 1990.

[2] J.-I. Akutsu, Y. Tojo, O. Segawa et al., "Development of an integrated automation system with a magnetic bead-mediated nucleic acid purification device for genetic analysis and gene manipulation," *Biotechnology and Bioengineering*, vol. 86, no. 6, pp. 667–671, 2004.

[3] P. Ashtari, X. He, K. Wang, and P. Gong, "An efficient method for recovery of target ssDNA based on amino-modified silica-coated magnetic nanoparticles," *Talanta*, vol. 67, no. 3, pp. 548–554, 2005.

[4] R. Caldarelli-Stefano, L. Vago, S. Bonetto, M. Nebuloni, and G. Costanzi, "Use of magnetic beads for tissue DNA extraction and IS6110 *Mycobacterium tuberculosis* PCR," *Molecular Pathology*, vol. 52, no. 3, pp. 158–160, 1999.

[5] D. van Baarle, E. Hovenkamp, M. J. Kersten, M. R. Klein, F. Miedema, and M. H. J. van Oers, "Direct Epstein-Barr virus (EBV) typing on peripheral blood mononuclear cells: no association between EBV type 2 infection or superinfection and the development of acquired immunodeficiency syndrome-related non-Hodgkin's lymphoma," *Blood*, vol. 93, no. 11, pp. 3949–3955, 1999.

[6] N. H. Hai, N. D. Phu, N. H. Luong et al., "Mechanism for sustainable magnetic nanoparticles under ambient conditions," *Journal of the Korean Physical Society*, vol. 52, no. 5, pp. 1327–1331, 2008.

[7] A. Abe, K. Inoue, T. Tanaka et al., "Quantitation of hepatitis B virus genomic DNA by real-time detection PCR," *Journal of Clinical Microbiology*, vol. 37, no. 9, pp. 2899–2903, 1999.

[8] P. T. Nghia, K. T. Nga, N. T. H. Loan et al., "Multiplex (RT)-PCR assay for detection of co-infection of HBV, HCV and HIV in blood samples," *VNU Journal of Science, Natural Sciences and Technology*, vol. 24, no. 2, supplement, pp. 377–383, 2008.

[9] H. G. M. Niesters, J. van Esser, E. Fries, K. C. Wolthers, J. Cornelissen, and A. D. M. E. Osterhaus, "Development of a real-time quantitative assay for detection of Epstein-Barr virus," *Journal of Clinical Microbiology*, vol. 38, no. 2, pp. 712–715, 2000.

[10] N. H. Luong, N. D. Phu, N. H. Hai, and N. T. D. Thuy, "Surface modification of $SiO_2$-coated FePt nanoparticles with Amino Groups," *e-Journal of Surface Science and Nanotechnology*, vol. 9, pp. 536–538, 2011.

## Research Article

# Magnetic Properties and Biological Activity Evaluation of Iron Oxide Nanoparticles

**Alina Mihaela Prodan,**[1,2] **Simona Liliana Iconaru,**[3,4,5] **Carmen Mariana Chifiriuc,**[6] **Coralia Bleotu,**[7] **Carmen Steluta Ciobanu,**[3] **Mikael Motelica-Heino,**[5] **Stanislas Sizaret,**[5] **and Daniela Predoi**[3]

[1] *Carol Davila University of Medicine and Pharmacy, 8 Eroii Sanitari, Sector 5, Bucharest, Romania*
[2] *Emergency Hospital Floreasca, Bucharest 5, Calea Floreasca Nr 8, Sector 1, Bucharest, Romania*
[3] *National Institute of Materials Physics, 105 bis Atomistilor, P.O. Box MG 07, 077125 Bucuresti-Magurele, Romania*
[4] *Faculty of Physics, University of Bucharest, 405 Atomistilor, CP MG-1, 077125 Magurele, Romania*
[5] *ISTO, Université d'Orléans, Orléans Cedex 02, 45067, France*
[6] *Microbiology Department, Faculty of Biology, University of Bucharest, Aleea Portocalelor 1-3, 60101 Bucharest, Romania*
[7] *Institute of Virology, Antiviral Therapy Department "Stefan S. Nicolau", 285 Mihai Bravu, 030304 Bucharest, Romania*

Correspondence should be addressed to Daniela Predoi; dpredoi@gmail.com

Received 14 March 2013; Revised 7 June 2013; Accepted 8 June 2013

Academic Editor: Anjan Barman

The aim of this study was to provide information about the biological properties of iron oxide nanoparticles (IO-NPs) obtained in an aqueous suspension. The IO-NPs were characterized by transmission electron microscopy (TEM). Analysis of hysteresis loops data at room temperature for magnetic IO-NPs sample indicated that the IO-NPs were superparamagnetic at room temperature. The calculated saturation magnetization for magnetic iron oxide was $M_s = 18.1$ emu/g. The antimicrobial activity of the obtained PMC-NPs was tested against Gram-negative (*Pseudomonas aeruginosa* 1397, *Escherichia coli* ATCC 25922), Gram-positive (*Enterococcus faecalis* ATCC 29212, *Bacillus subtilis* IC 12488) bacterial as well as fungal (*Candida krusei* 963) strains. The obtained results suggested that the antimicrobial activity of IO-NPs is dependent on the metallic ions concentrations and on the microbial growth state, either planktonic or adherent. The obtained IO-NPs exhibited no cytotoxic effect on HeLa cells at the active antimicrobial concentrations.

## 1. Introduction

During the last decade, there has been an increasing interest in developing and understanding of matter at nanometric scale [1, 2]. The progress made in the area of nanotechnology in the last years has allowed the scientists to develop and characterize materials with outstanding properties and nanometric sizes [3]. The field of nanomaterials has been the centre of attention in the scientific community due to the unique and remarkable properties exhibited by materials when studied at nanometric scale. Recent studies state that inorganic materials are the core of future developments in industrial and technological applications [4]. During the past few years, the most studied materials were the ones with magnetic behaviour due to their promising applications in areas such as magnetic data storage [5], gas sensors [6–8], tunnelling magneto-resistance (TMR) [9, 10], ferrofluid, targeted drug delivery, contrast agents in magnetic resonance imaging [11], hyperthermia, magnetic field assisted radionuclide therapy [12] as well as magnetically separable absorbents [13]. Amongst materials with magnetic properties, iron oxide nanoparticles are most suitable for biomedical applications due to their proven biocompatibility. Magnetite and maghemite, the most common iron oxide nanoparticles, have been the subject of intensive studies because at nanometric scale they exhibit unique physical and chemical particularities [14].

Due to the increased resistance to existing antibiotics of various microorganisms, many researchers have turned towards engineered nanoparticles for finding a solution.

The ability of pathogenic bacteria and fungi to resist antimicrobial agents, by genetic mechanisms and by phenotypic resistance due to the biofilm growing state, has emerged in the recent years and became a major health problem. Recent studies reported various metal nanoparticles to exhibit antimicrobial effects [15]. Iron oxide nanoparticles, due to their small size, superparamagnetic properties and controllable parameters, can interact directly with various microorganisms without posing a risk for human body. These nanoparticles can interact directly with the microbial cells causing damage to the envelope and thus rendering the bacterial cell defenceless or, in some cases, disrupting the metabolic functions and causing the destruction of the cell [16].

Magnetic iron oxide nanoparticle are increasingly being developed for use in research and biomedical applications, such as targeted transport of antimicrobial drug. The fundamental understanding on the influence of magnetic iron oxide nanoparticle on cellular growth and functions is very important for further biological applications. The comparative study on growth of different bacteria the influence of magnetic iron oxide were revealed the effect of magnetic iron oxide nanoparticle on bacterial growth.

This study focuses on the investigation of the antimicrobial behavior of iron oxide nanoparticles (IO-NPs) prepared by an adapted co-precipitation method [17–21] and on the analysis of M-H hysteresis loops at room temperature. Transmission electron microscopy studies have been conducted to obtain information about size, structure and morphology of the fabricated IO-NPs. The antimicrobial activity of the IO-NPs was investigated by qualitative and quantitative assays and their cytotoxic effect was assessed on HeLa cells. In this study, the IO-NPs were tested in aqueous suspension against a large spectrum of microbial strains, both by antimicrobial susceptibility standard methods (agar diffusion and minimal inhibitory concentration assay) as well as by methods aimed to investigate the efficiency of IO-NPs against biofilm embedded cells, which are much more resistant to different stress factors, including antimicrobials, than their planktonic counterparts.

## 2. Experimental Section

*2.1. Materials.* Ferrous chloride tetrahydrate (FeCl$_2$·4H$_2$O), ferric chloride hexahydrate (FeCl$_3$·6H$_2$O), natrium hydroxide (NaOH), and hydrochoric acid (HCl) were purchased from Merck. Deionized water was used in the synthesis of nanoparticles and for rinsing of clusters.

*2.2. Synthesis of Iron Oxide Ferrofluid and Characterization.* The synthesis of iron oxide ferrofluid was carried out as reported in other papers [22]. Transmission electron microscopy (TEM) images for these samples were recorded using a FEI Tecnai 12 equipped with a low dose digital camera from Gatan. The specimen for TEM imaging was prepared by ultramicrotome to get thin section of about 60 nm. The powder was embedded in an epoxy resin (polaron 612) before microtomy. The magnetic properties of the samples were

measured using a superconducting quantum interference device (MPMS magnetometer) at room temperature.

*2.3. Cytotoxicity Assay.* Quantification of cell viability was performed using propidium iodide (PI) and fluorescein diacetate (FdA). Briefly, $5 \times 10^4$ HeLa cells were seeded in each well of a plate with 24 wells and after 24 h were treated with 10 $\mu$L of Fe$^{2+}$/Fe$^{3+}$ of 0.03 final concentration. The effects on cell viability were evaluated after 24 h by adding 100 $\mu$L PI (0.1 mg/mL) and 100 $\mu$L FdA (0.1 mg/mL) and fluorescence was quantified using Observer D1 Carl Zeiss microscope. All cells from several fields were counted and cell viability was established by the ratio between viable (green) and dead cells (red) [23].

*2.4. The In Vitro Antibacterial and Antibiofilm Activity*

*Assessment of the Antimicrobial and Antipathogenic Activity of the New Oxides.* The *in vitro* qualitative screening of the antimicrobial activity was carried out by an adapted agar diffusion technique using a bacterial suspension of 0.5 McFarland density obtained from 24 hour cultures [24, 25]. The antimicrobial activity of the IO-NPs was tested against Gram-negative (*Pseudomonas aeruginosa* 1397, *Escherichia coli* ATCC 25922), Gram-positive (*Enterococcus faecalis* ATCC 29212, *Bacillus subtilis* (IC 12488) bacterial as well as fungal (*Candida krusei* 963) strains. The microbial strains identification was confirmed by aid of VITEK II automatic system. VITEK cards for identification and susceptibility testing (GNS-522) were inoculated and incubated according to the manufacturer's recommendations. IO-NPs were tested starting with a concentration of 10 mg/mL.

*Qualitative Screening of the IO-NPs Antimicrobial Activity.* A volume of 10 $\mu$L of each tested IO-NPs sample of 10 mg/mL concentration was spotted on Muller Hinton agar for bacteria and Yeast Peptone Glucose (YPG) agar for fungi, previously seeded with the microbial inocula of 0.5 MacFarland density. The inoculated plates were incubated for 24 h at 37°C. The antimicrobial activity was assessed by measuring the growth inhibition zones diameters expressed in mm [26]. Following the results of the qualitative screening, only the microbial strains proving to be susceptible have been further tested in the quantitative assay.

The quantitative assay of the minimal inhibitory concentration (MIC, $\mu$g/mL) was based on liquid medium two-fold microdilutions and performed in 96 multi-well plates. For this purpose, serial binary dilutions of the tested compounds (ranging between 5 and 0.01 $\mu$g/mL) were performed in a 200 $\mu$L volume of nutrient broth (for bacteria)/YPG (for fungi) and each well was seeded with 20 $\mu$L microbial inocula of 0.5 McFarland density. The plates were incubated for 24 h at 37°C, the antimicrobial effect being assessed by measuring the absorbance of the obtained cultures at 620 nm [26]. The lower absorbance value was, the more intensive the antimicrobial effect is.

The antibiofilm activity of the IO-NPs was tested by the microtiter method. For this purpose, the microbial strains
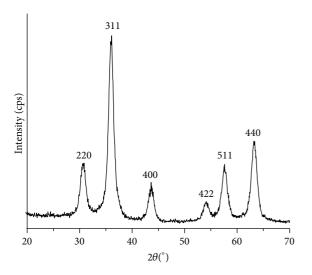
FIGURE 1: XRD patterns of maghemite $\gamma$-Fe$_2$O$_3$ nanoparticles obtained by coprecipitation method.

have been grown in the presence of two-fold serial dilutions of the tested compounds (ranging between 5 and 0.01 μg/mL), performed in liquid nutrient broth/YPG, distributed in 96-well plates and incubated for 24 hours at 37°C. At the end of the incubation period, the plastic wells were emptied, washed three times with phosphate buffered saline (PBS), fixed with cold methanol and stained with 1% violet crystal solution for 30 minutes. The biofilm formed on plastic wells was resuspended in 30% acetic acid. The intensity of the colored suspensions was assessed by measuring the absorbance at 492 nm [26–28]. The lower absorbance value was, the more intensive the antibiofilm effect was considered.

## 3. Results and Discussion

Figure 1 shows the XRD patterns of the iron oxide particles. The $2\theta$ values of the peaks are compared with the standard data for $\gamma$-Fe$_2$O$_3$. Diffraction peaks at (220), (311), (400), (422), (511) and (440) are readily recognized from the XRD pattern in the sample. The XRD peaks of iron oxide nanoparticles (Figure 1) can be indexed into the spinel cubic lattice type with a lattice of 0.835 nm. This value of lattice parameter is in agreement with *the values of the standard data (JCPDS no. 4-755)*. The refinement of XRD spectra indicated that no other phases except the maghemite are detectable. The XRD showed a finite broadening of the diffraction lines. The particle size calculated using the Scherer [29] formula was estimated at around 7.7 nm.

Figure 2(a) shows TEM picture of iron oxide nanoparticles (IO-NPs), clearly showing that the product is entirely composed of crystals with a relatively uniform, spherical morphology. Grain size distribution was determined by measuring the mean diameter, $D$, of about 500 particles on the micrographs (Figure 2(c)). TEM images indicate a very uniform size distribution of iron oxide nanoparticles. The average grain size of the monodisperse nanoparticles is $7 \pm 0.2$ nm. Figure 2(b) also shows the selected area electron

diffraction (SAED) pattern recorded from an area containing a large number of nanoparticles and high-resolution TEM picture. The rings in the SAED pattern can be indexed as the (220), (311), (400), (422), (511) and (440) reflections of the cubic maghemite in agreement with the XRD results.

The magnetic properties of the prepared IO-NPs were monitored by measuring the hysteresis loops at a temperature of 300 K. Magnetization curves (M-H loop) for the magnetic IO-NPs measured at room temperature were presented in Figure 3. At the maximum applied magnetic field of 10 kOe the magnetization did not reach saturation no hysteresis loops can be observed (no remanent magnetization and zero coercivity fields) [30, 31]. This behavior indicated that the IO-NPs were superparamagnetic at room temperature with a calculated saturation magnetization of 18.1 emu/g. The iron oxide nanoparticles sample shows a saturation magnetization at lower than the reported values for the saturation magnetization of bulk maghemite ($\gamma$-Fe$_2$O$_3$) [32]. This trend could be attributed to the particles sizes effect. The magnetic nanoparticles are so small that they may be considered to have a single magnetic domain [33]. In his studies, Hergt et al., showed that the saturation magnetizations, Ms, decreases with decreasing particle size [34]. Analysis the hysteresis loops of the IO-NPs, at 300 K confirms average size and particle size distribution of IO-NPs already obtained from TEM and XRD analyses. Combination of magnetic properties and antimicrobial features of iron oxide nanoparticles, designates these nanoparticles for exploitation in biomedical applications, such as targeted transport of antimicrobial drug. With regard to their unique magnetic and antibacterial properties, the iron oxide nanoparticles can be exploited at lower concentrations so that their toxic effect on human cells to be minimized.

A great advantage of the tested compound is that they are not cytotoxic at the active concentrations, as reveal by the cytotoxicity assay, demonstrating no cytotoxic effect of the IO-NPs (Figure 4).

The microbial species of clinical interest often involved in biofilm associated diseases are belonging to a very large spectrum, from the Gram positive (*S. epidermidis* and *S. aureus*), and Gram negative (*P. aeruginosa*, *E. coli*) bacterial strains to different members of the *Candida* genus [35]. The understanding of microbial infections related to the biofilm development on tissues or indwelling devices was possible by using different qualitative and quantitative *in vitro* specific assays. In our study we have also used both assays for studying the susceptibility of microbial cells grown in suspension, known as planktonic cells, as well as of those developed in biofilms, called adherent or sessile cells.

The antimicrobial activity of the IO-NPs has been studied on strains belonging to common bacterial pathogens, that is, the Gram-negative, *P. aeruginosa*, *E. coli*, Gram-positive *E. faecalis*, *B. subtilis,* and a yeast strain of *C. krusei*.

After the qualitative screening, the microbial strains which proved to be susceptible to the tested nanoparticles have been investigated in the quantitative assay for establishing the MIC value. The highest tested concentration was of 5 mg/mL, because at higher concentrations, the colored iron oxide suspension would have interfered with the reading
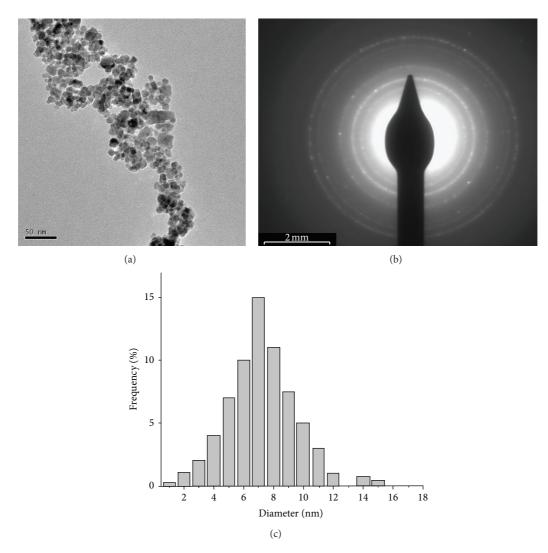
(a)



(b)



(c)

FIGURE 2: Bright field TEM picture showing a homogeneous distribution of iron oxide nanoparticles (a), SAED pattern from a region including a large number of nanoparticles (b), and size distribution of IO-NPs (c).
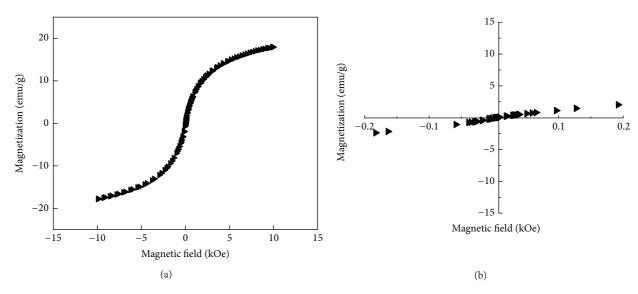


(a)



(b)

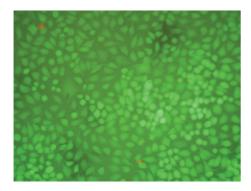FIGURE 3: M-H curves of iron oxide nanoparticles at room temperature (a). The low field parts (b).

FIGURE 4: Fluorescence microscopy image revealing the absence of the cytotoxic effect on HeLa cells (no dead cell stained in red) after 24 h treatment with 200 $\mu$L of iron oxide ($\times$100).
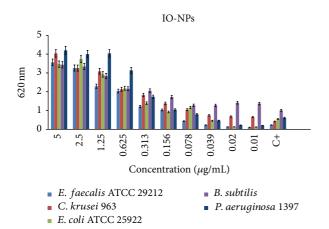


FIGURE 5: The quantitative assay of the inhibitory effect of the IO-NPs on different microbial strains, quantified by the absorbance measurements at 620 nm. C = positive control, represented by the microbial culture grown in the absence of IO-NPs.

of the absorbance values at 620 nm. The quantitative assay showed that the IO-NPs generally stimulated the growth of all microbial cells in suspension from the highest tested concentrations of 5 mg/mL to 0.039 mg/mL, as demonstrated by the absorbance measurements at 620 nm of the obtained cultures (Figure 5).

A bactericidal effect has been observed at low IO-NPs concentrations, that is, from 0.039 to 0.01 mg/mL against *E. faecalis* ATCC 29212 and *P. aeruginosa* 1397, from 0.02 to 0.01 against *E. coli* ATCC 25922. The IO-NPs, irrespective to the tested concentration exhibited no inhibitory effect on *C. krusei 963* and *B. subtilis* IC 12488 growth.

Metal oxide nanoparticles, including magnetite, have been proved to have inherent antimicrobial properties, which are enhanced, or occur, when the materials are in the nanometer size and in relation to surface area [36]. Since nanoparticles can be smaller in size than bacterial pores, they have a unique ability of crossing the cell membrane, disrupting its function or interfering with nucleic acid or protein synthesis [37]. Our study demonstrated that IO-NPs are rather exhibiting a stimulatory effect on the microbial

growth especially at high concentrations. The stimulatory effect of iron oxide nanoparticles on the microbial growth was also reported by other authors, that is, on *E. coli* [38] or *E. coli*, *P. aeruginosa* and *E. faecalis*, *C. albicans* [39]. These results could be explained by the ability of the microbial strains to use the iron oxide as a metabolic source of iron, which is known to positively regulate the microbial growth rate and other physiological processes [40].

However, at lower concentrations ranging from 39 to 10 $\mu$g/mL, they inhibited the growth of *E. faecalis*, *P. aeruginosa* and *E. coli* strains. Our results come into agreement with other studies showing that iron oxide nanoparticles substantially inhibited the growth of *E. coli* and *S. aureus* at concentrations comparable with those used in our study, from 10 to 100 $\mu$g/mL [41]. $Fe_2O_3$ nanoparticles have been shown to exhibit the least bactericidal activity, when compared with other metal oxides, like ZnO or CuO [42]. The antibacterial activity of composite nanoparticles containing iron oxide, zinc oxide and zinc ferrite phases has been shown to be proportional with the weight ratio [Zn]/[Fe] of the composite nanoparticle, on *Staphylococcus aureus* and *Escherichia coli*, so the lowest the iron concentration, the most intensive the antimicrobial activity [37].

Studies in the last decades on microbial adherence to different substrata led to the conclusion that the survival of microorganisms in the natural habitats, including medical ecosystems, is dependent on their capacity to adhere to different surfaces/substrata and form biofilms. A biofilm is a sessile microbial community composed of cells embedded in a matrix of extracellular polymeric substances attached to a substratum or interface. The matrix is primarily of microbial origin and the cells encased in this matrix present a modified phenotype, being metabolically more efficient and well protected, exhibiting resistance to different stress factors, including host defense mechanisms and antibiotics [43].

The quantitative assay of the inhibitory effect of IO-NPs on biofilms developed on the inert substratum by different microbial strains, quantified by the absorbance measurements at 490 nm are presented in Figure 6. The highest tested concentration (i.e., 5 mg/mL) exhibited a strong stimulatory effect on the biofilm development by all tested microbial strains, this effect drastically decreasing in case of the other tested concentrations (Figure 6). The tested IO-NPs exhibited only a slight antibiofilm activity for the same strains susceptible in the planktonic state, that is, *E. faecalis 29212* (0.625 to 0.01 mg/mL), *P. aeruginosa 1397* (2.5 to 0.01 mg/mL), and *E. coli* ATCC 25922 (0.156 to 0.01 mg/mL) strains (Figure 6). Comparing the range of active concentrations of IO-NPs against planktonic and respectively adherent strains, it could be observed that the antibiofilm activity of the obtained nanoparticles is maintained on a wider range of concentrations.

## 4. Conclusions

Iron oxide nanoparticles were synthesized by a facile and rapid coprecipitation method. The prepared IO-NPs were characterized by various techniques. The TEM images show
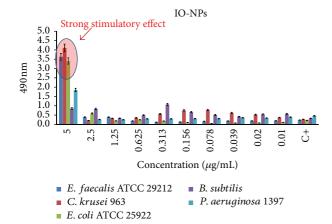
FIGURE 6: The quantitative assay of the inhibitory effect of IO-NPs on biofilms developed on the inert substratum by different microbial strains, quantified by the absorbance measurements at 490 nm.

well-crystallized magnetic IO-NPs with average size of $7 \pm 0.2$ nm and narrow size distributions without particle agglomeration. The hysteresis loop of IO-NPs demonstrates a superparamagnetic behavior. The IO-NPs exhibited a strong stimulatory effect directly correlated with high concentrations of the tested nanoparticles, both on the growth of microbial strains in suspension and in adherent state, probably due to the potential of these strains to use the iron oxide as a source of iron ions required for the microbial metabolism and pathogenicity. However, the tested iron oxide nanoparticles inhibited on a certain range of concentrations the ability of *E. faecalis*, *P. aeruginosa,* and *E. coli* strains to grow, both in suspension and in biofilm state, results demonstrating their potential use in the design of antibacterial and antibiofilm materials and surfaces, for biomedical applications, exhibiting also the great advantage of reduced cytotoxicity on eukaryotic host cells and tissues. The combination of magnetic properties and antimicrobial features designates the iron oxide nanoparticles to be possibly used in applications such as clinical infections and local antimicrobial therapy. On the other hand, these nanoparticles could be used for targeted transport of an antimicrobial agent and its subsequent removal by means of an external magnetic field.

## Acknowledgments

## References

[1] G. Nicoara, D. Fratiloiu, M. Nogues, J. L. Dormann, and F. Vasiliu, "Ni-Zn ferrite nanoparticles prepared by ball milling," *Materials Science Forum*, vol. 235-238, no. 1, pp. 145–150, 1997.

[2] D. Prodan, C. Chanéac, E. Tronc et al., "Adsorption phenomena and magnetic properties of $\gamma$-Fe$_2$O$_3$ nanoparticles," *Journal of Magnetism and Magnetic Materials*, vol. 203, no. 1-3, pp. 63–65, 1999.

[3] D. Prodan, V. V. Grecu, M. N. Grecu, E. Tronc, and J. P. Jolivet, "Electron spin resonance in $\gamma$-Fe$_2$O$_3$ nanoparticles dispersed in a polymer matrix," *Measurement Science and Technology*, vol. 10, no. 9, pp. L41–L43, 1999.

[4] A. Figuerola, R. Di Corato, L. Manna, and T. Pellegrino, "From iron oxide nanoparticles towards advanced iron-based inorganic materials designed for biomedical applications," *Pharmacological Research*, vol. 62, no. 2, pp. 126–143, 2010.

[5] M. L. Yan, X. Z. Li, L. Gao et al., "Fabrication of nonepitaxially grown double-layered FePt:C/FeCoNi thin films for perpendicular recording," *Applied Physics Letters*, vol. 83, no. 16, pp. 3332–3334, 2003.

[6] D. Predoi, C. S. Ciobanu, M. Radu et al., "Hybrid dextran-iron oxide thin films deposited by laser techniques for biomedical applications," *Materials Science and Engineering C*, vol. 32, no. 2, pp. 296–302, 2012.

[7] O. K. Tan, W. Zhu, Q. Yan, and L. B. Kong, "Size effect and gas sensing characteristics of nanocrystalline $_x$SnO$_2$-(1-$x$)$\alpha$-Fe$_2$O$_3$ ethanol sensors," *Sensors and Actuators B*, vol. 65, no. 1, pp. 361–365, 2000.

[8] E. Andronescu, M. Costache, C. S. Ciobanu, A. M. Prodan, and D. Predoi, "Biocompatibility studies of iron-oxide-dextrin thin films," *Revista de Chimie*, vol. 61, no. 10, pp. 925–928, 2010.

[9] Y. Peng, C. Park, and D. E. Laughiin, "Fe$_3$O$_4$ thin films sputter deposited from iron oxide targets," *Journal of Applied Physics*, vol. 93, no. 10, pp. 7957–7959, 2003.

[10] C. S. Ciobanu, E. Andronescu, L. Pall, S. L. Iconaru, E. Gyorgy, and D. Predoi, "Physico-chemical properties of iron-oxide-dextnn thin films," *Revista de Chimie*, vol. 61, no. 12, pp. 1207–1211, 2010.

[11] M. Bystrzejewski, A. Huczko, and H. Lange, "Arc plasma route to carbon-encapsulated magnetic nanoparticles for biomedical applications," *Sensors and Actuators B*, vol. 109, no. 1, pp. 81–85, 2005.

[12] Z. Sun, L. Wang, P. Liu et al., "Magnetically motive porous sphere composite and its excellent properties for the removal of pollutants in water by adsorption and desorption cycles," *Advanced Materials*, vol. 18, no. 15, pp. 1968–1971, 2006.

[13] A. R. Jalilian, A. Panahifar, M. Mahmoudi, M. Akhlaghi, and A. Simchi, "Preparation and biological evaluation of [$^{67}$Ga]-labeled-superparamagnetic nanoparticles in normal rats," *Radiochimica Acta*, vol. 97, no. 1, pp. 51–56, 2009.

[14] Y. Xiong, J. Ye, X. Gu, and Q. Chen, "Synthesis and magnetic properties of iron oxide nanoparticles/C and $\alpha$-Fe/iron oxide nanoparticles/C composites," *Journal of Magnetism and Magnetic Materials*, vol. 320, no. 3-4, pp. 107–112, 2008.

[15] M. P. Moralesa, O. Bomati-Miguela, R. Perez de Alejob, J. Ruiz-Cabellob, S. Veintemillas-Verdaguera, and K. O'Gradyc, "Contrast agents for MRI based on iron oxide nanoparticles prepared by laser pyrolysis," *Journal of Magnetism and Magnetic Materials*, vol. 266, pp. 102–109, 2003.

[16] F. Furno, K. S. Morley, B. Wong et al., "Silver nanoparticles and polymeric medical devices: a new approach to prevention of infection?" *Journal of Antimicrobial Chemotherapy*, vol. 54, no. 6, pp. 1019–1024, 2004.

[17] R. Massart, "Magnetic fluids and process for obtaining them," US Patent 4329241, 1982.

[18] R. Massart, "Preparation of aqueous magnetic liquids in alkaline and acidic media," *IEEE Transactions on Magnetics*, vol. 17, no. 2, pp. 1247–1248, 1981.

[19] R. Massart, J. Roger, and V. Cabuil, "New trends in chemistry of magnetic colloids: polar and non polar magnetic fluids, emulsions, capsules and vesicles," *Brazilian Journal of Physics*, vol. 25, no. 2, pp. 135–141, 1995.

[20] D. Predoi and C. M. Valsangiacom, "Thermal studies of magnetic spinel iron oxide in solution," *Journal of Optoelectronics and Advanced Materials*, vol. 9, no. 6, pp. 1797–1799, 2007.

[21] D. Zins, V. Cabuil, and R. Massart, "New aqueous magnetic fluids," *Journal of Molecular Liquids*, vol. 83, no. 1-3, pp. 217–232, 1999.

[22] C. S. Ciobanu, S. L. Iconaru, E. Gyorgy et al., "Biomedical properties and preparation of iron oxide-dextran nanostructures by MAPLE technique," *Chemistry Central Journal*, vol. 6, p. 17, 2012.

[23] A. M. Grumezescu, E. Andronescu, A. Ficai, C. Bleotu, and M. C. Chifiriuc, "Chitin based biomaterial for antimicrobial therapy: fabrication, characterzation and in vitro profile based intercation with eukaryotic and prokaeryotic cells," *Biointerface Research in Applied Chemistry*, vol. 2, p. 446, 2012.

[24] A. M. Grumezescu, E. Andronescu, A. Ficai et al., "Magnetic nanofluid with antitumoral properties," *Letters in Applied NanoBioScience*, vol. 1, p. 56, 2012.

[25] A. M. Grumezescu, A. Holban, E. Andronescu, A. Ficai, C. Bleotu, and M. C. Chifiriuc, "Microbiological applications of a new water dispersible magnetic nanobiocomposite," *Letters in Applied NanoBioScience*, vol. 4, p. 83, 2012.

[26] C. Saviuc, A. M. Grumezescu, C. M. Chifiriuc et al., "Hybrid nanosystem for stabilizing essential oils in biomedical applications," *Digest Journal of Nanomaterials and Biostructures*, vol. 6, no. 4, pp. 1657–1666, 2011.

[27] C. Saviuc, A. M. Grumezescu, A. Holban et al., "Phenotypical studies of raw and nanosystem embedded Eugenia carryophyllata buds essential oil antibacterial activity on Pseudomonas aeruginosa and Staphylococcus aureus strains," *Biointerface Research in Applied Chemistry*, vol. 1, no. 3, pp. 111–118, 2011.

[28] C. Saviuc, I. Marinas, A. M. Grumezescu et al., "Phytochemical composition of the fennel fruits essential oil and its influence on prokariotic cells growth and pathogenic features," *Biointerface Research in Applied Chemistry*, vol. 2, p. 300, 2012.

[29] R. M. Cornell and U. Schertmann, *Iron Oxides in the Laboratory: Preparation and Characterisation*, VCH, Weinheim, Germany, 1991.

[30] K. V. P. M. Shafi, A. Gedanken, R. Prozorov, and J. Balogh, "Sonochemical preparation and size-dependent properties of nanostructured $CoFe_2O_4$ particles," *Chemistry of Materials*, vol. 10, no. 11, pp. 3445–3450, 1998.

[31] R. Vijayakumar, Y. Koltypin, I. Felner, and A. Gedanken, "Sonochemical synthesis and characterization of pure nanometer-sized $Fe_3O_4$ particles," *Materials Science and Engineering A*, vol. 286, no. 1, pp. 101–105, 2000.

[32] E. du Tremolet deLacheisserie, D. Gignoux, and M. Schlenker, *Magnetism: Materialsandapplications*, Springer, New York, NY, USA, 2005.

[33] D. H. Han, J. P. Wang, and H. L. Luo, "Crystallite size effect on saturation magnetization of fine ferrimagnetic particles," *Journal of Magnetism and Magnetic Materials*, vol. 136, no. 1-2, pp. 176–182, 1994.

[34] R. Hergt, W. Andrae, C. G. d'Ambly et al., "Physical limits of hyperthermia using magnetite fine particles," *IEEE Transactions on Magnetics*, vol. 34, no. 5, pp. 3745–3754, 1998.

[35] V. Lazăr and M. C. Chifiriuc, "Medical significance and new therapeutical strategies for biofilm associated infections," *Roumanian Archives of Microbiology & Immunology*, vol. 69, no. 3, pp. 125–138, 2010.

[36] E. Taylor and T. J. Webster, "Reducing infections through nanotechnology and nanoparticles," *International Journal of Nanomedicine*, vol. 6, pp. 1463–1473, 2011.

[37] T. Gordon, B. Perlstein, O. Houbara, I. Felner, E. Banin, and S. Margel, "Synthesis and characterization of zinc/iron oxide composite nanoparticles and their antibacterial properties," *Colloids and Surfaces A*, vol. 374, no. 1-3, pp. 1–8, 2011.

[38] S. Nath, C. Kaittanis, V. Ramachandran, N. S. Dalal, and J. M. Perez, "Synthesis, magnetic characterization, and sensing applications of novel dextran-coated iron oxide nanorods," *Chemistry of Materials*, vol. 21, no. 8, pp. 1761–1767, 2009.

[39] M. Singh, S. Singh, S. Prasad, and I. S. Gambhir, "Nanotechnology in medicine and antibacterial effect of silver nanoparticles," *Digest Journal of Nanomaterials and Biostructures*, vol. 3, pp. 115–122, 2008.

[40] A. Azam, A. S. Ahmed, M. Oves, M. S. Khan, S. S. Habib, and A. Memic, "Antimicrobial activity of metal oxide nanoparticles against Gram-positive and Gram-negative bacteria: a comparative study," *International Journal of Nanomedicine*, vol. 7, pp. 6003–6009, 2012.

[41] S. A. Mahdy, Q. J. Raheed, and P. T. Kalaichelvan, "Antimicrobial activity of zero-valent iron nanoparticles," *International Journal of Modern Engineering Research*, vol. 2, no. 1, pp. 578–581, 2012.

[42] A. K. Horst, "Antimicrobial effects of metal oxide nanoparticles," The NNIN REU Research Accomplishmnents Biological Applicantions, 2009.

[43] C. Chifiriuc, V. Lazăr, C. Bleotu et al., "Bacterial adherence to the cellular and inert substrate in the presence of $CoFe_2O_4$ and $Fe_3O_4$/oleic acid-core/shell," *Digest Journal of Nanomaterials and Biostructures*, vol. 6, no. 1, pp. 37–42, 2011.

*Research Article*

# Z-Contrast STEM Imaging of Long-Range Ordered Structures in Epitaxially Grown CoPt Nanoparticles

## Kazuhisa Sato,[1] Keigo Yanajima,[2] and Toyohiko J. Konno[1]

[1] *Institute for Materials Research, Tohoku University, 2-1-1 Katahira, Aoba-ku, Sendai 980-8577, Japan*
[2] *Department of Materials Science, Tohoku University, 6-6 Aramaki, Aoba-ku, Sendai 980-8579, Japan*

Correspondence should be addressed to Kazuhisa Sato; ksato@imr.tohoku.ac.jp

We report on atomic structure imaging of epitaxial $L1_0$ CoPt nanoparticles using chemically sensitive high-angle annular dark-field scanning transmission electron microscopy (HAADF-STEM). Highly ordered nanoparticles formed by annealing at 973 K show single-variant structure with perpendicular *c*-axis orientation, while multivariant ordered domains are frequently observed for specimens annealed at 873 K. It was found that the (001) facets of the multivariant particles are terminated by Co atoms rather than by Pt, presumably due to the intermediate stage of atomic ordering. Coexistence of single-variant particles and multivariant particles in the same specimen film suggests that the interfacial energy between variant domains be small enough to form such structural domains in a nanoparticle as small as 4 nm in diameter.

## 1. Introduction

Recent developments in ultrahigh-density magnetic storage technology rely on novel recording media with high magnetocrystalline anisotropy energy (MAE) together with high-performance giant magnetoresistive (GMR) heads [1–4]. For such a purpose, CoPt alloy nanoparticles with the $L1_0$-type ordered structure are one of the candidate materials [5, 6]. The hard magnetic property of this alloy is attributed to the tetragonal $L1_0$-type ordered structure with a high MAE [7]: the reported value is as high as $4.1 \times 10^6$ J/m$^3$ for a single-crystal bulk $L1_0$-$Co_{50}Pt_{50}$ alloy [8]. The $L1_0$-type ordered structure is composed of alternate stacking of Co(001) and Pt(001) atomic planes in the [001] direction (*c*-axis). Since MAE is dependent on the long-range order (LRO) parameter [9, 10], atomic ordering and the stability of the ordered phase are key issues for hard magnetic properties of the $L1_0$-type magnetic alloy nanoparticles [11]. To extract chemical information directly related to the LRO in the atomic scale resolution, atomic number (*Z*) contrast imaging by high-angle annular dark-field scanning transmission electron microscopy (HAADF-STEM) is quite useful. One of the authors demonstrated the detection of nanometer-sized local

atomic order in FePd nanoparticles by *Z*-contrast at an intermediate stage of the ordering process [12]. To date, detection of atomic ordering has been reported for several ordered alloy nanoparticles produced by different fabrication methods [13–16]. However, there is no report on the *Z*-contrast imaging of highly ordered epitaxial $L1_0$ CoPt nanoparticles so far.

In this study, we hence intend to characterize the atomic structure of highly ordered $L1_0$ CoPt nanoparticles using chemically sensitive atomic resolution HAADF-STEM. Large atomic number difference between Co ($Z = 27$) and Pt ($Z = 78$) enables clear visualization of atomic ordering in bimetallic CoPt nanoparticles; that is, *Z*-contrast makes the direct interpretation of image contrasts possible due to incoherent imaging nature [17].

## 2. Experimental

CoPt nanoparticles were fabricated by sequential electron-beam deposition of Pt and Co onto NaCl(001) substrates with a base pressure of $9 \times 10^{-7}$ Pa [18]. The substrate temperature was kept at 653 K during the deposition. A quartz thickness monitor located near the substrate stage in the vacuum chamber was used to estimate and control the nominal
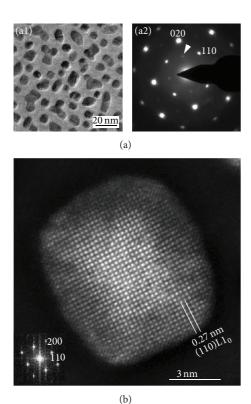
(a)



(b)

Figure 1: (a) BF-TEM image and corresponding SAED pattern of CoPt nanoparticles after annealing at 973 K for 100 min (sample no. 1). (b) HAADF-STEM image of a CoPt nanoparticle with the $L1_0$-type ordered structure. FFT pattern is shown in the inset.

thickness of deposited layers. We first deposited Pt to partially cover the substrate, which resulted in the formation of $\langle 100 \rangle$ oriented Pt islands. Next, Co was deposited onto the substrate with Pt followed by the deposition of an amorphous (a-) $Al_2O_3$ protective layer. In this sequential deposition process, Pt nanoparticles act as nucleation sites for Co nanoparticles [18, 19]. The deposition rates of Pt, Co, and $Al_2O_3$ were, respectively, 0.04, 0.2, and 0.3 nm/min. Nominal thickness and other detailed conditions for the sample preparation are listed in Table 1. After the deposition of $Al_2O_3$, the specimen films were then heated inside the vacuum chamber at 823 K for 3 h to promote island growth of nanoparticles. A part of the specimen film was then removed from the NaCl substrate by the immersion into distilled water, and floating film was mounted onto a Mo grid with a holey carbon film for TEM observation. To obtain highly ordered nanoparticles, we carried out high-temperature postdeposition annealing of the as-deposited film on a Mo grid at 873 or 973 K in a high-vacuum furnace ($<2 \times 10^{-5}$ Pa). Cooling rate after the heat treatment was set to be less than 3 K/min in order to ensure atomic ordering in small nanoparticles [18, 20]. STEM images were obtained using an FEI TITAN80-300 (STEM) operating at 300 kV with a field emission gun. We set beam convergence to be 10 mrad in half angle, taking into account the spherical aberration coefficient (1.2 mm) of the prefield of objective lens. Z-contrast images were acquired by using a HAADF-detector (Fischione model 3000) with detector

half angles between 60 and 210 mrad. STEM images were simulated using QSTEM software [21]. Alloy compositions were analyzed by energy dispersive X-ray spectrometer (EDS) attached to the TEM.

## 3. Results and Discussion

Figure 1(a) shows a bright-field (BF) TEM image and a corresponding selected area electron diffraction (SAED) pattern of the Co-55 at %Pt nanoparticles after annealing at 973 K for 100 min (sample no. 1). Note that the annealing temperature of 973 K is 100 K lower than the order-disorder transformation temperature for the corresponding bulk alloy (Co-55 at %Pt) [22]. CoPt nanoparticles with the $L1_0$-type ordered structure were formed as epitaxial islands on the NaCl(001) substrate. The orientation relationships between CoPt and NaCl(001) is $\langle 100 \rangle_{\text{CoPt}} \parallel \langle 100 \rangle_{\text{NaCl}}, \{001\}_{\text{CoPt}} \parallel \{001\}_{\text{NaCl}}$ [18]. Strong 110 superlattice reflections of the $L1_0$ ordered structure indicates preferential growth of nanoparticles with the crystallographic $c$-axis oriented normal to the substrate surface (c-domain) with a high degree of order. In addition, the arrowhead indicates 001 superlattice reflection from nanoparticles with the $c$-axis oriented parallel to the substrate surface (a or b domain), while its intensity is quite weak compared to that of the 110 reflection.

Figure 1(b) shows a high-resolution HAADF-STEM image of a 10 nm sized $L1_0$ CoPt nanoparticle with the $c$-axis oriented normal to the film plane. Fast Fourier transform (FFT) pattern is also shown in the inset. Periodic arrangement of atoms by atomic order can be seen clearly as bright contrasts. It is obvious that the particle is single crystal as indicated by clear-cut (110) superlattice atomic planes which spread over the particle. In this specimen film, most of the particles observed were single crystal. Image contrasts of the (110) superlattice fringes are lower in the peripheral regions than those in the central part of the nanoparticle. To clarify the origin of such contrast variation, we performed image simulation using a model cluster.

Figure 2(a) shows a structure model and a simulated HAADF-STEM image of a fully ordered CoPt nanoparticle. The model is a truncated octahedron (TO) composed of 8000 atoms, 5.7 nm in width and 5.5 nm in height. As seen, contrast variation from the particle center to the {111} or {100} facets is reproduced in the simulated image of the fully ordered CoPt nanoparticle. Figure 2(b) shows intensity profiles of the simulated images measured in the [100] direction (b1) and [1$\bar{1}$0] direction (b2). Intensity degradation towards {111} facet (B-B$'$) is prominent compared to that of {100} (A-A$'$) due to the thickness reduction. Thus, image simulation revealed that experimentally observed degradation of image contrast can be attributed to the thickness reduction in the peripheral region due to particle shape. This result indicates that HAADF-STEM image intensity is also sensitive to thickness variation in addition to atomic number. Similar degradation of image contrast has been observed in high-resolution TEM (HRTEM) images to a lesser degree compared to Z-contrast [18].

Figure 3(a) shows another example of HAADF-STEM image of a highly ordered CoPt nanoparticle after annealing

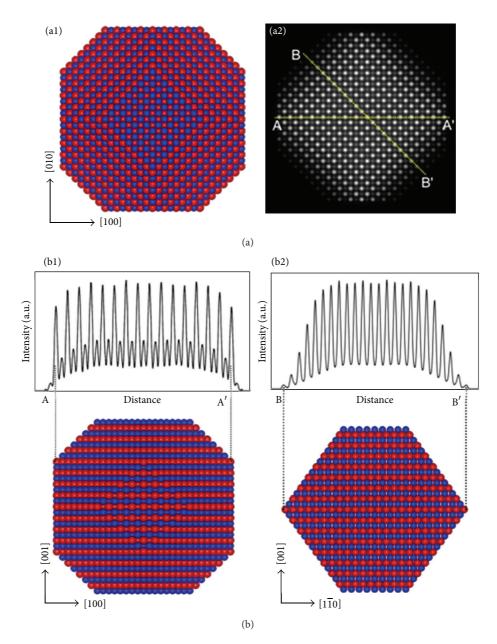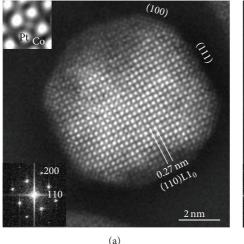(a1)

(a2)

(a)

(b1)

(b2)

(b)

FIGURE 2: (a) A structure model (truncated octahedron) and a simulated HAADF-STEM image. The beam incidence is [001]. (b) Intensity profiles of simulated images measured in the [100] (b1) and [1$\bar{1}$0] directions (b2).

TABLE 1: Nominal thickness, alloy composition, annealing condition, and particle size for CoPt nanoparticles grown on NaCl(001) single-crystal substrates.

| Sample no. | Nominal thickness | Composition | Annealing (cooling rate) | Particle size ($\ln \sigma$) |
|---|---|---|---|---|
| No. 1 | $Al_2O_3$ (6.0 nm)/Co (0.7 nm)/Pt (1.0 nm) | 55 at % Pt | 973 K-100 min (2.8 K/min) | 8.4 nm (0.15) |
| No. 2 | $Al_2O_3$ (6.0 nm)/Co (0.7 nm)/Pt (1.0 nm) | 55 at % Pt | 873 K-10 h (2.4 K/min) | 8.3 nm (0.20) |
| No. 3 | $Al_2O_3$ (6.0 nm)/Co (0.15 nm)/Pt (0.20 nm) | 61 at % Pt | 873 K-1 h (1.5 K/min) | 4.0 nm (0.13) |

at 973 K for 100 min (sample no. 1). Particle size is 8 nm in diameter. The particle is single crystalline, and clear (110) superlattice atomic planes of the $L1_0$ ordered structure can be seen as bright contrasts. The (220) atomic planes are also resolved as shown in the upper inset. Two types of bright

dots, strong and weak, correspond to Pt and Co atomic columns, respectively. Due to the alternate stacking of Co and Pt in the [001] direction of the $L1_0$ structure, the (220) atomic planes also possess an alternate stacking sequence of Co and Pt in the [110] direction. Thus, chemical sensitivity
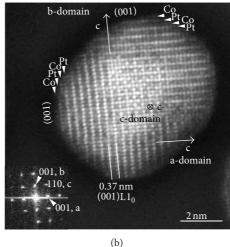
(a)                                                    (b)

FIGURE 3: HAADF-STEM images and corresponding FFT patterns of $L1_0$-CoPt nanoparticles: (a) single-crystal nanoparticle formed after annealing at 973 K for 100 min (sample no. 1). Magnified image is shown in the upper inset. (b) Nanoparticle composed of three-variant domains formed after annealing at 873 K for 10 h (sample no. 2).

of HAADF-STEM is quite useful to detect atomic ordering, while quantitative interpretation such as order parameter analysis is not straightforward. For this purpose, nanobeam electron diffraction can be employed under several prerequisite conditions [23].

On the other hand, for a specimen after annealing at 873 K for 10 h (sample no. 2), multivariant ordered domains were observed as well as single-variant particles. Figure 3(b) shows a $Z$-contrast image of a CoPt nanoparticle composed of three-variant ordered domains: the $c$-axis of the central region of the particle is normal to the film plane (parallel to the electron beam, c-domain), while those of other two variants in peripheral regions of the particle are in the film plane (a, b domains). Three kinds of superlattice reflections (001a, 001b, and 110c) in the FFT pattern also explain the formation of three-variant ordered domains. Note that the nanoparticle shown in Figure 3(b) contains two (001) facets, and, therefore, alternate stacking of Co(001) and Pt(001) atomic planes can be directly distinguished by $Z$-contrast in the image of a, b domains. They are both terminated by Co atomic planes as indicated by arrowheads, judging from the $Z$-contrast of Pt and Co. By contrast, Müller and Albe [24] have reported the termination of (001) planes by Pt atoms for FePt nanoparticles (TO, 2.5–8.5 nm in diameter, 50–54 at %Pt) based on Monte Carlo simulations. This discrepancy suggests that the particle shown in Figure 3(b) may not be in the thermodynamical equilibrium by annealing at 873 K for 10 h. Existence of three-variant ordered domains also indicates intermediate stage of atomic ordering [19, 25]. It is presumed that multiple nucleation of the ordered phase in a particle and a low interfacial energy between variant domains are responsible for the formation of such ordered domains. Surface segregation at {100} or {111} facets has been also discussed by Yang et al. (FePt, TO, 2.32–5.35 nm in diameter) [26] and Rossi et al. (CoPt, TO, 1.5–3 nm in diameter) [27];

however, it was difficult to detect this detailed surface atomic configuration in the present study except for the (001) planes shown in Figure 3(b).

Thus, the microscopy results indicate that postdeposition annealing at 973 K is required for realizing a highly ordered single-variant structure for the $L1_0$ CoPt nanoparticles prepared by epitaxial growth techniques using sequential deposition of Pt and Co [18]. Lowering of kinetic ordering temperature is also desired for practical applications; however, ordering rate of the Co-Pt system is slow compared to that of similar compounds such as Fe-Pt or Fe-Pd [28].

Figure 4(a) shows $Z$-contrast images for single-variant CoPt nanoparticles with size of 3–5 nm in diameter after annealing at 873 K for 1 h (sample no. 3). The beam incidence is the [001] direction (along the $c$-axis of the $L1_0$ structure). Clear (110) atomic planes of the $L1_0$ ordered structure can be seen in all the nanoparticles shown here. This is evidence of the atomic ordering in a small CoPt nanoparticle, while the degree of order is not known. It is noted that nanoparticles smaller than 3 nm showed weak superlattice reflections, indicating a low degree of order [18]. Figure 4(b) shows $Z$-contrast images of CoPt nanoparticles including structural domains. Particle sizes are comparable to those shown in Figure 4(a), while two- or three-variant domains are clearly seen in these nanoparticles. Coexistence of single-variant particles and multivariant particles in the same specimen film suggests that the interfacial energy between variant domains will be small enough to form such structural domains in a 4 nm sized particle. Furthermore, the $L1_0$ ordered domain was found in an extremely small CoPt nanoparticle, 2 nm in diameter [15]; this is also evidence of a low interfacial energy. According to our previous HRTEM observation on Fe-56 at %Pt nanoparticles, three-variant ordered domains are transformed to single domain after annealing for 24 h at 873 K [25].
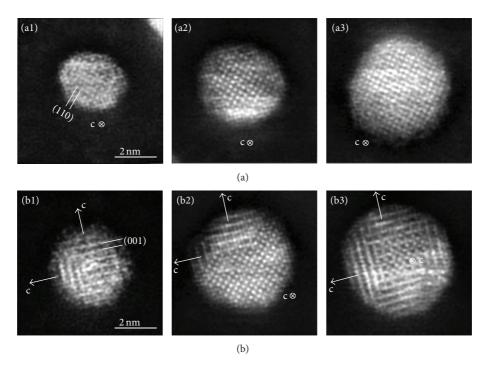
(a)



(b)

FIGURE 4: HAADF-STEM images of the $L1_0$-CoPt nanoparticles with sizes of 3–5 nm in diameter (sample no. 3). Annealing was performed at 873 K for 1 h. (a) Single-variant nanoparticles, (b) multivariant nanoparticles.

## 4. Conclusion

We have studied atomic structures of $L1_0$ CoPt nanoparticles using $Z$-contrast imaging by HAADF-STEM. Highly ordered particles are formed by high-temperature annealing at 973 K. Most of the particles are single crystal with $c$-axis oriented normal to the film plane. Image simulation revealed that HAADF-STEM image intensity is sensitive to thickness variation in addition to atomic number. On the other hand, for a specimen annealed at 873 K, nanoparticles composed of multivariant ordered domains are observed in addition to single-variant particles. It was found that (001) facets of particles with structural domains are terminated by Co atomic planes rather than by Pt, suggesting an intermediate stage of atomic ordering. Coexistence of single-variant particles and multivariant particles in the same specimen film suggests that the interfacial energy between the ordered domains will be small enough to form such structural domains in a particle as small as 4 nm in diameter. This study thus demonstrates that postdeposition annealing at 973 K is required for realizing highly ordered single-variant structure for the $L1_0$ CoPt nanoparticles prepared by epitaxial growth techniques using sequential deposition of Pt and Co.

## Conflict of Interests

The authors declare no possible conflict of interests.

## Acknowledgments

## References

[1] D. Weller and M. F. Doerner, "Extremely high-density longitudinal magnetic recording media," *Annual Review of Materials Science*, vol. 30, pp. 611–644, 2000.

[2] Y. Tanaka, "Fundamental features of perpendicular magnetic recording and design considerations for future portable HDD integration," *IEEE Transactions on Magnetics*, vol. 41, no. 10, pp. 2834–2838, 2005.

[3] M. A. Seigler, W. A. Challener, E. Gage et al., "Integrated heat assisted magnetic recording head: design and recording demonstration," *IEEE Transactions on Magnetics*, vol. 44, no. 1, pp. 119–124, 2008.

[4] R. Wood, M. Williams, A. Kavcic, and J. Miles, "The feasibility of magnetic recording at 10 terabits per square inch on conventional media," *IEEE Transactions on Magnetics*, vol. 45, no. 2, pp. 917–923, 2009.

[5] S. H. Liou, Y. Liu, S. S. Malhotra, M. Yu, and D. J. Sellmyer, "Magnetic properties of nanometer-size CoPt particles," *Journal of Applied Physics*, vol. 79, no. 8, pp. 5060–5062, 1996.

[6] C. Chen, O. Kitakami, S. Okanioto, Y. Shimada, K. Shibata, and M. Tanaka, "Large coercivity and granular structure of CoPt/SiO$_2$ films," *IEEE Transactions on Magnetics*, vol. 35, no. 5, pp. 3466–3468, 1999.

[7] A. Sakuma, "First principle calculation of the magnetocrystalline anisotropy energy of FePt and CoPt ordered alloys," *Journal of the Physical Society of Japan*, vol. 63, no. 8, pp. 3053–3058, 1994.

[8] H. Shima, K. Oikawa, A. Fujita et al., "Magnetocrystalline anisotropy energy in $L1_0$-type CoPt single crystals," *Journal of Magnetism and Magnetic Materials*, vol. 290-291, no. 1, pp. 566–569, 2005.

[9] T. Shima, T. Moriguchi, S. Mitani, and K. Takanashi, "Low-temperature fabrication of $L1_0$ ordered FePt alloy by alternate monatomic layer deposition," *Applied Physics Letters*, vol. 80, no. 2, pp. 288–290, 2002.

[10] S. Okamoto, N. Kikuchi, O. Kitakami, T. Miyazaki, Y. Shimada, and K. Fukamichi, "Chemical-order-dependent magnetic anisotropy and exchange stiffness constant of FePt (001) epitaxial films," *Physical Review B*, vol. 66, no. 2, Article ID 024413, pp. 1–9, 2002.

[11] K. Sato, T. J. Konno, and Y. Hirotsu, "Electron microscopy studies on magnetic $L1_0$-type FePd nanoparticles," *Advances in Imaging and Electron Physics*, vol. 170, pp. 165–225, 2012.

[12] K. Sato, J. G. Wen, and J. M. Zuo, "Intermetallic ordering and structure in Fe-Pd alloy nanoparticles," *Journal of Applied Physics*, vol. 105, no. 9, Article ID 093509, pp. 1–7, 2009.

[13] K. Sato, K. Yanajima, and T. J. Konno, "Structure and compositional evolution in epitaxial Co/Pt core-shell nanoparticles on annealing," *Thin Solid Films*, vol. 520, no. 9, pp. 3544–3552, 2012.

[14] M. Delalande, M. J.-F. Guinel, L. F. Allard et al., "$L1_0$ ordering of ultrasmall FePt nanoparticles revealed by TEM in situ annealing," *Journal of Physical Chemistry C*, vol. 116, no. 12, pp. 6866–6872, 2012.

[15] F. Tournus, K. Sato, T. Epicier, T. J. Konno, and V. Dupuis, "Multi-$L1_0$ domain CoPt and FePt nanoparticles revealed by electron microscopy," *Physical Review Letters*, vol. 110, no. 5, Article ID 055501, pp. 1–5, 2013.

[16] D. Wang, H. L. Xin, R. Hovden et al., "Structurally ordered intermetallic platinum-cobalt core-shell nanoparticles with enhanced activity and stability as oxygen reduction electrocatalysts," *Nature Materials*, vol. 12, no. 1, pp. 81–87, 2013.

[17] S. J. Pennycook and P. D. Nellist, Eds., *Scanning Transmission Electron Microscopy, Imaging and Analysis*, Springer, New York, NY, USA, 2011.

[18] K. Sato, K. Yanajima, and T. J. Konno, "Effect of cooling rate on size-dependent atomic ordering of CoPt nanoparticles," *Philosophical Magazine Letters*, vol. 92, no. 8, pp. 408–416, 2012.

[19] B. Bian, K. Sato, Y. Hirotsu, and A. Makino, "Ordering of island-like FePt crystallites with orientations," *Applied Physics Letters*, vol. 75, no. 23, pp. 3686–3688, 1999.

[20] D. Alloyeau, C. Ricolleau, C. Mottet et al., "Size and shape effects on the order-disorder phase transition in CoPt nanoparticles," *Nature Materials*, vol. 8, no. 12, pp. 940–946, 2009.

[21] http://elim.physik.uni-ulm.de/?page_id=834.

[22] T. B. Massalski, H. Okamoto, P. R. Subramanian, and L. Kacprzak, Eds., *Binary Alloy Phase Diagrams*, ASM International, Materials Park, Ohio, USA, 2nd edition, 1990.

[23] K. Sato, Y. Hirotsu, H. Mori, Z. Wang, and T. Hirayama, "Long-range order parameter of single $L1_0$-FePd nanoparticle determined by nanobeam electron diffraction: particle size dependence of the order parameter," *Journal of Applied Physics*, vol. 98, no. 2, Article ID 024308, pp. 1–8, 2005.

[24] M. Müller and K. Albe, "Lattice Monte Carlo simulations of FePt nanoparticles: influence of size, composition, and surface segregation on order-disorder phenomena," *Physical Review B*, vol. 72, no. 9, Article ID 094203, pp. 1–10, 2005.

[25] K. Sato, B. Bian, T. Hanada, and Y. Hirotsu, "Oriented $L1_0$-FePt nanoparticles and their magnetic properties," *Scripta Materialia*, vol. 44, no. 8-9, pp. 1389–1393, 2001.

[26] B. Yang, M. Asta, O. N. Mryasov, T. J. Klemmer, and R. W. Chantrell, "The nature of A1-$L1_0$ ordering transitions in alloy nanoparticles: a Monte Carlo study," *Acta Materialia*, vol. 54, no. 16, pp. 4201–4211, 2006.

[27] G. Rossi, R. Ferrando, and C. Mottet, "Structure and chemical ordering in CoPt nanoalloys," *Faraday Discussions*, vol. 138, pp. 193–210, 2008.

[28] Y. Hirotsu and K. Sato, "Growth and atomic ordering of hard magnetic $L1_0$-FePt, FePd and CoPt alloy nanoparticles studied by transmission electron microscopy: alloy system and particle size dependence," *Journal of Ceramic Processing Research*, vol. 6, no. 3, pp. 236–244, 2005.

*Research Article*

# The Study of Magnetorheology of Iron Oxide Nanowires

## S. P. Rwei,[1] L. Y. Wang,[2] and M. J. Chen[1]

[1] *Institute of Organic and Polymeric Materials, National Taipei University of Technology, No. 1, Section 3,*
  *Chung-Hsiao E. Road, Taipei 10648, Taiwan*
[2] *Center of Condensed Matter Science, National Taiwan University, Taipei, Taiwan*

Correspondence should be addressed to S. P. Rwei; f10714@ntut.edu.tw

In this work, circular $Fe_3O_4$ particles with a diameter of 24 nm and quasicircular $Fe_3O_4$ particles with a diameter of 10 nm were synthesized using peptization and coprecipitation methods, respectively. The coprecipitated particles were further formed into $Fe_3O_4$ nanowires at high temperature and high pressure in a strongly alkaline environment. The optimal environment for forming nanowire was 15 m (molality) NaOH at 120°C for three days; the resulting proportional relationship between its width and its height, the aspect ratio, was 50.5/1. In the second part of this study, the nanoparticles and nanowire were dispersed in silicon oil and formed into magnetorheological (MR) fluids of different concentrations, before undergoing various MR tests—a shear test, a compression test, and a creep recovery test. The results revealed that the MR performance of nanowire fluid was better than that of circular particle fluid, in terms of yield stress (35 Pa versus 60 Pa), compression displacement ($\Delta d$) (0.19 mm versus 0.44 mm), and creep recovery ratio (82% versus 48%). The experimental results conclude that the nanowire network is more robust than the nanoparticle network. The test of the storage shelf time revealed that 12 wt% nanowire fluid retained more than 80% of its original yield stress after three months, indicating slight precipitation in the nanowire fluid. In summary, the nanowire MR fluid had a stronger MR effect than traditional MR fluid that was prepared with spherical MR particles.

## 1. Introduction

A magnetorheological (MR) suspension can be promptly transformed from a fluid-like structure to a solid-like structure with a viscoelastic to plastic yielding by subjecting it into a magnetic field [1–7]. Rabinow [8] discovered this phenomenon in 1948. Since then, various metal or ceramic powders with magnetic characteristics have been dispersed in nonmagnetic carrier liquids (such as oil or aqueous liquids) in the preparation of MR suspensions. Smart damper [9] is an important application of magnetorheological (MR) fluid. The releasing of its internal energy depends mainly on the viscosity of the dashpot. Therefore, a method for preparing MR fluid with a wide range of viscosities, ensuring a strong response of the yield stress or creep recovery from low to high magnetic strength, is crucial. Notably, $Fe_3O_4$, having a net ferromagnetic moment arising from the incomplete cancellation of spin materials of $Fe^{2+}$ ions, can respond very sensitively to the magnetic fields. More importantly, the permanent magnetization of $Fe_3O_4$ nanoparticles is still weak enough that it cannot cause any interparticle agglomeration under zero magnetic field strength; $Fe_3O_4$ nanoparticle thus becomes a good candidate for the preparation of MR fluids. This work employs various chemical methods to synthesize $Fe_3O_4$ magnetic particles of various sizes and $Fe_3O_4$ magnetic nanowire and to form them into MR fluids, whose MR properties, including shear yield stress, compression resistance, creep recovery, and yield strength decay, are then observed. The goal is to find the formulation of MR fluids with optimal performance.

## 2. Experimental

*2.1. Peptization Synthesis of Nanoparticle I [10–12].* Add iron chloride hexahydrate (10.8 g, 80 mmol), sodium oleate (36.5 g, 240 mmol) to a mixed solution of ethanol (80 mL), deionized water (60 mL), and hexane (140 mL). Stir the mixture well in a 500 mL three-neck flask that is mounted on a condensation system. Heat to 70°C and maintain this

temperature for 4.5 h; then purify three times using deionized water (30 mL) and finally store the iron-oleate complex product in hexane. Add iron-oleate complex 9 g, oleic acid 1.7 g to 30 g tri-n-octylamine and stir well in a 500 mL three-neck flask. Heat at 3.3°C/min to 366°C or 300°C and maintain this temperature for 30 min. Wash the excessive oleic acid from the surface of $Fe_3O_4$ nanoparticles using ethanol or hexane, respectively.

### 2.2. Coprecipitation Synthesis of Nanoparticle II.

To 6 g iron chloride tetrahydrate and 12 g iron chloride hexahydrate add 25 mL deionized water and mix to form an ionic solution. Add 50 mL ammonium hydroxide rapidly while agitating mechanically; keep stirring for 6 min and coprecipitate [13–16] to obtain $Fe_3O_4$ nanoparticles. Use deionized water to wash off excessive ammonium hydroxide. Remove remaining deionized water in $Fe_3O_4$ nanoparticles by freeze-drying.

### 2.3. Hydrothermal Synthesis of Nanowire III.

Put 0.5 g $Fe_3O_4$ nanoparticles in a pressurized reaction flask and add sodium hydroxide solution to a concentration of 15 M. Place the flask in an oven and allow the hydrothermal reaction [17–19] to proceed at 120°C (2 atm) for three days to yield $Fe_3O_4$ nanowires. Use deionized water to remove the excess sodium hydroxide solution. Remove the remaining deionized water from the $Fe_3O_4$ nanowires by freeze-drying.

### 2.4. Preparation of Magnetic Fluid.

Add materials *I*, or *II*, or *III* to silicon oil with viscosities of 10 cp and 100 cp (polydimethylsiloxane PDMS). Stir well to obtain MR fluid. Pour the MR fluid into the groove on the lower plate of the rheometer (Anton Paar Physica MCR301 MRD). Then, lower the upper plate until the clearance is 0.1 cm. The temperature of the rheometer is held constant, 25°C. Apply various currents and measure the yield stress, the compression displacement, and the creep recovery rate of the specimen. The electronic micrographs were taken using transmission electron microscope at 300 kV (TEM Hitachi: H-7100). The X-ray powder diffractometer (XRD PANalytical X'Pert PRO MPD), operated at 45 kV and 20 mA under CuK$\alpha$ radiation, was applied to analyze the crystal phase. The detector was scanned over a range of $4\theta$ angles from 0° to 70° at a speed of 4° per minute.

## 3. Results and Discussion

Figure 1 presents a TEM image of $Fe_3O_4$ nanoparticles that were synthesized by oleic acid peptization. The diameters of the particles are uniformly distributed with an average of 24 nm. X-ray diffraction proves that the nanoparticles are pure $Fe_3O_4$ (Figure 2 lower curve). The peaks are consistent with the previous study [20]. Figure 3 presents a TEM image of $Fe_3O_4$ nanoparticles that were formed by coprecipitation. As is seen, the distribution of particle sizes is very broad— much broader than achieved by peptization. The particles are not spherical but appear quasicircular or even polygonal. However, X-ray diffraction pattern (Figure 2-upper curve) proves that they are still pure $Fe_3O_4$ particles.
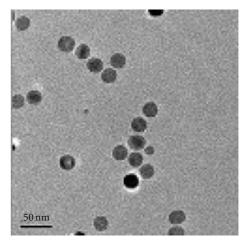


Figure 1: The TEM image of $Fe_3O_4$ nanoparticles synthesized by oleic acid peptization.



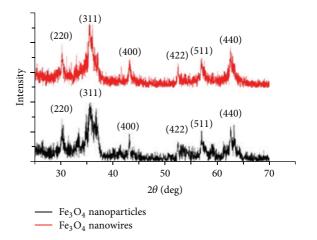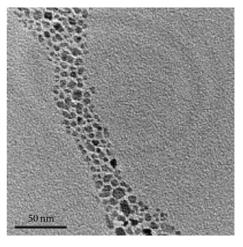Figure 2: The X-ray diffraction spectrum of $Fe_3O_4$ nanoparticle and nanowire.



Figure 3: The TEM image of $Fe_3O_4$ nanoparticles formed by coprecipitation.
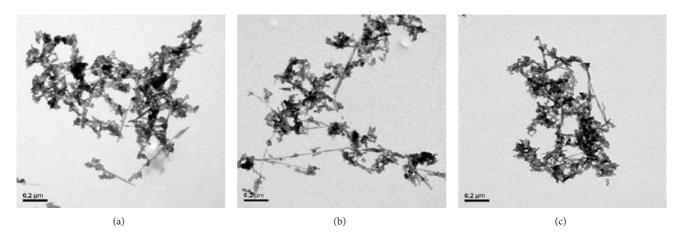
FIGURE 4: (a)~(c) The TEM image of $Fe_3O_4$ nanowires formed at high temperature, 110˚C, and under various NaOH concentrations, (a) 5 m, (b) 15 m, and (c) 20 m.
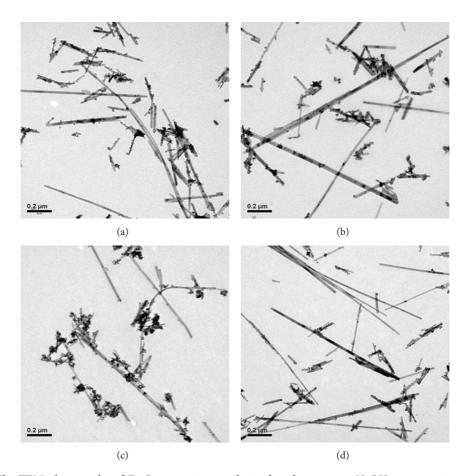


FIGURE 5: (a)~(d) The TEM photographs of $Fe_3O_4$ nanowires synthesized under constant NaOH concentration, 15 m, and at various temperatures or reaction durations, (a) 120˚C, 3 days, (b) 130˚C, 3 days, (c) 140˚C, 3 days, and (d) 120˚C, 9 days.

Figures 4(a)–4(c) present the influence of NaOH concentration on the lengths of $Fe_3O_4$ nanowires formed at high temperature (110˚C) and high pressure in a hydrothermal environment. As is seen, the nanowires were longest when the NaOH concentration was 15 m. As the NaOH concentration was further increased, less deionized water can be vaporized, resulting in the pressure in the flask at high temperature being reduced. Consequently, the $Fe_3O_4$ nanoparticles are not driven to combine to form nanowire. The length of the rod shapes is therefore reduced. In short, the optimal environment in which to form nanowire is 15 m NaOH, which was utilized hereafter.
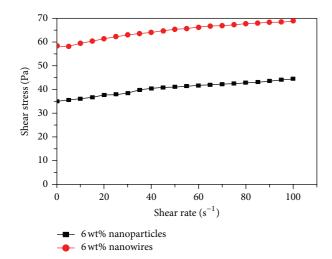
FIGURE 6: The plot of shear stress against shear rate for MR fluids containing 6 wt% $Fe_3O_4$ nanoparticles and nanowires.



FIGURE 8: The yield stress is a function of solid loading of $Fe_3O_4$ MR fluids.
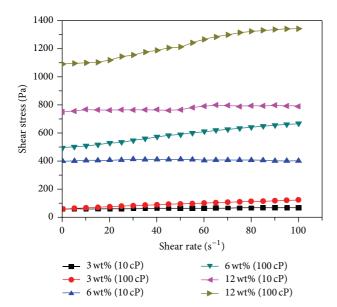


FIGURE 7: The plot of shear stress against shear rate for MR fluids containing nanowires at various solid loadings and dispersed at different viscosities of PDMS.

Figures 5(a)–5(d) present a TEM photograph of $Fe_3O_4$ nanowires that were synthesized at various temperatures or reaction durations. The conditions of Figure 5(a), including a temperature of 120°C, in which the fewest particles were unreacted, were obviously optimal. Analysis of the image reveals that the aspect ratio of 50.5 : 1 obtained at 120°C is also the maximum value. The optimal conditions for forming $Fe_3O_4$ nanowire formation are thus determined to be 15 m NaOH, 120°C, high pressure, and a strongly alkaline ambient.

As shown in Figure 6, the yield stress of $Fe_3O_4$ nanowire fluid, 60 Pa, is nearly double that of $Fe_3O_4$ nanoparticle fluid, 35 Pa, at the same concentration (6 wt%). This result indicates that the asymmetry of nanowire can enhance the MR effect. Figure 7 plots the dependence of shear stress on
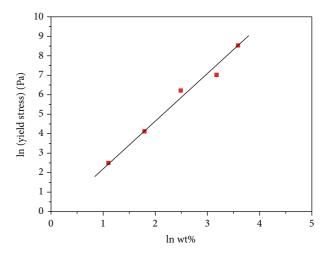
shear rate for various concentrations of $Fe_3O_4$ nanowires that were suspended in silicon oil with various viscosities (10 cp, 100 cp). The MR fluid exhibits typical Bingham character [21], with a yield stress threshold at which fluidity in a magnetic field is first exhibited. Figure 7 demonstrates that the yield stress increases with the nanowire concentration. Moreover, when the solid loading is 12 wt%, the yield stress of the 100 cp suspension is 1.5 times that of the 10 cp suspension (1100 Pa versus 720 Pa). This result demonstrates that an increase of PDMS viscosity results in a higher yield stress at a given $Fe_3O_4$ loading. Figure 8 plots the yield stress against $Fe_3O_4$ solid concentrations when 0–36 wt% of $Fe_3O_4$ nanowires are suspended in 100 cp silicon oil. In the plot, as the solid loading increases, the yield stress increases as approximately a second-order polynomial (slope = 2.35) function. Even though the increase of $Fe_3O_4$ loading positively affects the MR effect, the nanowire agglomeration that arises from high loading may occur seriously. This work demonstrates that the solid loading of $Fe_3O_4$ nanowires can be increased to 36 wt% without causing serious agglomeration. The authors' ultimate goal is to formulate a highly effective MR fluid at a sufficiently high concentration so that it can flow freely in a nonmagnetic field without solid-liquid separation but has a yield stress that can increase to $10^4$ Pa in a magnetic field.

Along with the shear test, the compression test can also be employed to characterize MR fluids. When a magnetic fluid is placed in a magnetic field, MR particles are temporarily in a network state, as shown in Figure 9(a). The purpose of shear test, as stated previously, is to determine the critical shear stress, also known as the yield stress that disrupts the network state. Similarly, the action of compression stress on the network can alter the network structure. Figure 9(b) demonstrates that under a given compression stress, a smaller change in volume, or a smaller $\Delta d$, corresponds to a greater magnetic attractive force among the magnetic particles within the network. When subjected to an external force, a more robust network is associated with a greater displacement resistance, and the displacement in
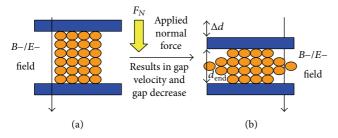
FIGURE 9: (a), (b) The illustration of structure change for an MR fluid under the compression test.
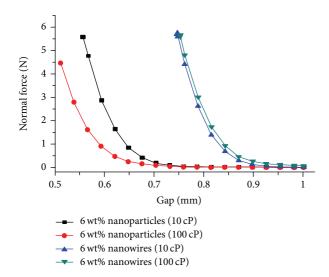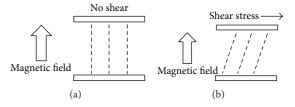


FIGURE 11: The illustration of $Fe_3O_4$ nanowires lining up along the magnetic line of force for the MR fluid (a) without shear and (b) under shear.
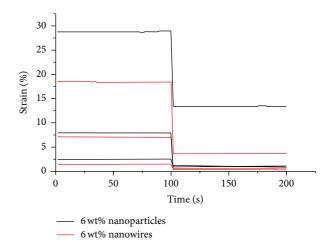


FIGURE 10: The plot of normal force versus gap distance for various MR fluids subjecting to the compression test.



FIGURE 12: The plot of creep and recovery test for MR fluids containing 6 wt% of $Fe_3O_4$ nanoparticles and nanowires under various shear stresses (10, 20, and 30 Pa).

the direction of the force is smaller. **Figure 10** reveals that the compression displacements of the $Fe_3O_4$ nanoparticle are 0.39 mm and 0.44 mm in 10 cp and 100 cp silicon oil, respectively. In contrast, the compression displacements ($\Delta d$) of the nanowires dispersed in 10 cp and 100 cp silicon oil are 0.19 mm and 0.07 mm, respectively. The experimental result demonstrates that nanowire can exhibit favorable MR behavior. Additionally, the nanowire network has a higher compact density and toughness than the nanoparticle network. In fact, the particles are orientated and line up along the magnetic line of force with fewer joints. However, the line derived from the circular nanoparticles has more junctions than that derived from a nanowire. These junctions are the weakest points of the line. They usually collapse under a shear force or compression stress (Figures 11(a) and 11(b)). The resistance of the nanowire network to an external force is better because it has fewer junctions. The results also reveal that 10 cp silicon oil is associated with a shorter compression displacement than 100 cp silicon oil, perhaps because the former lubricates the joints less well than the latter. Better lubrication is generally associated with longer compression displacement.

The creep and recovery test [22, 23] focuses on investigating the recovery behavior of a magnetic network following deformation by shearing, which has rarely been studied as part of MR investigations. In this work, the elasticity of the magnetic network structure is determined by applying a constant shear stress less than the yield stress to the MR fluid. The transient displacement of the MR structure reaches a constant, and then the stress is removed to observe the recovery of the MR fluid. A high recovery ratio demonstrates excellent elasticity of the magnetic network. It also indicates that the arrangement of magnetic particles inside the network is in a very stable state. Notably, the stress applied herein is less than the yield stress, and none of the magnetic fluids flows; rather, it exhibits various degrees of displacement. If obvious damage or permanent displacement occurs in the creep test, then the stress has permanently and detrimentally affected the relative positions of the network particles, such that the magnetic network structure fails to recover after shearing. This situation reveals that the solid character of the magnetic network is not strong. **Figure 12** plots the result of the creep and recovery test for nanoparticles and nanowire. When the shear stress (10 Pa or 20 Pa) is much less than the yield stresses of the MR fluids (35 Pa for nanoparticles and 60 Pa for nanowire), the recovery ratio of elasticity is nearly 100%. However, at a shear stress of 30 Pa, which is close to the yield stress of nanoparticles, the recovery ratio is only 48%. In contrast, 30 Pa is far below the yield stress of the nanowire, for which the recovery ratio is 82%. This result confirms

that a nanowire network is more robust than a nanoparticle network. Additionally, Figure 12 shows that a network formed by the magnetic field suffers serious damage when the applied stress is only slightly less than the yield stress. Figure 13 plots the creep and recovery of MR fluids when the applied stress exceeds the yield stress. In the creep stage in Figure 13, the creep strain is not constant but increases with time. When the creep recovery stage is triggered 100 seconds later, the recovery is unobservable because the previous magnetic network structure had completely disintegrated. Even if the applied stress were terminated, a new network that is oriented with the magnetic field would gradually form, but it would have no relation to the previously damaged network in terms of structure or relative position of particles. Accordingly, recovery cannot occur when the applied stress exceeds the yield stress.

To determine whether the nanowire fluid meets the operating requirements, 12 wt% nanowire suspensions were stored for one, two, and three months, restirred, and then individually subjected to the MR shear test. Figure 14 shows that the yield stress decays from an initial value of 400 Pa at a rate from 20 Pa–30 Pa per month to 325 Pa after three months. This result shows that, because the size of the suspended nanowires is of the order of microns, their Brownian motion cannot overcome gravity, and precipitation eventually occurs. However, after restirring, this suspended matter is again dispersed, reducing the agglomeration. Figures 15(a) to 15(c) are TEM images of nanowire fluid with various storage periods. A comparison with Figure 5(b) reveals slight wire agglomeration, which, while not severe, should be reduced.

## 4. Conclusions

This systematic study of the preparation of magnetic particles preparation and their MR characterization supports the following conclusions.

(1) Circular $Fe_3O_4$ particles with a diameter of 24 nm and quasicircular $Fe_3O_4$ particles with a diameter of 10 nm were synthesized by peptization and coprecipitation. The peptized particles were formed into $Fe_3O_4$ nanowire at high temperature and high pressure in strongly alkaline environment. The optimal reaction conditions for forming nanowires are 15 m NaOH at 120°C for three days. An aspect ratio as high as 50.5 : 1 can thus be achieved.

(2) The MR shear test revealed that the yield stress of $Fe_3O_4$ nanowire fluid is double that of the same concentration of $Fe_3O_4$ nanoparticle fluid. Furthermore, as the $Fe_3O_4$ particle concentration increases, the yield stress increases following a second-order polynomial (slope = 2.35) curve.

(3) The compression displacement ($\Delta d$) of the $Fe_3O_4$ nanowire MR fluid is far less than that of the $Fe_3O_4$ nanoparticle MR fluid (0.19 mm versus 0.44 mm). The creep recovery capacity of $Fe_3O_4$ nanowire also exceeds that of $Fe_3O_4$ nanoparticle.
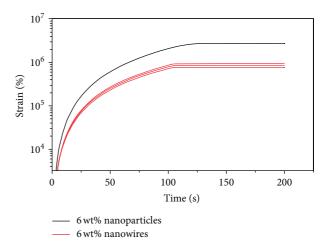


FIGURE 13: The plot of creep and recovery test for MR fluids containing 6 wt% of $Fe_3O_4$ nanoparticles and nanowires under shear stress of 70 Pa, which is far above the yield stresses of both MR fluids. The experiment was repeated 3 times and a good reproducibility is shown.
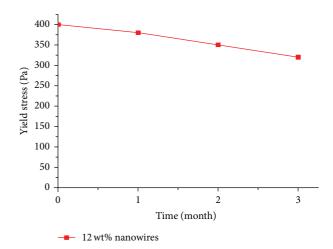


FIGURE 14: The plot of yield stress versus the shelf time for an MR fluid containing 12 wt% of $Fe_3O_4$ nanowires.

(4) The creep and recovery test showed that a network formed by the magnetic field had serious damage once the applied stress was close to the yield stress.

(5) In the storage test, 12 wt% nanowire fluid retained more than 80% of its original yield stress after three months.

In summary, nanowire magnetic particles can exhibit a better MR effect than traditional magnetic particles that were prepared with spherical MR particles.

## Conflict of Interests

The MR fluid prepared according to the method mentioned herein is a novel method. Even though it still has long way to go for commercial application, its patents have been claimed
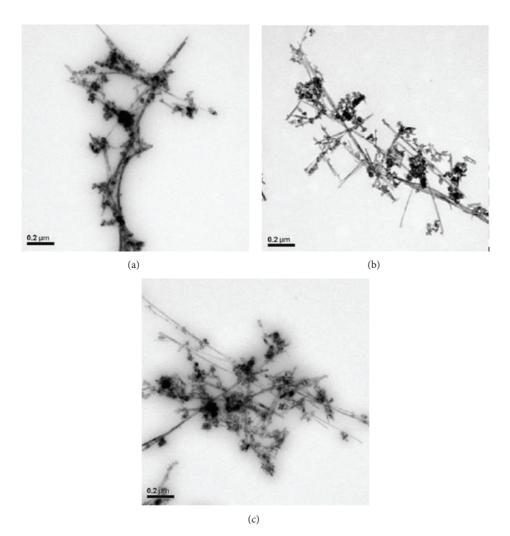
(a)



(b)



(c)

FIGURE 15: (a)~(c) The TEM images of a MR fluid containing 12 wt% $Fe_3O_4$ nanowires, which were stored at various periods of time: (a) 1 month, (b) 2 months, and (c) 3 months.

and filed by the authors and the financial founder: NSC of Taiwan. There is no conflict of interests for any commercial application at present time or in the future.

## Acknowledgment

## References

[1] W. M. Winslow, "Induced fibration of suspensions," *Journal of Applied Physics*, vol. 20, no. 12, pp. 1137–1140, 1949.

[2] P. P. Phulé, "Magnetorheological (MR) fluids: principles and applications," *Smart Materials Bulletin*, vol. 2001, no. 2, pp. 7–10, 2001.

[3] G. Bossis, O. Volkova, S. Lacis, and A. Meunier, "Magnetorheology: fluids, structures and rheology," *Stefan Odenbach*, vol. 594, pp. 202–230, 2002.

[4] I. Bica and H. J. Choi, "Preparation and electro-thermoconductive characteristics of magnetorheological suspensions," *International Journal of Modern Physics B*, vol. 22, no. 29, pp. 5041–5064, 2008.

[5] J. L. Viota, J. de Vicente, J. D. G. Durán, and A. V. Delgado, "Stabilization of magnetorheological suspensions by polyacrylic acid polymers," *Journal of Colloid and Interface Science*, vol. 284, no. 2, pp. 527–541, 2005.

[6] A. J. F. Bombard, M. Knobel, and M. R. Alcântara, "Phosphate coating on the surface of carbonyl iron powder and its effect in magnetorheological suspensions," *International Journal of Modern Physics B*, vol. 21, no. 28-29, pp. 4858–4867, 2007.

[7] F. F. Fang and H. J. Choi, "Fabrication of multiwalled carbon nanotube-wrapped magnetic carbonyl iron microspheres and their magnetorheology," *Colloid and Polymer Science*, vol. 288, no. 1, pp. 79–84, 2010.

[8] J. Rabinow, "The magnetic fluid clutch," *Transactions of the American Institute of Electrical Engineers*, vol. 67, pp. 1308–1315, 1948.

[9] A. G. Olabi and A. Grunwald, "Design and application of magneto-rheological fluid," *Materials and Design*, vol. 28, no. 10, pp. 2658–2664, 2007.

[10] X. Ren, "Large electric-field-induced strain in ferroelectric crystals by point-defect-mediated reversible domain switching," *Nature Materials*, vol. 3, no. 2, pp. 91–94, 2004.

[11] S. Sun, H. Zeng, D. B. Robinson et al., "Monodisperse $MFe_2O_4$ (M = Fe, Co, Mn) nanoparticles," *Journal of the American Chemical Society*, vol. 126, no. 1, pp. 273–279, 2004.

[12] T. Hyeon, "Chemical synthesis of magnetic nanoparticles," *Chemical Communications*, no. 8, pp. 927–934, 2003.

[13] R. Massart, "Preparation of aqueous magnetic liquids in alkaline and acidic media," *IEEE Transactions on Magnetics*, vol. 17, no. 2, pp. 1247–1248, 1981.

[14] J. Zhang, Q. Kong, J. Du, D. Ma, G. Xi, and Y. Qian, "Formation, characterization, and magnetic properties of $Fe_3O_4$ microoctahedrons," *Journal of Crystal Growth*, vol. 308, no. 1, pp. 159–165, 2007.

[15] J. Wang, K. Zhang, Z. Peng, and Q. Chen, "Magnetic properties improvement in $Fe_3O_4$ nanoparticles grown under magnetic fields," *Journal of Crystal Growth*, vol. 266, no. 4, pp. 500–504, 2004.

[16] S. Lian, E. Wang, L. Gao et al., "Growth of single-crystal magnetite nanowires from $Fe_3O_4$ nanoparticles in a surfactant-free hydrothermal process," *Solid State Communications*, vol. 132, no. 6, pp. 375–378, 2004.

[17] S. Lian, E. Wang, Z. Kang et al., "Synthesis of magnetite nanorods and porous hematite nanorods," *Solid State Communications*, vol. 129, no. 8, pp. 485–490, 2004.

[18] K. He, C.-Y. Xu, L. Zhen, and W.-Z. Shao, "Hydrothermal synthesis and characterization of single-crystalline $Fe_3O_4$ nanowires with high aspect ratio and uniformity," *Materials Letters*, vol. 61, no. 14-15, pp. 3159–3162, 2007.

[19] X. Lan, X. Cao, W. Qian, W. Gao, C. Zhao, and Y. Guo, "Long $Fe_3O_4$ nanowires decorated by CdTe quantum dots: synthesis and magnetic-optical properties," *Journal of Solid State Chemistry*, vol. 180, no. 8, pp. 2340–2345, 2007.

[20] G. Vaidyanathan, S. Sendhilnathan, and R. Arulmurugan, "Structural and magnetic properties of $Co_{1-x}Zn_xFe_2O_4$ nanoparticles by co-precipitation method," *Journal of Magnetism and Magnetic Materials*, vol. 313, no. 2, pp. 293–299, 2007.

[21] J. M. G. Cowie and V. Arrighi, *Polymers: Chemistry and Physics of Modern Materials*, CRC Press, New York, NY, USA, 2007.

[22] I. G. Plashchina, N. V. Grinberg, E. E. Braudo, and V. B. Tolstoguzov, "Conformational transition and aggregation of $x$-carrageenan macromolecules in solution," *Colloid and Polymer Science*, vol. 258, no. 9, pp. 1038–1043, 1980.

[23] S.-P. Rwei and L. Wang, "Synthesis and electrical, rheological and thermal characterization of conductive polyurethane," *Colloid and Polymer Science*, vol. 285, no. 12, pp. 1313–1319, 2007.

*Research Article*

# Synthesis and Magnetorheology Study of Iron Oxide and Iron Cobalt Oxide Suspensions

## Syang-Peng Rwei,[1] Lee Yi Wang,[2] and Po-Wen Yang[1]

[1] *Institute of Organic and Polymeric Materials, National Taipei University of Technology, No. 1, Section 3,*
*Chung-Hsiao E. Road, Taipei 10648, Taiwan*
[2] *Center Condensed Matter Science, National Taiwan University, Taipei, Taiwan*

Correspondence should be addressed to Syang-Peng Rwei; f10714@ntut.edu.tw

This study investigates the magnetorheology (MR) of polydimethylsiloxane (PDMS) that contains magnetic powders of various compositions, shapes, and concentrations. Two magnetic powders, $Fe_3O_4$ and $CoFe_2O_4$, were synthesized. TEM images reveal that a powder of spherical particles was obtained at high temperature. A powder with nonspherical star shape was synthesized at low temperature. A rheological test confirmed a typical Bingham behavior for all the MR fluids prepared in this study. Experimental results demonstrated that the cobalt ferrite exhibited a more superior yield stress than the ferrite compound. A magnetic powder of larger particles was found to have higher yield stress. Moreover, the spherical particles yielded a higher yield stress than the star-shaped particles. The "saturated magnetic strength" increased with the loading of the magnetic powder. Finally, the results demonstrate that 12 wt% $CoFe_2O_4$ nanopowder (10 nm) dispersed in the PDMS liquid exhibited a large range of yield stresses (0 to 644 Pa).

## 1. Introduction

A magnetorheological (MR) fluid can be rapidly transformed from a Newtonian fluid-like structure to a solid-like structure with viscoelastic-plastic yielding by applying a magnetic field [1–7]. Rabinow [8] discovered this phenomenon in 1948. Since then, various metal or ceramic powders with magnetic characteristics have been dispersed in nonmagnetic carrier liquids [9], such as oil or aqueous liquids, in the preparation of MR fluids. The smart damper design [10] is currently the most advanced application of MR suspensions. It releases energy using a magnetorheological dashpot and uses electric power to align magnetic nanoparticles that are suspended in liquid with a magnetic warp. The particles are orientated almost perpendicular to the direction of fluid motion (Figure 1). Accordingly, the flow is blocked and the viscosity is thus increased. Regardless of the magnitude of a shock, the energy dissipation always remains optimal in the smart damper because the viscosity of the suspension can be adjusted.

Among all the methods to produce the magnetic nanoparticles [11–13], the thermal decomposition method was the most common one in a lab scale and was therefore selected in this work. This study investigates the magnetic fluids, with a view to form magnetic nanoparticles of different shapes and sizes under the control of chemosynthesis [14–18] and then to mix them with PDMS to make magnetic fluid with various solid loadings. MR tests are then performed. The most common MR fluid consists of particles on a micron-scale, normally 5–200 $\mu$m in size. The micron-scale particles are too weak to be stabilized by the Brownian motion, and, using which, the reproducibility of MR characterization is difficult to achieve. Accordingly, the sedimentation of particles remains a critical problem to solve in relation to most designed MR fluids—even those that involve added surfactants. Nanoparticles, however, can be easily stabilized in a liquid with the aid of Brownian motion and the repulsive effect from the surfactant. A special synthetic approach was followed in this study to produce nanoscale particles in a manner that eliminates the sedimentation problem.
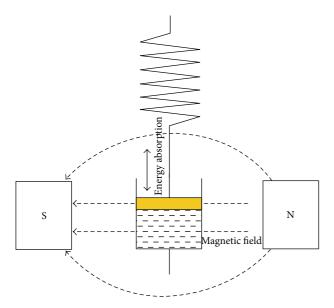
FIGURE 1: Schematic diagram of magnetorheological damper [19].

## 2. Experimental

### 2.1. Preparation of Iron Oxide ($Fe_3O_4$) Nanoparticles.
$FeCl_3 \cdot H_2O$ (10.8 g, 40 mmol), sodium oleate (36.5 g, 120 mmol), distilled water (60 mL), ethanol (80 mL), and hexane (140 mL) were put in a 500 mL three-neck flask and stirred under nitrogen for one hour to dissolve them completely. Then, the flask was mounted onto a condensing system and heated to 70°C at a heating rate of 3.3°C/min in the nitrogen environment. This temperature was maintained for 4.5 hours and three extractions were performed after the reaction using distilled water (60 mL). The iron-oleate complex (1) with a black-brown appearance was obtained. A rotary concentrator was then used to remove the solvent.

Product (1) (9.00 g, 10 mmol), oleic acid (1.73 g, 6 mmol) and tri-n-octylamine (30.00 g) were put in a 500 mL three-neck flask. A magnet was added and stirred in a nitrogen environment for 40 minutes to mix the contents uniformly. The condensing system, in the nitrogen environment, was set up to 300 or 366°C at a heating rate of 3.3°C/min. A black solution was obtained after reaction for 30 minutes. The ethanol was used to separate out the black solid, namely, the $Fe_3O_4$ product. Finally, the $Fe_3O_4$ was purified using hexane to remove the organic substance on its surface (Figure 2).

### 2.2. Preparation of Iron Cobalt Oxide ($CoFe_2O_4$) Nanoparticles.
The cobalt ferrite nanoparticles have been prepared using the method developed by Hyeon as follows [20]. Iron (III) acetylacetonate (0.71 g, 2 mmol), cobalt (II) acetylacetonate (0.26 g, 1 mmol), and 1,2-tetradecanediol (2.56 g, 10 mmol) were put in a 500 mL three-neck flask. Nitrogen deoxidized phenyl ether (20 mL), oleic acid (1.73 g, 6 mmol), and oleyamine (2.00 g, 6 mmol) were then added and stirred in a nitrogen environment for one hour to ensure uniform mixing. The condensing system, in the nitrogen environment, was set up to 200°C at a rate of 3.3°C/min and maintained

for 30 minutes; the system was then heated to 265°C at a heating rate of 3.3°C/min and maintained for 30 minutes. Alternatively, the condenser was heated to 300°C and maintained for one hour after reaction at 200°C for two hours. A black solution was yielded after the reaction is complete and ethanol was used to separate out the black solid. The black solid thus obtained is the product $CoFe_2O_4$. The $CoFe_2O_4$ was purified using hexane to remove the organic substance on its surface (Figure 3). All of the chemicals used were supplied by ACROS Chemicals and used without further purification.

### 2.3. Preparation of Magnetic Fluid.
The magnetic material 0.2 g was blended with 1.5 mL polydimethylsiloxane (PDMS, viscosity 100 cp) and stirred uniformly. The content was poured into the lower plate of rheometer (Anton Paar Physica MCR301 MRD). Then, the upper plate was lowered to maintain the spacing between the plates at 0.1 cm. The temperature of the rheometer was kept at 25°C. The yield stress of the object was measured under various magnetic strength. The samples were prepared in the following orders: (1) $Fe_3O_4$ (300°C), (2) $Fe_3O_4$ (366°C), (3) $CoFe_2O_4$ (265°C), and (4) $CoFe_2O_4$ (300°C).

### 2.4. Principle of Magnetorheology.
Figures 4(a) to 4(d) present the basic principle of magnetorheology. When a magnetic fluid is placed in a magnetic field, magnetic nanoparticles are temporarily in a network state, as shown in Figures 4(b) to 4(c). The purpose of shear test is to determine the critical shear stress, also known as the yield stress, which disrupts the network state (Figure 4(d)). A larger yield stress indicates that the tested MR fluid exhibits a stronger MR effect.

The pure PDMS fluid that was used herein is a Newtonian fluid. An MR fluid, in contrast, exhibits Bingham character in a magnetic field. Such a Bingham fluid [19] has a so-called yield stress ($\tau_0$). The MR fluid must overcome this threshold for the onset of fluidity in a magnetic field. Equation (1) defines "apparent viscosity" ($\mu_a$), taking into account the yield stress in viscosity calculation.

$$\tau = \tau_0 + \mu_0 \dot{\gamma},$$
$$\mu_a = \frac{\tau}{\dot{\gamma}} = \frac{\tau_0}{\dot{\gamma}} + \mu_0. \tag{1}$$

In (1), $\tau$ denotes the shear stress; $\tau_0$ denotes the yield stress; $\mu_0$ denotes the quasi-Newtonian viscosity; $\dot{\gamma}$ represents the shear rate, which is the gradient of the velocity against the vertical displacement, and $\mu_a$ represents the apparent viscosity, which is the ratio of the measured shear stress to the given shear rate.

For a fixed shear rate, a larger yield stress corresponds to a higher apparent viscosity. The magnetic field is adjusted by varying the electric current, and the targeted apparent viscosity is thereby obtained.

## 3. Results and Discussion

Figure 5(a) presents the wide-angle X-ray diffraction pattern of $Fe_3O_4$ particles that were synthesized in this work. All of

Iron chloride + sodium oleate $\longrightarrow$ iron-oleate complex

Iron-oleate complex + oleic acid $\xrightarrow[366°C \text{ or } 300°C]{Tri-n-octylamine}$ $Fe_3O_4$

Iron-oleate complex + [structure] $\xrightarrow[Tri-n-octylamine]{High\ temperature}$ $Fe_3O_4$

FIGURE 2: Scheme of $Fe_3O_4$ nanoparticle Synthesis.

$Co(acac)_2 + Fe(acac)_3 + 1,2\text{-}RCH(OH)CH_2OH + RCOOH + RNH_2$ $\xrightarrow[\substack{(1)\ N_2 \\ (2)\ High\ temperature \\ High\ BP.\ solvent}]{}$ $CoFe_2O_4$

FIGURE 3: Preparation of iron cobalt oxide ($CoFe_2O_4$) nanoparticles.
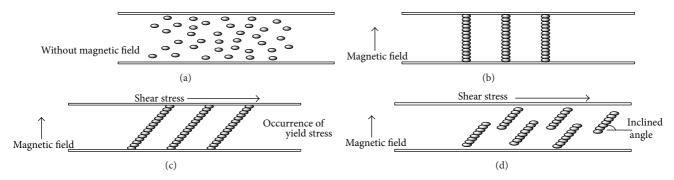


FIGURE 4: Schematic diagram of yield stress.

the characteristic peaks of the crystal (30.1 (200), 35.4 (311), 37.0 (222), 43.1 (400), 53.4 (422), 56.9 (511), 62.5 (440)) are similar to other scholars' results [21, 22], proving that the synthesized particles are granular $Fe_3O_4$ crystals. The wide-angle X-ray diffraction pattern of $CoFe_2O_4$ particles that were synthesized in this work was shown in Figure 5(b). All of the characteristic peaks (18.1 (111), 30.1 (220), 35.7 (311), 37.0 (222), 43.1 (400), 53.4 (422), 57.0 (511), 62.5 (440)) of the crystal are similar to other scholars' results [23–25], indicating that the synthesized particles are granular $CoFe_2O_4$ crystals.

Figures 6(a) and 6(b) are TEM photos of $Fe_3O_4$ particles that were synthesized at 366°C and 300°C, respectively. They reveal that the particles formed at 300°C are star shaped; the longest diagonal distance between two apexes is 80 nm, and the internal diameter of the particles is around 40 nm. In contrast, regular, spherical particles (30 nm in diameter) are obtained at 366°C, suggesting that a high temperature yields round and uniform particles, and a low temperature yields nonspherical particles, even with multi-acute angles.

Crystallization is usually divided into "nucleation" and "growth" stages. Low temperature favors nucleation but is dis-advantageous to growth, whereas high temperature disfavors nucleation but favors growth. The reactant diffusion rate is low at low temperature. The crystal nucleus is unlikely to grow uniformly to form a 3-D symmetrical sphere; in contrast, particles with polygonal shape are synthesized. The convex
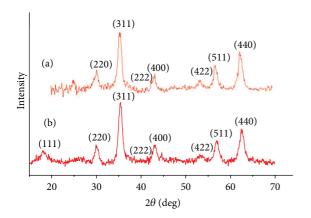
FIGURE 5: X-ray diffraction pattern of (a) $Fe_3O_4$ and (b) $CoFe_2O_4$.

TABLE 1: Various shapes and sizes of nanoparticles synthesized at different temperatures.

| Particle type | Synthesis temperature (°C) | Shape | Diameter (nm) |
|---|---|---|---|
| $Fe_3O_4$ | 300 | Star | $40 \pm 6^*$ |
| $Fe_3O_4$ | 366 | Sphere | $30 \pm 2$ |
| $CoFe_2O_4$ | 265 | Sphere | $3 \pm 1$ |
| $CoFe_2O_4$ | 300 | Sphere | $10 \pm 3$ |

*The mean value of the core-diameter of the star particles.

TABLE 2: The $\tau_{0a}$ and $\mu_0$ of $CoFe_2O_4$ 12 wt% MR fluid under different magnetic strengths.

| Magnetic field strength (Gauss) | $\tau_{0a}$ (Pa) | $\mu_0$ (Pa S) |
|---|---|---|
| 0 | 0 | 0.5 |
| 1400 | 296.8 | 0.9 |
| 2800 | 404.3 | 1.2 |
| 5800 | 511.5 | 1.4 |
| 8600 | 576.7 | 1.5 |
| 10000 | 644.3 | 1.6 |

surfaces of a polygonal particle can more easily capture a new $Fe_3O_4$ ionic particle than can do the spherical surfaces, so the crystal keeps growing along the convexity and forms several arms. Therefore, star-shaped particles with multiacute angles are formed. However, the diffusion rate is high at high temperature, and the crystal nuclei are uniform, so numerous new $Fe_3O_4$ ionic particles are stratified on the surface of each nucleus simultaneously. The crystallization time is too short to allow any nucleus to form a convexity, so round crystals uniformly grow instead. The formation of the star-shaped or polygonal nanoparticles was also observed by other scholars [26, 27], and similar growth mechanism was proposed.

Figures 6(c) and 6(d) are the TEM images of $CoFe_2O_4$ particles that were synthesized at 265°C and 300°C, respectively. Particles that were synthesized at high temperature were spherical with a relatively uniform diameter of approximately 10 nm. Particles synthesized at low temperature, however, are nonspherical and have sizes of 3~5 nm. The difference between the shapes of $CoFe_2O_4$ particles can be explained similarly to the mechanism of formation of the $Fe_3O_4$ particles mentioned previously; a high temperature promotes the formation of round particles because the rate of the diffusion of the ionic particles is high enough to make the suspension contain a homogenous ionic-particle distribution at high temperature. At higher temperatures, nucleation and growth may not be easily separated. The homogeneity of the crystallization process is better and can thus yield a more spherical particle with a larger diameter. The relationship between synthesis temperature and the shape of $CoFe_2O_4$ and $Fe_3O_4$ particles is shown in Table 1. Notably, the dependence of temperature on particle size and shape is only valid for the "thermal decomposition method" used herein. Similar result was also reported by other scholars [28].

Figure 7 presents the MR result of $CoFe_2O_4$ (synthesized at 300°C) dispersed in PDMS (12 wt%). The MR fluid clearly changed from a Newtonian fluid to a Bingham fluid when a magnetic field was applied. As the magnetic field increases, the yield stress ($\tau_0$) increases, and the quasi-Newtonian viscosity ($\mu_0$) of the fluid increases. Table 2 summarizes the results from Figure 7. Table 2 demonstrates that the yield stress, defined as the extrapolated stress at zero shear rate,

increases with the magnetic field. Accordingly, when the magnetic field increases, the magnitude of the yield stress, which is the range of deformation before fracture, increases, as demonstrated in Figure 4(c). If the line of magnetic nanoparticles is broken, then various dispersed particle groups advance in the original direction of the shear force and thus flow forward. However, the magnetic field causes the particle groups to follow an inclination that deviates from the direction of flow in the flow process. A larger deviation corresponds to greater resistance of the fluid and, therefore, a greater viscous stress. Therefore, quasi-Newtonian viscosity ($\mu_0$) increases with magnetic force. In fact, the Bingham yield stress ($\tau_0$) and quasi-Newtonian viscosity ($\mu_0$) do not increase without limit. When the magnetic field continues to increase, the magnetic fluids eventually reach their own "saturated magnetic strength."

Figure 8 plots the relationship between yield stress ($\tau_0$) and magnetic flux density (G) for $Fe_3O_4$ (366°C) fluid at various concentrations. Evidently, the yield stress increases with the magnetic field. However, the saturated magnetic strength, which the yield stress does not further increase after the magnetic force is raised over, can be obtained for the $Fe_3O_4$ suspension at a low concentration. Figure 8 reveals that the saturated magnetic strengths of 3 wt% and 6 wt% $Fe_3O_4$ fluids are 6000 G and 8600 G, respectively. However, the saturation point of 12 wt% $Fe_3O_4$ is far beyond the measurable range (10000 G) of the instrument, so it cannot be determined. In summary, Figure 8 demonstrated that the saturated magnetic strength increases with the particle concentrations.

Figure 9 plots the shear stress against shear rate for magnetic nanoparticles with different shape, size, and species. Figure 9 plots the effect of size on the MR behavior of $CoFe_2O_4$ particles of similar shapes (spherical or almost spherical). $CoFe_2O_4$ particles with a diameter of 10 nm have
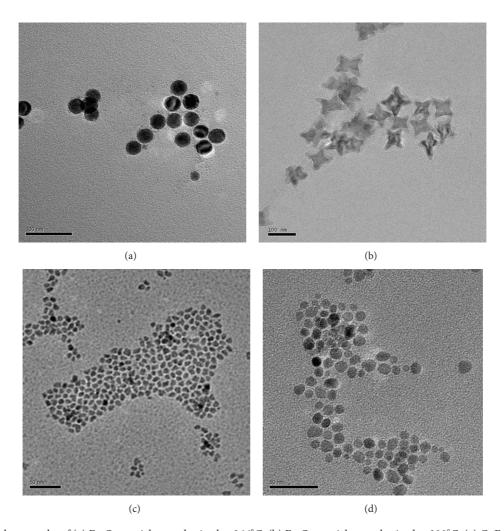
(a)

(b)

(c)

(d)

Figure 6: TEM photographs of (a) $Fe_3O_4$ particles synthesized at 366°C, (b) $Fe_3O_4$ particles synthesized at 300°C, (c) $CoFe_2O_4$ synthesizing particles at 265°C, and (d) $CoFe_2O_4$ synthesizing particles at 300°C.
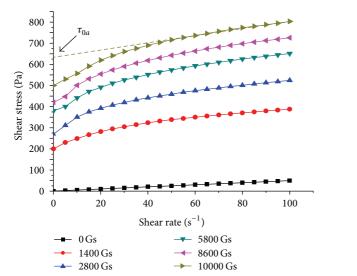


Figure 7: Shear stress is a function of shear rate for $CoFe_2O_4$ particles, synthesized at 300°C, under various magnetic fields.
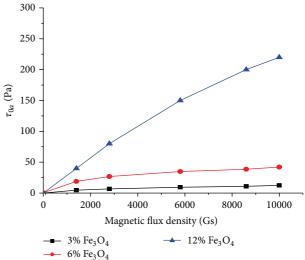
Figure 8: The yield stress of $Fe_3O_4$ fluid at different solid loading (366°C) as a function of magnetic flux intensity (Gauss).
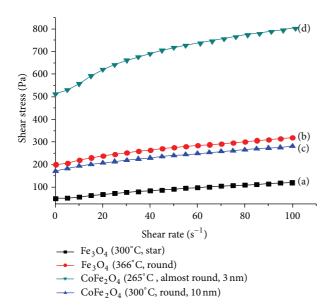
FIGURE 9: Shear stress against shear rate for various magnetic nanoparticles dispersed in silicone oil (10000 Gauss, 25°C, 12 wt%).
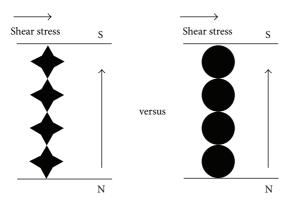


FIGURE 10: Effect of shear stress and magnetic force on star-shaped and round particles.

the best yield stress, 644 Pa, and quasi-Newtonian viscosity, 1.6 Pa S. $CoFe_2O_4$ particles with a smaller diameter, 3 nm, have a poor yield stress, which is only one third of that of the larger panicles, 188 Pa. Theoretically, a larger particle has fewer connection points and is unlikely to be destroyed by shear stress. Therefore, it can exhibit a higher MR yield stress. Figure 9 demonstrates that the yield stress of the $CoFe_2O_4$ series clearly exceeds that of the $Fe_3O_4$ series, indicating that the magnetic strength of iron cobalt oxide exceeds that of iron oxide [29]. The incorporation of the Co cation in the Fe-O matrix greatly increases the magnetic anisotropy of the materials, resulting in higher coercivity. Ferromagnetic materials with high coercivity have permanent magnets which can sustain a harsh and complex hydrodynamic environment and yield a good MR behavior. The drawback of the particles with high coercivity is the problem of particle dispersion when the field is out [30, 31]. How to prepare an MR fluid with high

magnetic strength but low self-flocculation is a tough task for us in the future.

Figure 10 illustrates that a round particle of $Fe_3O_4$ has a higher yield stress than a star particle. The core diameter of the star particle (40 nm) exceeds the diameter of the round particle (30 nm). According to the results for ferrocobalt oxide, larger particles are associated with higher yield stress, but the experiment to which Figure 9 pertains yields the opposite result. The junction of the star-shaped particle may be the connection between two arms, and it is less stable than the connection of two round particles. Accordingly, this fragile joint is easy to be destroyed by a shear force, resulting in a reduced yield force.

## 4. Conclusions

$Fe_3O_4$ is likely to be synthesized at high temperature (366°C) as round uniformly sized particles, and at low temperature (300°C) as star-shaped particles. Based on the MR test results, we conclude the following.

(1) The yield stress of the $CoFe_2O_4$ fluid is three to ten times higher than that of $Fe_3O_4$ fluid at the same concentration.

(2) In an MR fluid of round $CoFe_2O_4$ particles larger particles produce higher yield stress.

(3) The yield stress of MR fluid with round particles exceeds that of such a fluid with star-shaped particles.

(4) In an MR test, the "saturated magnetic strength" increases with the particle concentration.

## Disclosure

The MR fluids are prepared according to the method mentioned herein as a novel method. Although it still has long way to go for commercial application, its patents have been claimed and filed by the authors and the financial founder: NSC of Taiwan. There is no conflict of interests for any commercial application at present time or in the future.

## Acknowledgment

## References

[1] I. Bica, "Influence of the transverse magnetic field intensity upon the electric resistance of the magnetorheological elastomer containing graphite microparticles," *Materials Letters*, vol. 63, no. 26, pp. 2230–2232, 2009.

[2] J. H. Kim, F. F. Fang, H. J. Choi, and Y. Seo, "Magnetic composites of conducting polyaniline/nano-sized magnetite and their magnetorheology," *Materials Letters*, vol. 62, no. 17-18, pp. 2897–2899, 2008.

[3] W. H. Li, C. Lynam, J. Chen, B. Liu, X. Z. Zhang, and G. G. Wallace, "Magnetorheology of single-walled nanotube dispersions," *Materials Letters*, vol. 61, no. 14-15, pp. 3116–3118, 2007.

[4] C. C. Ekwebelam and H. See, "Using oscillatory shear to probe the effects of bidispersity in inverse ferrofluids," *Korea Australia Rheology Journal*, vol. 19, no. 1, pp. 35–42, 2007.

[5] H. Pu, F. Jiang, and Z. Yang, "Studies on preparation and chemical stability of reduced iron particles encapsulated with polysiloxane nano-films," *Materials Letters*, vol. 60, no. 1, pp. 94–97, 2006.

[6] W. H. Li and X. Z. Zhang, "The effect of friction on magnetorheological fluids," *Korea Australia Rheology Journal*, vol. 20, no. 2, pp. 45–50, 2008.

[7] S. P. Rwei, H. Y. Lee, S. D. Yoo, L. Y. Wang, and J. G. Lin, "Magnetorheological characteristics of aqueous suspensions that contain $Fe_3O_4$ nanoparticles," *Colloid and Polymer Science*, vol. 283, no. 11, pp. 1253–1258, 2005.

[8] J. Rabinow, "The magnetic fluid clutch," *Transactions of the American Institute of Electrical Engineers*, vol. 67, no. 2, pp. 1308–1315, 1948.

[9] I. Bica, "The influence of the magnetic field on the electrical magnetoresistance of magnetorheological suspensions," *Journal of Magnetism and Magnetic Materials*, vol. 299, no. 2, pp. 412–418, 2006.

[10] R. Stanway, "Smart fluids: current and future developments," *Materials Science and Technology*, vol. 20, no. 8, pp. 931–939, 2004.

[11] S. Chakrabarti, S. K. Mandal, and S. Chaudhuri, "Cobalt doped $\gamma$-$Fe_2O_3$ nanoparticles: synthesis and magnetic properties," *Nanotechnology*, vol. 16, no. 4, pp. 506–511, 2005.

[12] S. K. Mandal, "Fluorescent magnetic emulsion droplets: potential material for multiplexed optical coding of biomolecules," *Journal of Magnetism and Magnetic Materials*, vol. 311, no. 1, pp. 88–91, 2007.

[13] S. K. Mandal, N. Lequeux, B. Rotenberg et al., "Encapsulation of magnetic and fluorescent nanoparticles in emulsion droplets," *Langmuir*, vol. 21, no. 9, pp. 4175–4179, 2005.

[14] H. R. Brand and H. Pleiner, "Origin of the slow wave in a magnetorheological slurry," *Physical Review Letters*, vol. 86, pp. 1385–1385, 2000.

[15] M. Liţă, N. C. Popa, C. Velescu, and L. N. Vékás, "Investigations of a magnetorheological fluid damper," *IEEE Transactions on Magnetics*, vol. 40, no. 2 I, pp. 469–472, 2004.

[16] H. Böse, "Viscoelastic properties of silicone-based magnetorheological elastomers," *International Journal of Modern Physics B*, vol. 21, no. 28-29, pp. 4790–4797, 2007.

[17] H. See, C. Joung, and C. Ekwebelam, "Dynamic behavior and yielding of field-responsive particulate suspensions," *International Journal of Modern Physics B*, vol. 21, no. 28-29, pp. 4945–4951, 2007.

[18] R. C. Bell, E. D. Miller, J. O. Karli, A. N. Vavreck, and D. T. Zimmerman, "Influence of particle shape on the properties of magnetorheological fluids," *International Journal of Modern Physics B*, vol. 21, no. 28-29, pp. 5018–5025, 2007.

[19] F. A. Morrison, *Understanding Rheology*, Guernsey, UK, 2001.

[20] T. Hyeon, Y. Chung, J. Park, S. S. Lee, Y.-W. Kim, and B. H. Park, "Synthesis of highly crystalline and monodisperse cobalt ferrite nanocrystals," *Journal of Physical Chemistry B*, vol. 106, no. 27, pp. 6831–6833, 2002.

[21] K. Hayashi, W. Sakamoto, and T. Yogo, "Magnetic and rheological properties of monodisperse $Fe_3O_4$ nanoparticle/organic hybrid," *Journal of Magnetism and Magnetic Materials*, vol. 321, no. 5, pp. 450–457, 2009.

[22] A. Kida, C. Yamamoto, M. Doi, H. Asano, and M. Matsui, "Magnetoresistance of trilayer films with $Fe_3O_4$," *Journal of Magnetism and Magnetic Materials*, vol. 272–276, no. 1, pp. e1559–e1561, 2004.

[23] M. M. Rashad, R. M. Mohamed, and H. El-Shall, "Magnetic properties of nanocrystalline Sm-substituted $CoFe_2O_4$ synthesized by citrate precursor method," *Journal of Materials Processing Technology*, vol. 198, no. 1–3, pp. 139–146, 2008.

[24] L. A. García Cerda and S. M. Montemayor, "Synthesis of $CoFe_2O_4$ nanoparticles embedded in a silica matrix by the citrate precursor technique," *Journal of Magnetism and Magnetic Materials*, vol. 294, no. 2, pp. e43–e46, 2005.

[25] D. Maity and D. C. Agrawal, "Synthesis of iron oxide nanoparticles under oxidizing environment and their stabilization in aqueous and non-aqueous media," *Journal of Magnetism and Magnetic Materials*, vol. 308, no. 1, pp. 46–55, 2007.

[26] C. L. Nehl, H. Liao, and J. H. Hafner, "Optical properties of star-shaped gold nanoparticles," *Nano Letters*, vol. 6, no. 4, pp. 683–688, 2006.

[27] C. Yang, J. Wu, and Y. Hou, "$Fe_3O_4$ nanostructures: synthesis, growth mechanism, properties and applications," *Chemical Communications*, vol. 47, no. 18, pp. 5130–5141, 2011.

[28] W. W. Yu, J. C. Falkner, C. T. Yavuz, and V. L. Colvin, "Synthesis of monodisperse iron oxide nanocrystals by thermal decomposition of iron carboxylate salts," *Chemical Communications*, vol. 10, no. 20, pp. 2306–2307, 2004.

[29] A. Hernando, I. Navarro, C. Prados, D. García, M. Vázquez, and J. Alonso, "Curie-temperature enhancement of ferromagnetic phases in nanoscale heterogeneous systems," *Physical Review B*, vol. 53, no. 13, pp. 8223–8226, 1996.

[30] S.-Y. Zhao, K. L. Don, W. K. Chang, G. C. Hyun, H. K. Young, and S. K. Young, "Synthesis of magnetic nanoparticles of $Fe_3O_4$ and $CoFe_2O_4$ and their surface modification by surfactant adsorption," *Bulletin of the Korean Chemical Society*, vol. 27, no. 2, pp. 237–242, 2006.

[31] S. Sun, H. Zeng, D. B. Robinson et al., "Monodisperse $MFe_2O_4$ (M = Fe, Co, Mn) Nanoparticles," *Journal of the American Chemical Society*, vol. 126, no. 1, pp. 273–279, 2004.